VOLUME 6 NUMBER 1 2019 ISSN 2409-6121; eISSN 2522-1361

Physical Sciences and Technology

National Nanotechnological Laboratory of Open Type
Institute of Experimental and Theoretical Physics

Physical Sciences and Technology is publishing two number in a year by al-Farabi Kazakh National University, al-Farabi ave., 71, 050040, Almaty, the Republic of Kazakhstan
website: http://phst.kaznu.kz/

Any inquiry for subscriptions should be send to:
Gauhar Mussabek, al-Farabi Kazakh National University
al-Farabi ave., 71, 050040, Almaty, the Republic of Kazakhstan
e-mail: gauharmussabek@gmail.com

SCOPE AND AIM

Physical Sciences and Technology provides an original paperback for the publication of peerreviewed research and review articles in all fields of Physics and related Technology. The topics, included in the scope, especially emphasize understanding of the physics underlying modern technology.

Subject areas may include, but are not limited to the following fields: Astronomy and Space Research, Theoretical Physics and Astrophysics, Plasma Physics and Related Technology, Chemical Physics and Related Technology, Condensed Matter Physics and Related Technology, Thermal physics and Related Technology, Nuclear Physics and Related Technology, Nanomaterials and Nanotechnology, Applied Atomic and Molecular Physics, Material Sciences and Related Technology, Electronics and Related Technology, Instrumentation, Photonics and Quantum Electronics, Signal processing.

The Journal is issued under the auspices of the National Nanotechnological Laboratory of Open Type and Institute of Experimental and Theoretical Physics and is published two times a year by the «Kazakh University» Publishing House. The International Editorial Board of the Journal consists of leading researchers from different countries of the world. The Journal is wide open for contributions that both lie at the far frontiers of contemporary physics and are particularly aimed at applications of the scientific principles of physics to modern technological problems.

IRSTI 29.15.29

On three-cluster disintegration of ^{9}Be

V.S. Vasilevsky[1,*] and K. Kato[2]

[1]*Bogolyubov Institute for Theoretical Physics,*
14-b Metrolohichna str., 02000, Kiev, Ukraine
[2]*Reaction Data Centre, Faculty of Science, Hokkaido University,*
Kita-10 Nishi-8, Kita-ku,060-0810, Sapporo, Japan
**e-mail:vsvasilvesky@gmail.com*

We study a process of the photodisintegration of some Borromean light nuclei into three clusters. This study is performed within a three-cluster microscopic model. In Reference [1] this model was applied to obtain parameters of resonance states in ^{9}Be and ^{9}B and to establish their nature. Main aim of the present investigations is to describe the dipole transition probability from the ground state of ^{9}Be to the states of three-cluster α+α+n continuum by using the same model. That model exploits the hyperspherical harmonics basis (HHB) and thus reduces many-channel Schrödinger equation to the algebraic matrix (AM) form. The dipole transitions from the ground 3/2- state to the 1/2+ states of three-cluster continuum were studied in detail. The role of resonance states in three-cluster continuum to this process is investigated in detail. The dominant channels with the maximal dipole strength due to the coupling between the ground and scattering states are discovered.

Key words: light nuclei, three-cluster microscopic model, hyperspherical harmonics basis, algebraic matrix, dipole transition.
PACS number: 25.20

1 Introduction

We consider the photodisintegration of some light nuclei into three fragments. This process is considered for nuclei with distinguished three-cluster features, or, in other words, nuclei which have the lowest three-cluster decay threshold. Such nuclei are also called the Borromean nuclei. In the present paper we will concentrate on the nucleus ^{9}Be, which considered as a three-cluster configuration α+α+n. These investigations are also aimed at clarifying the existence and properties of the $1/2^{+}$ resonance state in ^{9}Be.

All investigations are carried out within a microscopic three-cluster model. For this model we will use an abbreviation AMHHB which indicates that the model exploits the hyperspherical harmonics basis (HHB) and thus reduces many-channel Schrödinger equation to the algebraic matrix (AM) form. The key elements of the AMHHB were formulated in Reference [2] and then applied to study the three-cluster continuum in light nuclei.

In a set of publications [3, 4, 5, 6, 7, 8] the photodisintegration of ^{9}Be into two alpha-particles and a neutron has been considered within the orthogonality condition model (OCM) which make uses the Gaussian basis and the complex scaling method (CSM) to locate resonance states. In these papers the $1/2^{+}$ excited state was shown to be a virtual state situated a very close to the two-cluster ^{8}Be+n threshold. It was also shown that a huge peak of the photodisintegration cross section is created by the virtual state in the two-body channel ^{8}Be (0^{+})+n.

The three-cluster photodisintegration also attracts numerous experimental studies. The recent experimental measurements of the photodisintegration cross section are presented in References [9, 10, 11].

2 AMHHB and coupled channels methodology

In this section we present the main ideas of the AMHHB method. Basic ideas of the method were formulated in Reference [2]. In the present paper we

will the same notations as in recent publications [1, 12, 13].

Any microscopic model is based on a microscopic Hamiltonian, which includes a nucleon-nucleon interaction and the Coulomb forces, and on form of a fully-antisymmetrized wave function.

Within a three-cluster model, a wave function of compound system with a partition A = A_1 + A_2 + A_3 is

$$\Psi_{EJM_J} = \hat{A}\Big\{\Big[\Phi_1\left(A_1,s_1\right)\Phi_2\left(A_2,s_2\right)\Phi_3\left(A_3,s_3\right)\Big]_S \times \sum_{l_1,l_2} f^{(E,J)}_{l_1,l_2;L}\left(x,y\right)\Big\{Y_{l_1}\left(\hat{\mathbf{x}}\right)Y_{l_2}\left(\hat{\mathbf{y}}\right)\Big\}_L\Big\}_{JM_J} \tag{1}$$

All notations are the same as in Reference [1]. We also refer to Reference [1] for explanation of details of all parts of the wave function (1), quantum numbers and the Jacobi vectors **x** and **y**.

By using hyperspherical coordinates

$$x = \rho\cos\theta, \qquad y = \rho\sin\theta, \qquad \Omega = \left\{\theta, \hat{\mathbf{x}}, \hat{\mathbf{y}}\right\}, \tag{2}$$

the wave function (1) is represented as

$$\Psi_{EJM_J} = \hat{A}\Big\{\Big[\Phi_1\left(A_1,s_1\right)\Phi_2\left(A_2,s_2\right)\Phi_3\left(A_3,s_3\right)\Big]_S \times \sum_{K,l_1,l_2,L} \psi^{(E,J)}_{K,l_1,l_2;L}\left(\rho\right)Y_{K,l_1,l_2;L}\left(\Omega\right)\Big\}_{JM_J}, \tag{3}$$

where K is the hypermomentum, $Y_{K,l_1,l_2;L}\left(\Omega\right)$ is a hyperspherical harmonic. A set of quantum numbers

$$c = \left\{K, l_1, l_2, L\right\}, \tag{4}$$

numerates channels of the three-cluster continuum.

The hyperspherical harmonics allow us to employ the rigorous methodology coupled channels. In this case the many-particle Schrödinger equation transforms in a set of coupled equations for a column vector of hyperradial functions:

$$\mathrm{x}\,\psi = \begin{pmatrix} \psi_{c_1} \\ \psi_{c_2} \\ \psi_{c_3} \\ \vdots \end{pmatrix}, \tag{5}$$

Components $\psi_{c_i}\left(\rho\right)$ of the wave function (5) are subject for boundary conditions, which were discussed in detail in Reference [12]. The total many-particle Hamiltonian $\hat{H}$ is split onto the channel Hamiltonians $\hat{H}_{cc}$ and $\hat{H}_{c\tilde{c}}$ ($\tilde{c} \neq c$) for coupling between channels. Both channel Hamiltonians and coupling Hamiltonians contain local and non-local componentsdue to the antisymmetrization. In the channel Hamiltonians, the local part consists of the kinetic energy operator and the folding (or direct) potentials. On other hand, the coupling Hamiltonians contains the local part consisting of the folding (or direct) potentials only. It means that there are contributions from the interaction only, but not from the kinetic energy term.

Hamiltonians $\hat{H}_{cc}$ and $\hat{H}_{c\tilde{c}}$ ($\tilde{c} \neq c$) are obtained by sandwiching of the total Hamiltonian between the corresponding hyperspherical harmonics Y_c and $Y_{\tilde{c}}$

$$\left\langle \hat{A}\left\{\Phi_1\Phi_2\Phi_3 Y_c\right\} \middle| \hat{H} \middle| \hat{A}\left\{\Phi_1\Phi_2\Phi_3 Y_{\tilde{c}}\right\}\right\rangle$$

and integrating over all hyperangels and over those Jacobi coordinates describing the internal structure of interacting clusters. If we assume that the antisymmetrization operator $\hat{A}$ = 1, we obtain the local form of the Hamiltonians $\hat{H}_{c\tilde{c}}$.

It is important to underline, that within the coupled channel methodology, if we have N_{ch} open channels then for each energy we have N_{ch} independent solutions (wave functions) which describe all possible elastic and inelastic processes. It is well known (see for instance, chapter 6 of book [14] and Reference [15]) that the first wave function is obtained by assuming that there is an incoming wave in the first channel and outgoing waves appear in all channels, the second wave function contains

the incoming wave in the second channel, and so on. Thus these functions can be marked by the channel c which possesses both incoming and outgoing waves. Thus, considering a photo- or electro-disintegration of Borromean nuclei we automatically obtain N_{ch} cross sections of the process.

Suppose we obtained wave function of a bound state $\Psi_{E_iJ_i}$ and wave function $\Psi_{E_fJ_f}$ of continuous spectrum state with energy E_f measured from the three-cluster threshold. Then we can calculate probability of the dipole λ=1 transition from bound to continuous states

$$B\left(E\lambda; E_i, J_i \Rightarrow E_f, J_f\right) = \\ = \frac{1}{2J_i+1}\left|\left\langle E_f, J_f \left\| \hat{Q}_\lambda \right\| E_i, J_i \right\rangle\right|^2, \quad (6)$$

where

$$\hat{Q}_{\lambda\mu} = \sum_{i=1}^{A} \frac{1}{2}\left(1+\hat{\tau}_{iz}\right) r_i^\lambda Y_{\lambda\mu}\left(\hat{\mathbf{r}}_i\right), \quad (7)$$

vector $\mathbf{r}_i$ ($\mathbf{r}_i = r_i\hat{\mathbf{r}}_i$) is a coordinate of the i^{th} nucleon. It is important to note that wave functions $\Psi_{E_iJ_i}$ and $\Psi_{E_fJ_f}$ of bound and scattering states, respectively, are normalized by the following conditions

$$\left\langle \Psi_{E_i,J_i} \middle| \Psi_{E_i,J_i} \right\rangle = 1, \quad (8)$$

$$\left\langle \Psi_{E_f,J_f} \middle| \Psi_{\tilde{E}_f,J_f} \right\rangle = \delta\left(k-\tilde{k}\right), \quad (9)$$

where

$$k = \sqrt{\frac{2mE}{\hbar^2}}, \quad \tilde{k} = \sqrt{\frac{2m\tilde{E}}{\hbar^2}}.$$

In this section we defined all necessary quantities to perform the theoretical analysis of the dipole transitions from the bound state of the Borromean nucleus ^{9}Be to its continuous spectrum states.

3 Three-cluster photodisintegration ^{9}Be

In this nucleus, the $1/2^+$ resonance state is a mysterious state which is seen in one set of experiments, but does not observed in other set of experiments. Such a situation is also observed with different theoretical models. It was shown in References [1] and [16] that the AMHHB model confirms the existence of the $1/2^+$ resonance state. These results were obtained with the modified Hasegawa-Nagata potential [17, 18] in Reference [1] and the Minnesota potential [19, 20] in Reference [16]. Energies of resonance states in ^{9}Be are determined from the three-cluster α+α+n threshold.

In Table 1 we show the input parameters of calculations for ^{9}Be and the energy of the ground state, and energies and widths of the $1/2^+$ resonance states. These results are obtained in Reference [1] with the MHNP and in Reference [16] with the MP. Both potential creates at least two resonance states, one of which is close to the three-cluster threshold (E=0.248 MeV and E=0.338 MeV) and other lies at energy E=1.664 MeV and E=1.432 MeV. Energies of resonance states obtained with two different nucleon-nucleon potential are close, however their widths are quite different.

In Table 2 we display two-body threshold energies of ^{8}Be(0^+)+n and ^{5}He($3/2^-$)+α, as they play an important role in the photodisintegration of ^{9}Be. These energies are measured from the three-cluster threshold and they include energies of the 0^+ resonance state in ^{8}Be and the $3/2^-$ resonance state in ^{5}He, respectively.

Table 1 – Energy of the ^{9}Be ground state and parameters of the $1/2^+$ resonance states

Input parameters			$J^\pi=3/2^-$	$J^\pi=1/2^+$			
Potential	b (fm)	u/m	E (MeV)	E (MeV)	Γ (keV)	E(MeV)	Γ (MeV)
MP	1.285	0.9280	-1.555	0.248	15	1.664	1.520
MHNP	1.317	0.4389	-1.574	0.338	168	1.432	0.233

Table 2 – Parameters of resonance states in two-cluster subsystem of ^{9}Be

Channel	^{8}Be(0^{+})+n		^{5}He($3/2^{-}$)+α	
Potential	E (MeV)	Γ (keV)	E (MeV)	Γ (MeV)
MP	0.172	0.748	1.059	1.116
MHNP	0.859	958.40	0.385	0.209

Let us turn our attention to the dipole transitions. In Figure 1 we display the dipole transition probability from the $3/2^{-}$ ground state to the $1/2^{+}$ continuous spectrum states of ^{9}Be. The bar plots indicate energy (the centre of the bar) and with of the $1/2^{+}$ resonance states. In Figure 1 we show the dipole transition probability for three wave functions of continuous spectrum state. These functions are distinguished by the entrance channel K = 0, K = 2 and K = 4. As one can see, the first wave function is dominant-channel in the present region of energy. Besides the first $1/2^{+}$ resonance state is created in this channel, the dipole transition probability is very small.

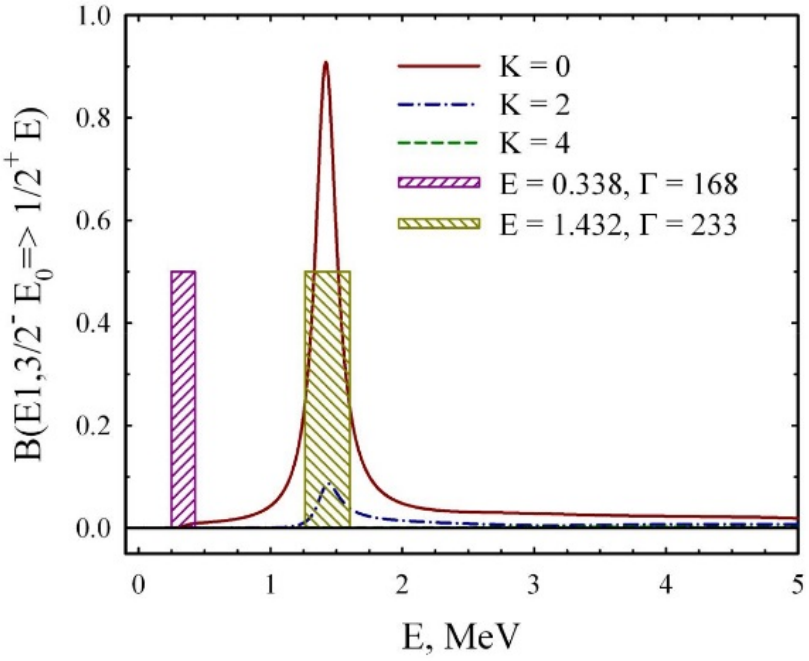

Figure 1 – Distribution of the dipole transition probability over continuous spectrum states of ^{9}Be. The bars present the energy (in MeV) and width (in keV) of the $1/2^{+}$ resonance states.

It is interesting to note that shape of the function B(E1; $3/2^{-}$ E_0=>$1/2^{+}$E) is similar to the weight of the internal part of the scattering 1/2+ wave function.

The latter is displayed in Figure 2 for three dominant wave functions of the $1/2^{+}$ state generated by the entrance channels with K = 0, K = 2, and K = 4, respectively.

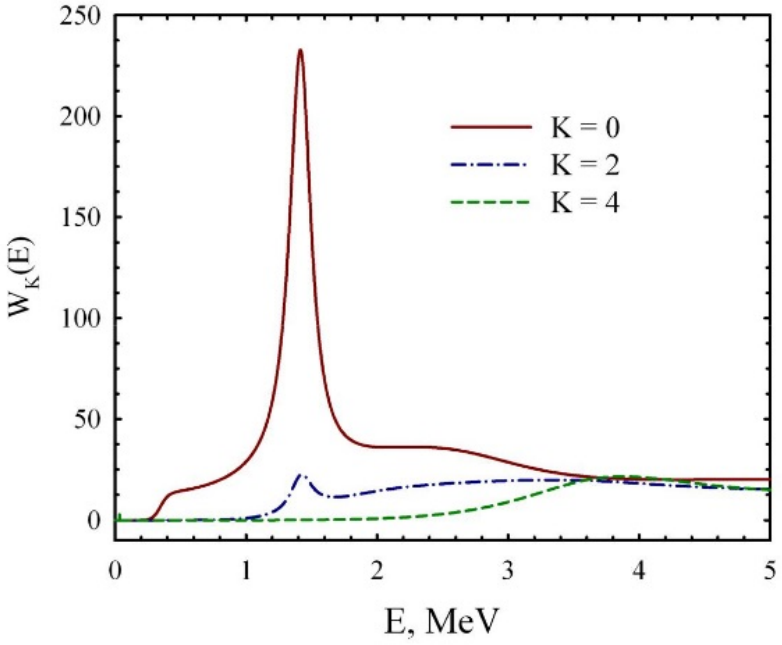

Figure 2 – Weights $W_K(E)$ of the internal part of the many-channel wave function describing three-cluster scattering in the state $J^\pi = 1/2^+$.

Contribution of the first $1/2^+$ resonance state to the dipole transition is shown in Figure 3. One can see that the contribution of the first $1/2^+$ resonance state is not as prominent as for the second $1/2^+$ resonance state. This is a result of a kinematical factor that suppresses the dipole transition at the low-energy region.

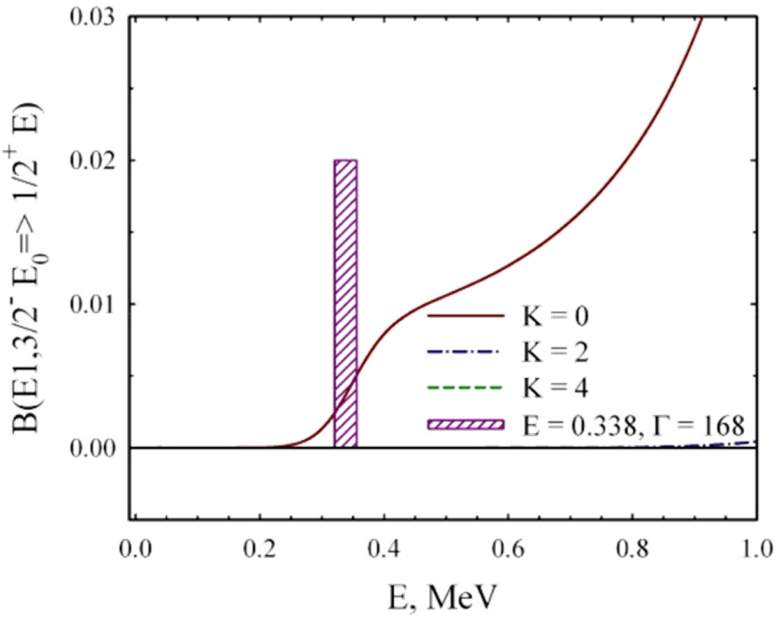

Figure 3 – The distribution of the dipole transition in ^{9}Be around the first $1/2^+$ resonance state.

4 Conclusions

We have considered the photodisintegration of the nucleus ^{9}Be. The consideration has been performed within a microscopic three-cluster model α+α+n. The model employs the full set of six-dimension oscillator functions to describe relative motion of clusters. Oscillator functions are numerated the quantum numbers of the hyperspherical harmonics method. The hyperspherical harmonics are very suitable for implementing the boundary conditions for wave functions of three-cluster continuous states. The dipole transitions from the ground $3/2^-$ state to the $1/2^+$ states of three-cluster continuum were studied in detail. We demonstrated that the low-lying $1/2^+$ resonance state weakly contributes to the dipole transition probability, while the second $1/2^+$ resonance state has strong impact on the dipole transition probability.

Acknowledgements

Authors are grateful to Prof. N. Zh. Takibayev, Mrs. A.D. Duisenbay and Mr. N. Kalzhigitov from the Faculty of Physics and Technology, Al-Farabi Kazakh National University, Almaty, Republic of Kazakhstan, for hospitality and stimulating discussion during their stay at Al-Farabi Kazakh National University. This work was supported in part by the Program of Fundamental Research of the Physics and Astronomy Department of the National Academy of Sciences of Ukraine (Project No. 0117U000239) and by the Ministry of Education and Science of the Republic of Kazakhstan, Research Grant IRN: AP 05132476.

References

1. V. S. Vasilevsky, K. Kato, N. Z. Takibayev. Formation and decay of resonance states in ^{9}Be and ^{9}B nuclei: Microscopic three-cluster model investigations // Phys. Rev. C. – 2017. – Vol. 96. – P. 034322.

2. V. Vasilevsky, A. V. Nesterov, F. Arickx, J. Broeckhove. Algebraic model for scattering in three-s-cluster systems I. Theoretical background // Phys. Rev. C. – 2001. – Vol. 63. – P. 34606.

3. M. Odsuren, K. Kato, Y. Kikuchi, M. Aikawa, T. Myo. A resonance problem on the low-lying resonant state in the ^{9}Be system // J. Phys. Conf. Ser. – 2014. – Vol. 569. – P. 012072.

4. M. Odsuren, Y. Kikuchi, T. Myo, M. Aikawa, K. Kato. Virtual-state character of the ^{9}Be $1/2^+$ state in the ^{9}Be $(\gamma,n)^{8}$Be reaction // Phys. Rev. C. – 2015. – Vol. 92. – P. 014322.

5. Y. Kikuchi, M. Odsuren, T. Myo, K. Kato. Photodisintegration cross section of ^{9}Be up to 16 MeV in the α+α+n three-body model // Phys. Rev. C. – 2016. – Vol. 93. – P. 054605.

6. M. Odsuren, Y. Kikuchi, T. Myo, M. Aikawa, K. Kato. Photodis-integration of ^{9}Be and the importance of the unbound $1/2^+$ state // Eur. Phys. J. Web Conf. – 2016. – Vol. 109. – P. 05007.

7. M. Odsuren, Y. Kikuchi, T. Myo, G. Khuukhenkhuu, H. Masui, K.Kato. Virtual-state character of the two-body system in the complex scaling method // Phys. Rev. C. – 2017. – Vol. 95. – P. 064305.

8. M. Odsuren, Y. Kikuchi, T. Myo, M. Aikawa, K. Kato. The first unbound states of mirror ^{9}Be and ^{9}B nuclei // Eur. Phys. J. Web Conf. – 2017. – Vol. 146. – P. 12012.

9. A. E. Robinson. Reanalysis of radioisotope measurements of the ^{9}Be$(\gamma,n)^{8}$Be cross section // Phys. Rev. C. – 2016. – Vol. 94. – P. 024613.

10. H. Utsunomiya, S. Katayama, I. Gheorghe, S. Imai, H. Yamaguchi,Kahl, Y. Sakaguchi, T. Shima, K. Takahisa, S. Miyamoto.Photodisintegration of ^{9}Be through the $1/2^+$ state and cluster dipole resonance // Phys. Rev. C. – 2015. – Vol. 92. – P. 064323.

11. C. W. Arnold, T. B. Clegg, C. Iliadis, H. J. Karwowski, G. C. Rich,R. Tompkins, C. R. Howell. Cross-section measurement of^{9}Be$(\gamma,n)^{8}$Be and implications forα+α+n →^{9}Be in the r process //Phys. Rev. C. – 2012. – Vol. 85. – P. 044605.

12. V. S. Vasilevsky, Y. A. Lashko, G. F. Filippov. Two- and three-cluster decays of light nuclei within a hyperspherical harmonics approach // Phys. Rev. C. – 2018. – Vol. 97. – P. 064605.

13. V. S. Vasilevsky, K. Kato, N. Takibayev. Systematic investigation of the Hoyle-analogue states in light nuclei // Phys. Rev. C. – 2018. – Vol. 98. – P. 024325.

14. A.I. Baz, Ya.B. Zel'dovich, A.M. Perelomov. Scattering reaction in non-relativistic quantum mechanics // Jerusalem: Israel Program for Scientific Translations. -1969.

15. R. F. Barrett, B. A. Robson, W. Tobocman. Calculable methods for many-body scattering // Rev. Mod. Phys. – 1983. – Vol. 55. – P. 155-243.

16. A. V. Nesterov, V. S. Vasilevsky, T. P. Kovalenko. Nature of resonance states in the ^{9}Be and ^{9}B mirror nuclei // Phys. Atom. Nucl. – 2014. – Vol. 77. – P. 555-568.

17. A. Hasegawa, S. Nagata. Ground state of ^{6}Li. // Prog. Theor. Phys. – 1971. – Vol. 45. – P. 1786-1807.

18. F. Tanabe, A. Tohsaki, R. Tamagaki. αα scattering at intermediate energies // Prog. Theor. Phys. – 1975. – Vol. 53. – P. 677-691.

19. D. R. Thompson, M. LeMere, Y. C. Tang. Systematic investigation of scattering problems with the resonating-group method // Nucl. Phys.A. – 1977. – Vol. 286. – No. 1. – P. 53-66.

20. I. Reichstein, Y. C. Tang Study. of N+α system with the resonating-group method // Nucl. Phys. A. – 1970. – Vol. 158. – P. 529-545.

IRSTI 29.27.51

Periodic variations in time of atmospheric alpha and beta radioactive nanoparticles

V.V. Dyachkov[1,*], Yu.A. Zaripova[2], A.V. Yushkov[2], A.L. Shakirov[2], M.T. Bigeldiyeva[2], K.S. Dyussebayeva[2], K.E. Abramov[2]

[1]National Research Nuclear University (MEPhI), Moscow, Russia, 115409, Kashirskoe shosse, 31, Moscow, Russian Federation
[2]National Nanotechnological Laboratory of Open Type, al-Farabi Kazakh National University, 71, al-Farabi Ave., 050040, Almaty, Kazakhstan
*e-mail:*lnirp206@gmail.com*

Here we present time variations data of radon emanations in the surface layer of the atmosphere, measured from January 2016 to June 2018. By means of spectral analysis method, we have analyzed time variations and showed the presence of existing natural variations, mechanisms of which were described by the authors in previous works. Authors measured the activity of natural beta-active radionuclides of radon's daughter decay products (DDP) in the surface layer of the atmosphere. The measurements were performed with a beta-spectrometer "Progress" scintillation detector, which is located on the third floor of the Faculty of Physics and Technology at al-Farabi Kazakh National University (KazNU). Measurements of beta spectra were carried out with an exposure of at least for 2000 seconds and during the day up to 10 beta spectra were recorded. The built up time dependence of the integral values of the spectra shows that seasonal variations of natural beta-active radionuclides are manifested on the background of diurnal fluctuations. Thus, 1 day, 4 day, 7 day, 16 day and 30 day variations were found.

Key words: variations in time of radon; natural beta active radionuclides; coagulation; atmospheric radioactive nanoparticles.
PACS number: 23.60

1 Introduction

The study of spatial topologies of radon emanations in the atmospheric surface layers is extremely topical, primarily due to the direct effect of radon on human health [1]. The Earth's crust from the initial moment of its formation contains natural radioactive elements, creating a natural radiation background. Radioactive isotopes of potassium-40, rubidium-87 and members of three radioactive families originating from uranium-238, uranium-235 and thorium-232 are present in rocks, soil, atmosphere, waters, plants and tissues of living organisms. The only gaseous product that is produced during the decay of three families of natural radionuclides is radon. 39 radon isotopes are known (all are radioactive), three of which are natural: ^{119}Rn, ^{220}Rn and ^{222}Rn. Under normal conditions, there is $7*10^{-6}$ g of radon in 1 m^3 of air [2].

Despite the fact that the oncological danger of radon is known and studied for a long time [3–9], no country in the world established standards for the maintenance of radon and its daughter products in premises until 1980. There was a need for rationing doses to the population by radon isotopes. In the Republic of Kazakhstan, these standards were also introduced [10].

2 Experimental procedure and methodology

The measurements were carried out by "RAMON-02A", an electronic radon radiometer and its daughters, developed in the Republic of Kazakhstan [11]. For stationary location in a room or in a specially installed radio-ecological observation station, it is intended for automatic monitoring of the content of equivalent equilibrium volumetric activity (EEVA) of radon Rn-222 in air

in residential and industrial premises, as well as in atmospheric air. The device measures radon's EEVA in the range 4-5 *10^5 Bq/m^3. It uses an alpha-spectrometric method of measurement based on surface-barrier semiconductor detectors, and an absorbent tape, designed for at least three thousand measurements, is installed as a filter material, from which the accumulated alpha activity of radon is read.

The territories of Almaty are characterized by the existence of extensive zones of tectonic faults. World literature data show that elevated levels of radon emanations are associated with existing tectonic faults. On this reason, an object located in the tectonic fault zone was selected for the study.

This work is a continuation of [12]. To measure the time topology of the radon isotopes emanation in a continuous mode in buildings and premises, we have selected room, located on the third floor at the Faculty of Physics and Technology at al-Farabi KazNU.

In order to increase the effect, i.e., to register more powerful emanations of radon isotopes, a stationary installation was installed near the large Almaty tectonic fault, on one of its branches at the campus of the university. To measure the equilibrium and nonequilibrium components of radon isotope emanation, two measuring instruments were placed in the room with positions at a height of 1 m from the floor level. The measurements were carried out for 10 months with a periodicity of 2 hours. The instrument is automated to collect measurement results into a common database, with which measurement results were copied to a PC every 5 days. Figure 1 shows the time dependence of radon activity in the first half of 2018.

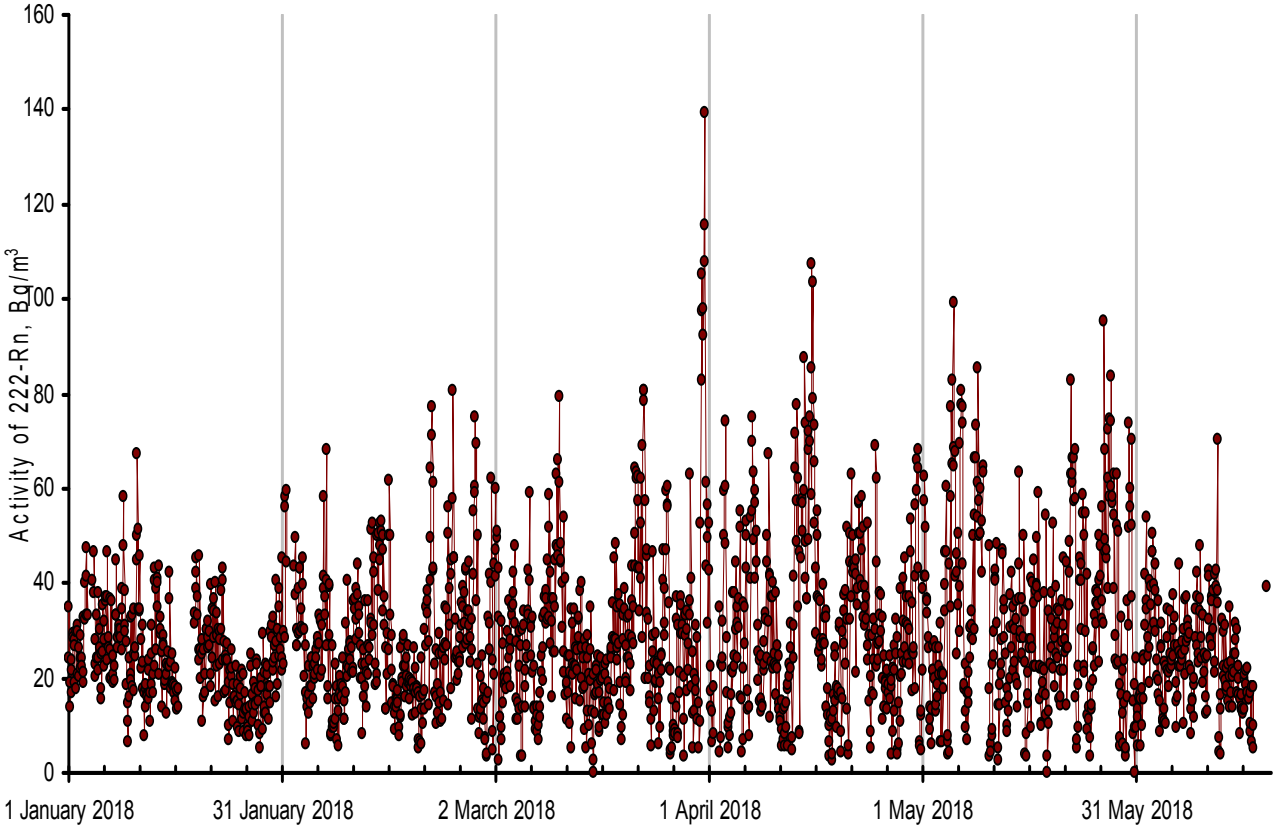

Figure 1 – The results of measurements in the experimental room using a radiometer "Ramon-02A" for the first half of 2018

3 Analysis of experimental data

Variations in the emanation of radon, as it was shown in [13–21], depend on a rather large number of factors exerting their influence. In Figure 2 there are measurements of radon activity over a long period.

In addition, the time topology of the experimental data was analyzed by the method of spectral analysis, which is one of the main ones in the study of time signals and allows us to characterize the frequency composition of the measured complex spectrum. The Fourier transform is a mathematical framework that relates the time signal to its representation in the frequency domain. An important role in spectral analysis is played by statistical methods, since the signals are usually random or noisy during propagation or measurement.

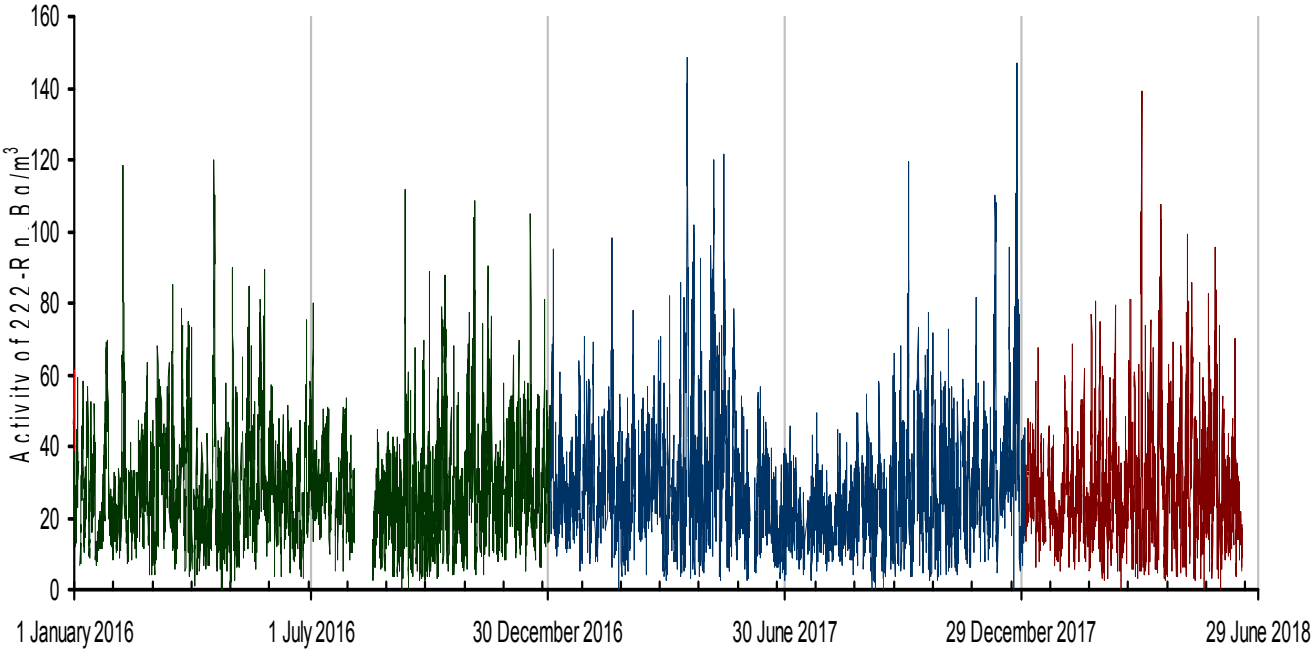

Figure 2 – The results of measurements in the experimental room using a radiometer "Ramon-02A" for the period from 2016 to the first half of 2018

Mathematically, a signal with a duration of T seconds is some function f (x) defined on the interval {0, T} (where X is time). Such signals can always be represented as the sum of harmonic functions (sine or cosine):

$$f(x) = \frac{a_0}{2} + \sum_{k=1}^{+\infty} A_k \cos\left(2\pi \frac{k}{\tau} x + \theta_k\right) \qquad (1)$$

where k is the number of the trigonometric function (the number of the harmonic component, the number of the harmonic); T is the length of time in which the function is defined (signal duration); A_k is the amplitude of the k-th harmonic component, θ_k is the initial phase of the k-th harmonic component. This series can also be written in another form:

$$f(x) = \sum_{k=-\infty}^{+\infty} \hat{f}_k e^{i2\pi \frac{k}{\tau} x} \qquad (2)$$

where $\hat{f}_k$, k-i complex amplitude, or

$$f(x) = \frac{a_0}{2} + \sum_{k=1} [a_k \cos(2\pi \frac{k}{\tau} x) + b_k \sin(2\pi \frac{k}{\tau} x)] \qquad (3)$$

The relationship between the coefficients (1) and (3) is expressed by the following formulas:

$$A_k = \sqrt{a_k^2 + b_k^2}, \qquad \theta_k = arctg\frac{b_k}{a_k} \tag{4}$$

Note that all these three representations of the Fourier series are completely equivalent. The amplitude spectra were built up by the results of a theoretical analysis of the time variations. Figure 3 presents the amplitude spectrum, which was obtained on the basis of the description by formulas (3, 4) of experimental data for the first half of 2018.

In the Figure 3, circles indicate the variations that were identified in the experimental data. It is known that the mechanism of radon emanation to the surface of the Earth is complex [19-21]. In particular, from the inner surfaces of the Earth's crust radon is transported due to the diffusion of aerosols to the surface, to which due to electrostatic attraction the radon atoms coagulate. The authors carried out an areal measurements of soil samples of the surface layer of the earth for the content of beta-active radionuclides of radon daughters [22-25], taken at different points of the city of Almaty. According to these data, a map of the distribution of the content of beta-active radionuclides of radon daughters in the soil of the surface layer of the earth was constructed.

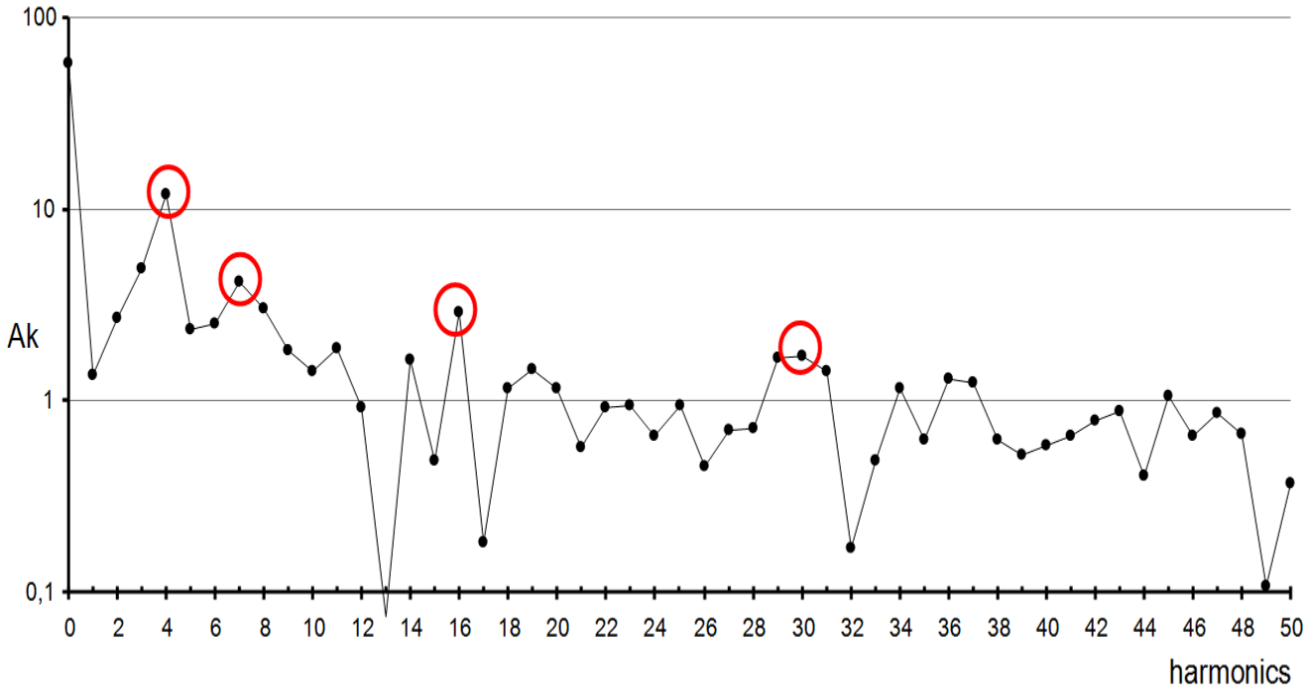

Figure 3 – Amplitude spectrum to describe experimental data on radon activity in the first half of 2018

Due to the fact that measurements of radon emanation are quite complex and the results oftenly depend on subjective factors effecting them, measurements of the activity of beta-active radionuclides of radon daughters in the surface layer of the atmosphere at various points in time were performed. Measurements of beta spectra were carried out with an exposure time of at least 2000 seconds and during the day up to 10 beta spectra were recorded. A typical beta spectrum of the radiation background is shown in Figure 4. We have also built up a time dependence of the integral values of the beta spectra.

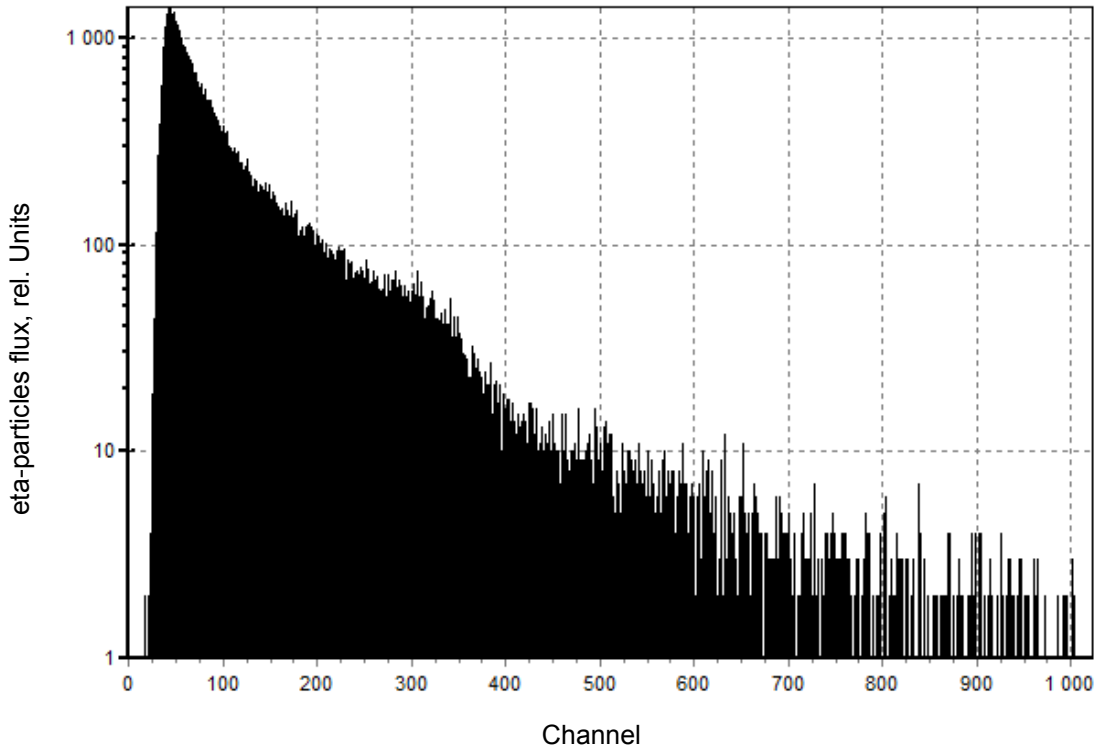

Figure 4 – Typical beta spectrum of radiation background

Figure 5 shows the integral values of the spectra (points) and values averaged over two days (solid line). It is clear that the seasonal variation of natural beta-active radionuclides is traced against the background of diurnal fluctuations. This variation correlates quite well with the variation of radon activity.

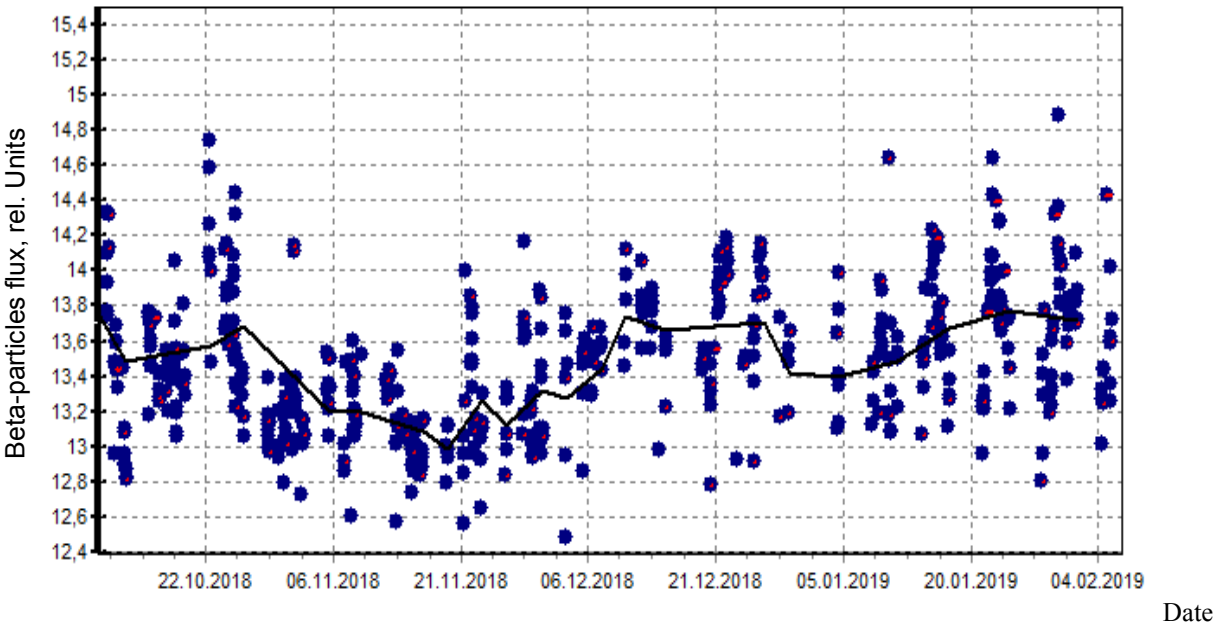

Figure 5 – Time variations of natural beta active radionuclides.

4 Conclusions

The paper presents experimental data of the radon activity for the period from January 2016 to June 2018. The analysis of time variations was carried out by the method of spectral analysis, which showed the presence of existing natural variations, the mechanisms of which were described by the authors in previous works [12, 19-25]. The authors measured the activity of natural beta-active radionuclides of radon daughters in the surface layer of the atmosphere. The measurements were performed with a beta-spectrometer with a "Progress" scintillation detector, which was located on the third floor of the Faculty of Physics and Technology, al-Farabi KazNU. The time dependence of the integral values of the spectra showed that seasonal variations of natural beta-active radionuclides are manifested on the background of diurnal fluctuations. 1 day, 4 day, 7 day, 16 day and 30 day variations were found.

Acknowledgements

The work was supported by the state grant financing of basic research (project No. IRN AP05131884 "Fundamental research of the mechanisms of formation of nanoscale onco-radiogenic structures in the body and development of anticancer express devices for their detection").

References

1. I.L. Knunyants. Short chemical encyclopedia // Moscow. – 2012. – Vol. 4. – 590 p.
2. I.N. Beckman. Radon: enemy, doctor and assistant // Moscow. – 2000. – 205 p.
3. Protection against radon-222 in residential buildings and workplaces // Publication 65 of the ICRP, Moscow. – 1995. – 78 p.
4. Risk of lung cancer due to irradiation with daughter radon decay products indoors // Publication 50 ICRP, Moscow. – 1992. – 112 p.
5. I.V. Yarmoshenko, I.A. Kirdin, M.V. Zhukovsky, S.Yu. Astrakhantseva. Meta-analysis of epidemiological studies of the risk of lung cancer during irradiation with radon in dwellings // Medical Radiology and Radiation Safety. – 2003. – Vol. 48. – No. 5. – P. 33-43.
6. J. Milner, C. Shrubsole, P. Das, B. Jones, I. Ridley, Z. Chalabi, I. Hamilton, B. Armstrong, M. Davies, P. Wilkinson. Home energy efficiency and risk of breast cancer: a modelling study // BMJ. – 2014. – Vol. 348. – P.1.
7. I.M. Fisenne, L. Machta, N.H. Harlez. Stratospheric radon measurements in three North American locations // The Natural Radiation Environment VII: VIIth Int. Symp. On the NRE. – 2005. – Vol. 7. – P. 715-721.
8. I.M. Fisenne. Radon-222 measurements at Chester // EML-422. – 1984. – P. 15-149.
9. S. Darby, D. Hill, R. Doll. Radon: A likely carcinogen at all exposures // Annals of Oncology 12. – 2001. – P. 10.
10. Law of the Republic of Kazakhstan No. 219-I of April 23, 1998 "On radiation safety of the population". – 2016.
11. V.N. Sevostyanov. The Problem of radon safety in Kazakhstan // Almaty, 2004. – 212p.
12. V.V. Dyachkov, Yu.A. Zaripova, A.V. Yushkov, A.L. Shakirov, M.T. Bigeldiyeva, K.S. Dyussebayeva, K.E. Abramov. Periodic variations in time of atmospheric radioactive nanoparticles // Physical sciences and technology. – 2017. – Vol. 4(1). – P. 20-26.
13. S. Okade. Time variation of the atmospheric radon content, near University of Kyoto // Memoir of College of Science. – 1956. – Vol. 28. – P. 99-115.
14. V.I. Outkin, A.K. Yurkov, S.V. Kridasheev. Dynamics of radon concentration in soil for predicting earthquakes. Proc. Third Eurosymposium on Protection against radon // Liege. – 2001. – P. 137-141.
15. O.N. Kosyanchuk The possibility of using radon exhalation dynamics as a reliable indicator of seismic activity // Young Scientist. – 2011. – Vol.1, No. 11. – P. 53-55.
16. E.V. Bazhko, E.V. Dyachkov, E.V. Ermahanova, E.V. Yushkov. Investigation of permeability of cell membranes under the influence of alpha irradiation of radon isotopes // Collection of reports "Nuclear potential of Kazakhstan", Almaty. – 2011. – P. 138-143.
17. A.V. Yushkov, V.V. Dyachkov. Nuclear-physical mechanisms of the effect of alpha radiation of radon on the cell and the problem of cancer morbidity // Collection of scientific works, Almaty. – 2012. – P. 21-27.
18. Yu.A. Zaripova, A.A. Migunova, V.V. Dyachkov, A.V. Yushkov. Development of nanotechnologies for nuclear medicine // Proceedings of the X-th International Conference, Almaty. – 2013. – Vol. 1. – P. 83-93.
19. V.V. Dyachkov, A.V. Yushkov, A.A. Migunova, A.L. Shakirov, V.A. Sysoev. Development of nanotechnology for creating a radiogenic element base for electronics // Proceedings of the X-th International Conference, Almaty. – 2013. – Vol. 1. – P. 62-69.

20. Yu.A. Zaripova, V.V. Dyachkov, A.V. Yushkov, Z.M. Biyasheva, O. Kh. Khamdieva. Two regularities of radon oncorisium, enhanced by an emanation near the tectonic fault // Collection of theses and reports “Nucleus 2016”, Sarov. – 2016. – P. 181-182.

21. V.V. Dyachkov, Z.M. Biyasheva, Yu.A. Zaripova, A.L. Shakirov, A.V. Yushkov. Gravitational interaction of lithospheric substructures and lands with the moon as precursors of destructive earthquakes // Collection of theses and reports “SDFFFO-9”, Almaty. – P. 12-14.

22. V.V. Dyachkov, Z.M. Biyasheva, A.A. Komarov, Yu.A. Zaripova, A.L. Shakirov, A.V. Yushkov, O.Kh. Khamdieva, V.A. Sysoev. Experimental observation of four-day variations of radon emanation caused by moon phases // Bulletin of KazNU. Series physical. – 2016. – Vol. 1., No. 56. – P. 120 – 128.

23. V.V. Dyachkov, Yu.A. Zaripova, A.V. Yushkov, A.L. Shakirov, M.T. Bigeldiyeva, K.S. Dyussebayeva, K.E. Abramov. Study of the factor of local accumulation of daughter products of radon decay in the body by the beta-spectrometry // 68th International Conference "NUCLEUS-2018" Fundamental problems of nuclear physics, atomic power engineering and nuclear technologies. – Book of abstracts, 2-6 July, Saint-Petersburg, Russia. – 2018. – P. 207.

24. V.V. Dyachkov, Yu.A. Zaripova, A.V. Yushkov, A.L. Shakirov, M.T. Bigeldiyeva, K.S. Dyussebayeva, K.E. Abramov. Study of distribution of beta-pollution in the city of Almaty // Recent Contributions to Physics – 2018. – Vol. 67(4). – P. 4-10.

25. V.V. Dyachkov, Yu.A. Zaripova, A.V. Yushkov, A.L. Shakirov, Z.M. Biyasheva, M.T. Bigeldiyeva, K.S. Dyussebayeva, K.E. Abramov. A Study of the accumulation factor of the daughter products of radon decay in the surface layer using beta spectrometry // Physics of Atomic Nuclei. – 2018. – Vol. 81(10). – P. 1509-1514.

IRSTI 29.15.29

The first excited $1/2^+$ state in ^{9}Be and ^{9}B

M. Odsuren[1], Y. Kikuchi[2], T. Myo[3, 4] and K. Kato[5,*]

[1]*School of Engineering and Applied Sciences and Nuclear Research Centre, National University of Mongolia, Ulaanbaatar 210646, Mongolia*
[2]*Tokuyama College, National Institute of Technology, Yamaguchi 745-8585, Japan*
[3]*General Education, Faculty of Engineering, Osaka Institute of Technology, Osaka 535-8585, Japan*
[4]*Research Centre for Nuclear Physics (RCNP), Osaka University, Ibaraki 567-0047, Japan*
[5]*Nuclear Reaction Data Centre, Faculty of Science, Hokkaido University, Sapporo 060-0810, Japan*
[*]*e-mail: kato@nucl.sci.hokudai.ac.jp*

Nuclear states observed around threshold energies provide us with interesting problems associated with the nuclear cluster structure [1, 2, 3, 4]. The first excited $J^\pi = 1/2^+$ state of ^{9}Be [5], which is an α+ α + *n* Borromean nucleus, is one of the typical examples in light nuclei. This state of ^{9}Be has been observed as a sharp peak above the ^{8}Be + *n* threshold energy in the photo-disintegration cross section of γ+^{9}Be→ α + α + *n* [6, 7]. The strength of the peak has a strong influence on the reaction rate of the ^{9}Be synthesis. We performed the calculations using an α + α + *n* three-body model [8, 9] and the complex scaling method (CSM), which well reproduces the observed photo-disintegration cross section. However, the result indicates that the $1/2^+$ state shows the *s*-wave virtual-state character of ^{8}Be+*n*. In addition to this problem, we discuss a mirror state problem of the first excite $1/2^+$ state in ^{9}B.

Key words: cluster model, photo-disintegration cross section, virtual state.
PACS numbers: 21.60.Gx, 25.20.-x, 26.20.Np

1 Introduction

Nuclear states observed around threshold energies provide us with interesting problems associated with the nuclear cluster structure [1, 2, 3, 4]. Most of them are also interesting astrophysically from the viewpoint of nucleosyntheses. The first excited $J^\pi = 1/2^+$ state in ^{9}Be [5], which is an α + α + *n* Borromean nucleus, is one of the typical examples in light nuclei.

The reaction rate of the ^{4}He(αn, γ)^{9}Be reaction is crucial to understand the productions of heavy elements. In the α(αn, γ)^{9}Be reaction, a sequential process, ^{4}He(α, γ) ^{8}Be(n, γ) ^{9}Be, has been considered as a dominant one. However, owing to the short life-time of the ^{8}Be ground state (~ 10^{-16} s), a direct measurement of the ^{8}Be(*n*, γ)^{9}Be reaction is impossible. For an alternative way, the cross section of its inverse reaction, ^{9}Be(γ, *n*)^{8}Be, has been measured to deduce the cross section of ^{8}Be(*n*, γ)^{9}Be.

The low-lying $1/2^+$ state have a impact on the reaction rate of ^{8}Be(*n*, γ)^{9}Be in stellar environments. This state of ^{9}Be has been observed as a sharp peak above the ^{8}Be + *n* threshold energy in the photo-disintegration cross section of γ + ^{9}Be→ α + α + *n* [6, 7]. The strength of the peak has a strong influence on the reaction rate of the ^{9}Be synthesis. From a theoretical side, it is interesting to answer how the low-lying $1/2^+$ state of ^{9}Be contributes to the ^{8}Be(*n*, γ)^{9}Be reaction.

We perform the calculations using an α + α + *n* three-body model [8, 9] and the complex scaling method (CSM) [10, 11]. Applying the three-cluster potential, we show that the observed photo-disintegration cross section [6, 7] is well reproduced. And, the result indicates that the $1/2^+$ state shows the s-wave virtual-state character of ^{8}Be + *n*.

In this report, we explain our results of the first excite $1/2^+$ state in ^{9}Be in comparison with those of other previous studies [12 - 17], because it has been a long-standing problem whether the $1/2^+$ state is a resonant or virtual state. In addition to this problem, we discuss a mirror state problem of the first excite $1/2^+$ state in ^{9}B.

In the next section, we will briefly explain the α + α + *n* three-body model [8, 9], and show the results of the photo-disintegration cross section. In Sec. 3, the result of the complex scaling method for the $1/2^+$ state is discussed to show no resonance solutions for ^{9}Be. In Section 4, the $1/2^+$ state in ^{9}B is shown to be obtained as a resonant state, and the comparison of energy levels for ^{9}Be and ^{9}B is discussed. Finally, summary is given in Section 5.

2 Photo-disintegration of ^{9}Be

To understand the origin of a low-energy peak in the photo-disintegration cross section just above the ^{8}Be + *n* breakup threshold energy in ^{9}Be, we investigate the *E*1-transition strength using an α + α + *n* three-body model [8, 9]. The Hamiltonian for the relative motion of the α + α + *n* three-body system for ^{9}Be is given as

$$H = \sum_{i=1}^{3} t_i - T_{cm} + \\ + \sum_{i=1}^{2} V_{\alpha n}(\xi_i) + V_{\alpha\alpha} + V_{PF} + V_3, \quad (1)$$

where t_i and $T_{\rm cm}$ are kinetic energy operators for each particle and the center of mass of the total system, respectively. The interactions between the neutron and the α particle is given as $V_{\alpha n}(\xi_i)$, where ξ_i is the relative distance between them. We here employ the KKNN potential [18] for Vαn. For the α-α interaction $V_{\alpha\alpha}$, we employ a folding potential of the effective NN interaction [19] and the Coulomb interaction:

$$V_{\alpha\alpha}(r) = v_0 \exp(-ar^2) + \frac{4e^2}{r}\,\mathrm{erf}(Br), \quad (2)$$

where $v_0 = -106.09$ MeV, $a = 0.2009$ fm^{-2}, and β = 0.5972 fm^{-1}. The pseudo-potential $V_{PF} = \lambda|\Phi_{\rm PF}\rangle\langle V_{\rm PF}|$ with $\lambda = 10^6$ MeV is expressed by the projection operator to remove the Pauli forbidden states $\Phi_{\rm PF}$ from the relative motion of α-α and α-n.

In the Hamiltonian of Equation (1), two-cluster potentials $V_{\alpha n}$ and $V_{\alpha\alpha}$ are fixed so as to reproduce the observed scattering data of αn and α-α, respectively. Since the antisymmetrization effects are taken into account by the Pauli-potential $V_{\rm PF}$ but a three-cluster exchange effect is not included explicitly in this calculation, we introduce the phenomenological three-cluster potential V_3 to investigate the photo disintegration of ^{9}Be by reproducing the breakup threshold energy into α +α +*n*. The explicit form of V_3 is given by

$$V_3 = v_3 \exp(-\mu\rho^2), \quad (3)$$

where ρ is the hyper-radius of the α + α + *n* system. The hyper-radius is defined as

$$\rho^2 = 2r^2 + \frac{8}{9}R^2, \quad (4)$$

where *r* is the distance between two α-particles and *R* is that between the neutron and the center of mass of the α + α subsystem.

In Figure 1, calculated photo-disintegration cross sections are shown. The dashed and dotted lines are results with and without the three-body potential of v_3 = 1.10 MeV and μ = 0.02 fm. The black solid line represents the cross section calculated by using an attractive three-body potential with $v_3 = -1.02$ MeV. The experimental data below E_γ = 2.2 MeV are taken from References [6, 7]. The arrow indicates the threshold energy of the ^{8}Be(0^+) + *n* channel.

The result calculated with an appropriate strength v3 of the three-cluster interaction well reproduces the cross section peak observed just above the ^{8}Be(0^+) + *n* threshold.

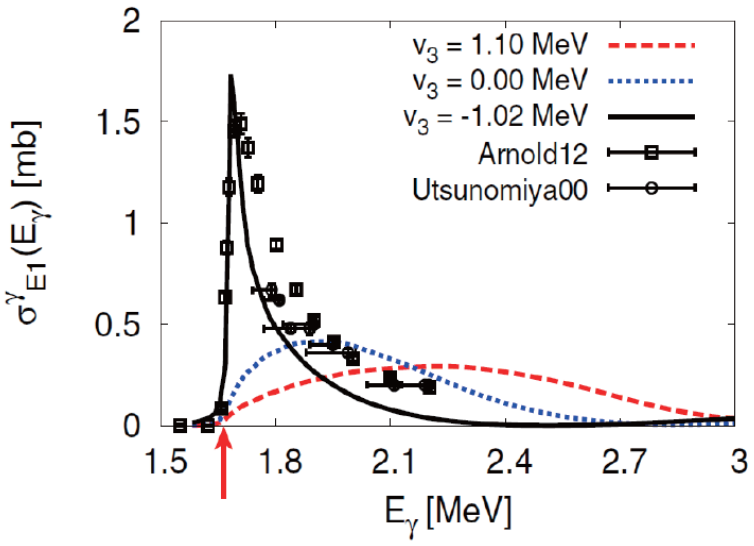

Figure 1 – Calculated photo-disintegration cross sections in comparison with experimental data.

3 The virtual-state property of ^{9}Be ($1/2^{+}_{1}$)

For the problem that the first excited $1/2^{+}$ state in ^{9}Be is resonant or virtual state, we have many studies so far [12 - 17]. To see whether the peak of the photo-disintegration cross section is due to resonances or not, we apply the complex scaling method to the α+ α + n model and search for the $1/2^{+}$ resonant states. The complex-scaled Schrodinger equation is given as

$$H^{\theta}\Psi_J(\theta) = E_J^{\theta}\Psi_J(\theta), \qquad (5)$$

where J is the total spin of the α+α+n system. The complex-scaled Hamiltonian and wave function are

$$H^{\theta} = U(\theta)HU^{-1}(\theta),$$
$$\Psi_J(\theta) = U(\theta)\Psi_J, \qquad (6)$$

respectively. The complex scaling $U(\theta)$ with a real parameter $0 \leq \theta \leq 45^{\circ}$ transforms the relative coordinates as

$$U(\theta); \quad r \rightarrow re^{i\theta}, \qquad R \rightarrow Re^{i\theta}. \qquad (7)$$

The calculated eigenvalue distribution of the $1/2^{+}$ states is shown in Figure 2. The result indicates no resonance solutions for θ = 15°. Although there may exist a resonance solution with a large width, which cannot be solved with θ = 15°, it is not consistent with observed data of the width Γ = 217±10 KeV [5]. And we could not find such a resonant state by the analytical continuation for the three-cluster potential strength [8].

On the other hand, we obtain the resonant solution for the $1/2^{+}$ state in the mirror nucleus ^{9}B, where the same Hamiltonian (Equation (1)) for the α + α + p model with the

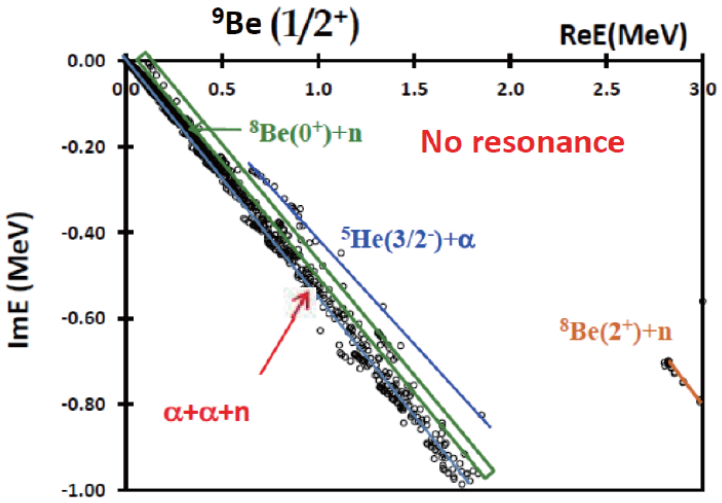

Figure 2 - Energy eigenvalue distribution of 1/2$^+$ states of 9Be measured from the α+α+*n* threshold with scaling angle θ = 15°. The solid, dashed, and dotted lines represent the branch cuts for α+α+*n*, ^{8}Be(0$^+$) + *n*, and ^{5}He(3/2$^-$) + α continua, respectively.

Coulomb interaction for the proton *p* are used. In Figure 3, the 1/2$^+$ resonant state is shown with a circle. This resonance solution is understood to be reproduced by the Coulomb interaction between the valence proton and two α clusters, which does not exist in the α + α + n system.

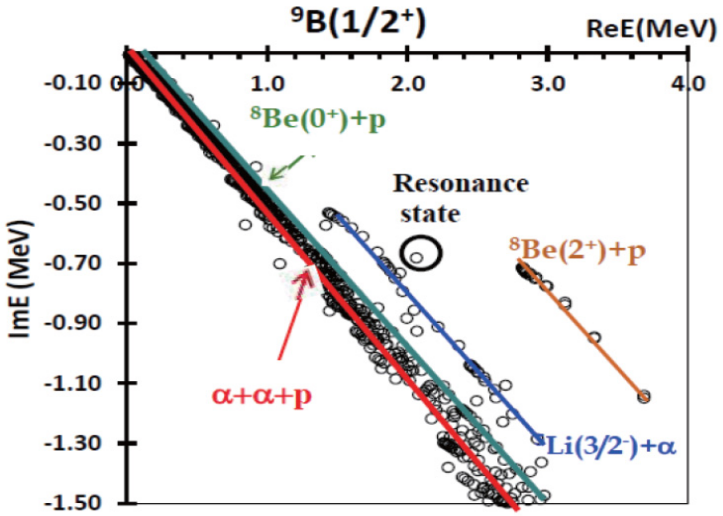

Figure 3 – Energy eigenvalue distribution of 1=2+ states of 9B measured from the α + α + p threshold with scaling angle θ = 15°. The solid, dashed, and dotted lines represent the branch cuts for α + α + p, ^{8}Be(0$^+$) + *p*, and ^{5}Li(3/2$^-$) + α continua, respectively

The virtual state property of the 1/2$^+$ state in ^{9}Be was studied in detail by using the ^{8}Be+*n* model [20-30]. It is confirmed that the virtual state of the neutron *s*-wave is embedded in the continuum without a barrier potential. Furthermore, it is shown that we cannot distinguish virtual state from resonant state in the shape of the cross section peak, when the resonance appears at a very small energy from the threshold.

4 Mirror States in ^{9}Be and ^{9}B

In addition to the $1/2^{+}$ state, low-lying states of ^{9}Be are calculated within the α+ α + n model. The observed photo-disintegration cross sections [6, 7] are shown to be well explained over a wide energy region [9]. The energy levels of ^{9}Be are presented in Figure 4 together with experimental results [5]. The first excited $1/2^{+}$ state does not have correspondence in the present calculation, and the $3/2^{-}_{2}$ state is predicted to be about 1 MeV lower than the experiment. However, other states are well reproduced.

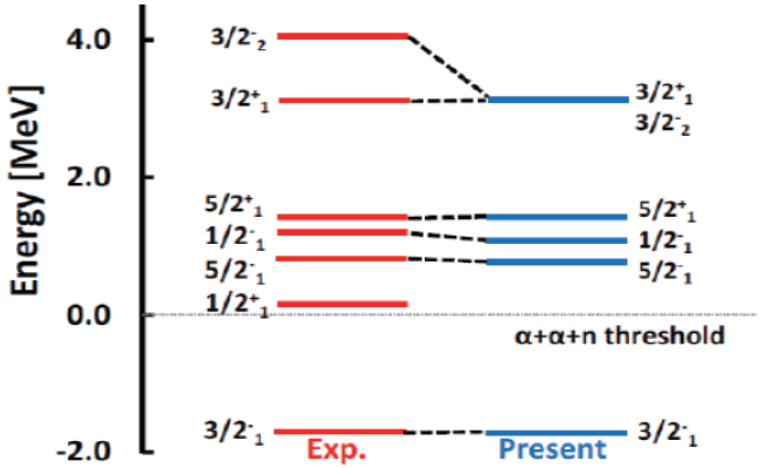

Figure 4 – Energy levels of ^{9}Be. The present calculation is compared with the experimental data taken from Ref.[5]

In Figure 5, we show the present result of energy levels for ^{9}B in comparison with observed data [5]. The low-lying states, which are all resonant states, are well reproduced except for the first excited $1/2^{+}$ state. The calculated state is rather higher than the experimental one.

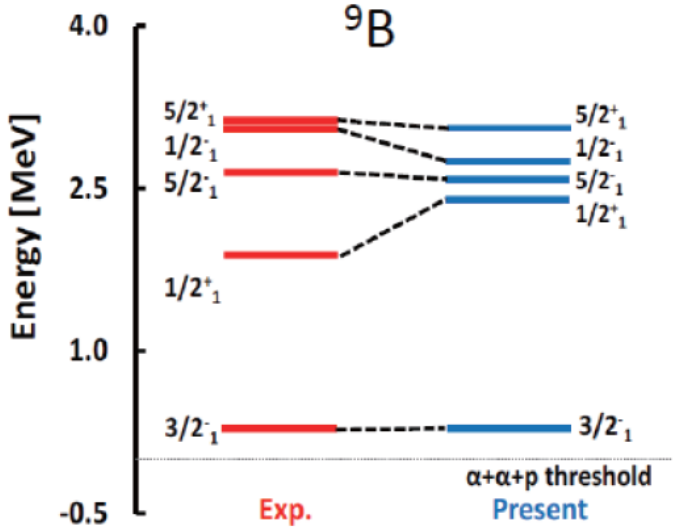

Figure 5 – Energy levels of ^{9}B. The present calculation is compared with the experimental data taken from Ref. [5]

This state of ^{9}B is the mirror of the virtual state in ^{9}Be, which is understood to have the *s*-wave configuration of the neutron around the ^{8}Be (= α+α) core. The Thomas-Ehrman effect [23] suggests that the *s*-wave proton of the mirror nucleus has a weak effect from the Coulomb interaction. Then the energy shift of the *s*-wave proton configuration is expected to be smaller than those of other states. Thus, the present result shows an inverse tendency of the energy relation between the $1/2^{+}$ states in ^{9}Be and ^{9}B.

5 Summary

It has been a long standing problem that the peak of the photo-disintegration cross section observed just above the ^{8}Be+*n* threshold in ^{9}Be causes from the $1/2^{+}$ resonant state or a neuron *s*-wave virtual. The complex scaled α + α + n model shows to reproduces the observed peak of the $1/2^{+}$ state due to a neuron *s*-wave virtual state of ^{8}Be(0^{+}) + *n*. We discussed a mirror state problem of the first excite $1/2^{+}$ state in ^{9}B.

References

1. K. Ikeda, N. Takigawa, H. Horiuchi. The Systematic structure-change into the molecule-like structures in the self-conjugate 4n nuclei // Progress of Theoretical Physics Supplement E. – 1968. – Vol. 68. – P. 464.
2. H. Horiuchi, K. Ikeda, K. Katō. Recent developments in nuclear cluster // Progress of Theoretical Physics Supplement. – 2012. –Vol. 192. – Pp. 1-238.
3. H. Horiuchi, K.Ikeda. Cluster Model of The Nucleus // Cluster Models and Other Topics. – 1987. – P. 1–258.
4. H. Horiuchi, K.Ikeda. A Molecule-like Structure in Atomic Nuclei of ^{16}O* and ^{10}Ne // Progress of Theoretical Physics. – 1968. – Vol.40, No. 2. – P. 277-287.
5. D. R. Tilley, J. H. Kelley, J. L. Godwin, D. J. Millener, J. E. Purcell, C. G. Sheu, & H. R. Weller. Energy levels of light nuclei A=8,9,10 // Nucl. Phys. A. – 2004. – Vol. 745. – P. 155-362.
6. C. W. Arnold, T. B. Clegg, C. Iliadis, H. J. Karwowski, G. C. Rich, J. R. Tompkins, and C. R. Howell. Arnold, C. W., Clegg, T. B., Iliadis, C., Karwowski, H. J., Rich, G. C., Tompkins, J. R., & Howell, C. R. (2012). Cross-section measurement of ^{9}Be(γ,n)^{8}Be and implications for α+α+n→^{9}Be in the r process // Physical Review C. – 2015. – Vol. 85, No. 4. – P. 044605.
7. H. Utsunomiya, S. Katayama, I. Gheorghe, S. Imai, H. Yamaguchi, D. Kahl, Y. Sakaguchi, T. Shima, K. Takahisa, and S. Miyamoto. Photodisintegration of ^{9}Be through the $1/2^{+}$ state and cluster dipole resonance // Phys. Rev. C. – 2015. – Vol. 92, No. 6. – P. 064323.
8. Myagmarjav Odsuren, Yuma Kikuchi, Takayuki Myo, Masayuki Aikawa, and Kiyoshi Katō. Virtual-state character of the ^{9}Be$1/2^{+}$ state in the ^{9}Be(γ,n)^{8}Be reaction // Phys. Rev. C. – 2015. – Vol. 92, No. 1. – P. 014322.
9. Yuma Kikuchi, Myagmarjav Odsuren, Takayuki Myo, and Kiyoshi Katō. Photodisintegration cross section of ^{9}Be up to 16 MeV in the α + α + n three-body model // Phys. Rev. C. – 2016. – Vol. 93, No. 5. – P. 054605.
10. J. Aguilar and J. M. Combes. A class of analytic perturbations for one-body Schrödinger Hamiltonians // Communications in Mathematical Physics – 1971. – Vol. 22, No. 4. – P. 269-279.
11. E. Balslev and J. M. Combes. Spectral properties of many-body Schrödinger operators with dilatation-analytic interactions // Communications in Mathematical Physics – 1971. – Vol. 22, No. 4. – P. 280-294.
12. F.C. Barker and B. M.Fitzpatrick. R-matrix fit to ^{9}Be(γ,n)^{8}Be cross section near threshold // Australian Journal of Physics. – 1968. – Vol. 21, No. 4. – P. 415-421.
13. Hiroshi Furutani Hiroyuki Kanada Tsuneo Kaneko Sinobu Nagata Hidetoshi Nishioka Shigeto Okabe Sakae Saito Toshimi Sakuda Michio Seya. Chapter III. Study of Non-Alpha-Nuclei Based on the Viewpoint of Cluster Correlations // Progress of Theoretical Physics Supplement. – 1980. – Vol. 68. – P. 193-302.
14. P. Descouvemont. ^{9}Be and ^{9}B nuclei in a microscopic three-cluster model // Phys. Rev. C. – 1989. – Vol. 39, No.4. – P.1557.
15. F.C. Barker. The ^{7}Be (p, γ)^{7}B cross section at low energies // Australian Journal of Physics. – 2000. –Vol. 53. – P. 247.
16. O. Burda, P. von Neumann-Cosel, A. Richter, C. Forssen, B.A. Brown. Resonance parameters of the first $1/2^{+}$ state in ^{9}Be and astrophysical implications // Phys. Rev. C. – 201. – Vol. 82, No. 1. – P. 015808.
17. E. Garrido, D. V. Fedorov, and A. S. Jensen. Above thresholds-wave resonances illustrated by the $1/2^{+}$ states in ^{9}Be and ^{9}B // Phys. Lett. B. – 2010. – Vol. 684, No. 2-3. – P. 132-136.
18. R. Álvarez-Rodríguez, A. S. Jensen, E. Garrido, and D. V. Fedorov. Structure and three-body decay of 9Be resonances // Phys. Rev. C. – 2010. – Vol. 82, No.3. – P. 034001.
19. J. Casal, M. Rodríguez-Gallardo, J. M. Arias, and I.J. Thompson. Astrophysical reaction rate for ^{9}Be formation within a three-body approach // Phys. Rev. C. – 2014. – Vol. 90, No. 4. – P. 044304.

20. Y. Koike, E. Cravo, and A. C. Fonseca, in Proceedings of the International Symposium on Clustering Aspects of Quantum Many-Body Systems, Kyoto, Japan, 2001, edited by Ohnishi et al. (World Scientific, Singapore, 2002), p. 65.

21. K. Arai, P. Descouvemont, D. Baye, and W. N. Catford. Resonance structure of ^{9}Be and ^{9}B in a microscopic cluster model // Phys. Rev. C. – 2003. – Vol. 68, No. 1. – P. 014310.

22. V.D. Efros and J.M. Bang. The first excited states of ^{9}Be and ^{9}B // The European Physical Journal A. – 1999. – Vol. 4, No. 1. – P. 33-39.

23. V. D. Efros, P. von Neumann-Cosel, and A. Richter. Properties of the first excited state of ^{9}Be derived from (γ,n) and (e,e′) reactions // Phys. Rev. C. – 2014. – Vol. 89, No. 2. – P. 027301.

24. H. Kanada, T. Kaneko, S. Nagata, and M. Nomoto. Microscopic Study of Nucleon-^{4}He Scattering and Effective Nuclear Potentials // Progress of Theoretical Physics. – 1979. – Vol. 61, No. 5. – P. 1327-1341.

25. E. Schmid and K. Wildermuth. Phase shift calculations on α-α scattering // Nucl. Phys. – 1961. – Vol. 26, No. 3. – P. 463-468.

26. M. Odsuren, Y. Kikuchi, T. Myo, G. Khuukhenkhuu, H. Masui and K. Katō. Virtual-state character of the two-body system in the complex scaling method // Phys. Rev. C. – 2017. – Vol. 95, No. 6. – P. 064305.

27. M. Odsuren, Y. Kikuchi, T. Myo and K. Katō. Photodisintegration cross sections for resonant states and virtual states // Phys. Rev. C. – 2019. – Vol. 99, No. 3. – P. 034312.

28. M. Odsuren, T. Myo, G. Khuukhenkhuu, H. Masui, K. Katō. Analysis of a Virtual State Using the Complex Scaling Method // Acta Physics Polonica B. – 2018. – Vol. 49, No. 3. – P. 319-324.

29. R. G. Thomas. An Analysis of the Energy Levels of the Mirror Nuclei, C^{13} and N^{13} // Phys. Rev. – 1952. – Vol. 88, No. 5. – P. 1109.

30. J. B. Ehrman. On the Displacement of Corresponding Energy Levels of C^{13} and N^{13} // Phys. Rev. – 1951. – Vol. 81, No. 3. – P. 412.

IRSTI 27.35.57

Asymptotic behavior of numerical solutions of the Schrodinger equation

F.M. Pen'kov[1] and P.M. Krassovitskiy [1,2]

[1]*Institute of nuclear physics, 1, Ibragimov Str., 050032, Almaty, Kazakhstan*
[2]*Join institute for nuclear research, 6, Joliot-Curie Str., 141980, Dubna, Russia*
e-mail: fmp56@mail.ru

Many problems of numerically solving the Schrodinger equation require that we choose asymptotic distances many times greater than the characteristic size of the region of interaction. The problems of resonance diffraction for composite particles or the problem of nucleon scattering by nonspherical atomic nuclei are examples of the need to use a large spatial domain for calculations. If the solution to one-dimensional equations can be immediately chosen in a form that preserves unitarity, the invariance of probability (in the form of, e.g., fulfilling an optical theorem) is a real problem for two-dimensional equations. An addition that does not exceed the discretization error and ensures a high degree of unitarity is proposed as a result of studying the properties of a discrete two-dimensional equation.
The problem for scattering of rigid molecules by the disks was successfully solved using an improved sampling scheme that provides the correct asymptotic behavior. Corresponding diffraction scattering curves are of a pronounced resonance nature.

Key words: Numerov's method, resonance diffraction, Babine's principle.
PACS numbers 2.60.−x, 03.65.Nk, 34.50.−s

1 Introduction

In numerically solving problems whose mathematical notation is expressed in terms of the two-dimensional Schrodinger equation, there is the problem of a loss of accuracy for finite difference schemes. It is associated with the need to travel long distances relative to the characteristic size of the potential range. Such situations arise in the scattering of slow particles at long scattering distances or with the scattering of fast particles with pronounced diffraction when we need to go beyond the region of the diffraction shadow in the calculations.

The problems of resonance diffraction for composite particles [1, 2] or the problem of nucleon scattering by nonspherical atomic nuclei are examples of the need to use a large spatial domain for calculations. Expansion in spherical functions in this case loses both physical and mathematical meaning because of the non conservation of the angular momentum in the scattering process. The standard approach, which uses amplitude notation in an explicitly unitary form, thus becomes an inoperative tool. We can, of course, choose a solving scheme based on some averaging of the nonspherical potential (by, e.g., means of folding [3]) and leaving the error of the means of solving without any possibility of analysis. This problem arises not only in the two examples given above, and it is solved in different ways for specific cases in theoretical physics, nanostructure physics, and related fields of chemistry, medicine, and atomic interferometry [4-8].

2 Material and methods

Let us write the Schrodinger equation in a two-dimensional axially symmetric case for a scattering problem (here and below, we use a system of units in which the Planck constant and the Boltzmann constant are 1 in analogy with [4])

$$\Delta\Psi(\vec{r}) - V(\vec{r})\Psi(\vec{r}) = -k^2\Psi(\vec{r}), \quad (1)$$

$$\Delta = \frac{\partial^2}{\partial r^2} + \frac{2}{r}\frac{\partial}{\partial r} + \frac{1}{r^2}\frac{1}{\sin(\vartheta)}\frac{\partial}{\partial\vartheta}\sin(\vartheta)\frac{\partial}{\partial\vartheta}$$

Here, $k^2 = 2mE$ is a wave parameter,E is the energy of the system, and $\Psi(\vec{r}) = \Psi(r,\vartheta)$ is the wave function. Note that the energy in the selected system of units ismeasured in ones that are inverse to the square of thelength. The potential is limited in some area $V = 0$ with $r > r_V$. The asymptotic form of the wave functionin a region greater than some asymptotic radius r_{as} : $r > r_{as} >> r_V$,

$$\Psi(\vec{r}) \to e^{i\vec{k}\vec{r}} + f(\vartheta)\frac{e^{ikr}}{r}\left(1 + O\left(\frac{1}{r}\right)\right),$$

determines scattering amplitude $f(\vartheta)$, which obeys optical theorem [9]

$$\sigma = 2\pi\int_0^\pi |f(\vartheta)|^2 \sin(\vartheta)\, d\vartheta = \frac{4\pi}{k}\operatorname{Im} f(0),$$

where σ is the total cross section. This ratio (the conditionfor invariance of probability) can be used as acriterion of accuracy for the numerical solution to theproblem.We must choose a sufficiently high value of parameter r_{as}that determines the region of the asymptoticsolution in the numerical solution to the scatteringproblem. Asymptotic distances several hundred unitsof the problem's length for characteristic values $r_V = 1-3$and $k \le 30$must extend beyond shadow region $r_{as} > r_V(kr_V)$ in the problem of the quantum scattering of particles on a nonspherical potential [1].

The limiting accuracy of calculations for such distancesis determined by the ignored asymptotic term (i.e., it can be a fraction of a percent). The form of potential $V(\vec{r})$ requires the use of asmall parameter for the sampling step. This ensuresthe accuracy of the solution, but considerably extendsthe estimated time. Two sampling steps are used toadvance the calculations for continuing quantum scatteringstudies on nonspherical potentials [1,2]. For $r \le r_s \approx r_V$, we choose fairly small step $\Delta r = 0.001$, which guarantees sufficient accuracy $O\left((\Delta r)^2\right)$ in the range of potentials, and step $\Delta r_2 = 2^n \Delta r$ with $n \sim 4-5$ for $r > r_s$. However, this choice results in as much as10% deviation in fulfilling the optical theorem. Thesedeviations are much larger than the sampling error $O\left((\Delta r_2)^2\right)$ for finding the wave function. Such anerror in the phase of asymptotic wave function neverthelessresults in considerable deviation from theoptical theorem.

The importance of loss of accuracy can beexpressed in a one-dimensional example. Let us considera one-dimensional free equation for $\varphi = r\Psi$ and its finite difference approximation

$$\frac{d^2}{dr^2}\phi + k^2\phi(r) = 0 \to \frac{\phi(r+\Delta r) - 2\phi(r) + \phi(r-\Delta r)}{(\Delta r)^2} + k^2\phi(r) + O\left((\Delta r)^2\right) = 0.$$

Replacing the value of the function at points $\varphi(r \pm \Delta r)$ with a Taylor expansion, we obtain

$$\frac{\partial^2}{\partial r^2}\varphi(r) + \frac{(\Delta r)^2}{12}\frac{\partial^4}{\partial r^4}\varphi(r) + k^2\varphi(r) + O\left((\Delta r)^4\right) = 0.$$

The solutions to this equation have the form

$$\exp\left(\frac{\sqrt{2}\sqrt{-3+\sqrt{9-3(\Delta rk)^2}}\, r}{\Delta r}\right).$$

Expanding the exponent in a series with respect toΔr, we obtain

$$ikr + \frac{1}{24}ikr(\Delta rk)^2 + O(\Delta r^4). \quad (2)$$

Since this expression is in the exponent, the secondterm can be ignored only if it is small in comparison to unity $\left(\frac{1}{24}kr(\Delta rk)^2 << 1\right)$. This inequality is certainlynot satisfied for very large r. For example, phase term $\frac{1}{24}kr(\Delta rk)^2 = 0.05543\, r$ at $\Delta r = 0.016$, $k = \sqrt{300}$, and becomes equal to 5.5 when $r = 100$. The problem ofthe loss of

accuracy is thus due to the incongruity ofthe exact asymptotic form and the asymptotic behaviorwhen solving the equation in finite differences.The same result can be obtained in general form.Let us find the solution to finite difference equation

$$\frac{\phi(r+\Delta r)-2\phi(r)+\phi(r-\Delta r)}{(\Delta r)^2}+ \\ +k^2\phi(r)=0 \quad , \ldots \qquad (3)$$

by substituting function $\varphi = \exp(ik_{eff}r)$ in it. Thisleads to the equation for k_{eff}:

$$4\sin^2\left(\frac{k_{eff}\Delta r}{2}\right)=k^2(\Delta r)^2.$$

The finite difference equation thus has an exponentialsolution with wave parameter k_{eff}:

$$k_{eff}=2\arcsin\left(\frac{k\Delta r}{2}\right)\Big/\Delta r.$$

Expanding k_{eff} in a series with respect to Δr, we obtain

$$k_{eff}=k+\frac{1}{24}k(k\Delta r)^2+\frac{3}{640}k(k\Delta r)^4+ \\ +\frac{5}{7168}k(k\Delta r)^6+O\left((k\Delta r)^8\right),$$

As expected, the first terms of the series coincidewith Eq. (2).In a similar manner, we can obtain the value of k_{eff} for more complicated problems, e.g., for two-dimensionalSchrodinger equation (1), sampled usingNumerov's method to an accuracy of $O\left((\Delta r)^4\right)$. Wemust in this case solve the following finite difference equation

$$\frac{\left(1+\frac{(k\Delta r)^2}{12}\right)\exp(ik_{eff}\Delta r)-2\left(1+\frac{(k\Delta r)^2}{12}\right)+\left(1+\frac{(k\Delta r)^2}{12}\right)\exp(-ik_{eff}\Delta r)}{(\Delta r)^2}+k^2=0,\ldots \qquad (4)$$

It yields

$$k_{eff}=\frac{2\arcsin\left(\frac{3k\Delta r}{\sqrt{\left(36+3(k\Delta r)^2\right)}}\right)}{\Delta r},$$

without quadratic terms with respect to Δr as a series expansion

$$k_{eff}=k+\frac{1}{480}k^5(\Delta r)^4+O\left((\Delta r)^6\right) \qquad (5)$$

The deviation of the correct asymptotic behavior fromthe solution to Eq. (4) thus occurs at much greater distanceswhen using Numerov's scheme. For example, the value $\frac{1}{480}r_{as}k(\Delta rk)^4$ at $r_{as}=100$ is 0.02, determiningan error of 2% in the unitarity condition whenusing the problem parameters $\Delta r=0.016, k=\sqrt{300}$. Such a scheme can be used for a two-dimensionalequation with twice differentiable interaction potentials.

Unfortunately, it does not work when using potentials with sharp boundaries. We propose introducing small term $-k^2\frac{(k\Delta r)^2}{12}$ into Eq. (3). On the one hand, this term has a low degree ofdiscretization error in the range of potentials; on theother, it is the compensating term for the free equationand brings its discretization error down to $O(\Delta r)^4$:

$$\frac{d^2}{dr^2}\phi+k^2\phi(r)=0\rightarrow\frac{\phi(r+\Delta r)-2\phi(r)+\phi(r-\Delta r)}{(\Delta r)^2}+ \\ +k^2\left(1-\frac{(k\Delta r)^2}{12}\right)\phi(r)=0.$$

In this case, we obtain for k_{eff} the equation

$$k_{eff}=\frac{2\arcsin\left(\frac{k\Delta r}{12}\sqrt{\left(36+3(k\Delta r)^2\right)}\right)}{\Delta r},$$

whose series expansion

$$k_{eff} = k - \frac{1}{720}k^5(\Delta r)^4 + O\left((\Delta r)^6\right),$$

has a numerical factor in front of $(\Delta r)^4$ that is even less than in expansion (5), ensuring 99–97% unitarity withthe most stringent parameters of the problem.

The computational error does not exceed 0.5% in testreductions of the sampling step (down to $\Delta r = 0.008$).

3 Results and discussions

The problem of the scattering of a rigid diatomicmolecule on a thin disk was solved by using the correctasymptotic behavior. The barrier potential of a disk in cylindrical coordinates $\rho = r\cos\vartheta$ and $z = r\sin\vartheta$ is written in the form

$$V_b = \begin{cases} V_{b0}: & \rho \le R \text{ и } |z| \le a/2, \\ 0: & \rho > R \text{ или } |z| > a/2. \end{cases}$$

Parameters V, adetermine the disk size. In analogy with the problem of a rigid moleculepassing through a barrier [4], the potential in Eq. (1) for the model of a rigid molecule has the form

$$V_b(\rho, z + d/2) + V_b(\rho, z - d/2),$$

where parameter $d$corresponds to the size of a scatteredrigid molecule.The difference between the scattering of a moleculeand a point particle equal to its mass is best seen inbackscattering, so not only the scattering cross sectionsof the molecule but also the backscattering cross section for a particle with a mass equal to that of twoatoms are shown in the figures below. This cross sectionmust have the form of monotonic energy and rapidlyshrink at energies above that of potential barrier(the disk potential). Barrier height V_{b0}in the abovecalculations was assumed to be $333.2\text{Å}^{-2}(4000\,K$ fora hydrogen molecule). The figures show the total crosssections along with those into the front and rear hemispheres.The cross section into the front (rear) hemisphereis determined in the same way as the total crosssection, but the limits of integration over the angle arefrom 0 to π/2 (from π/2 to π).

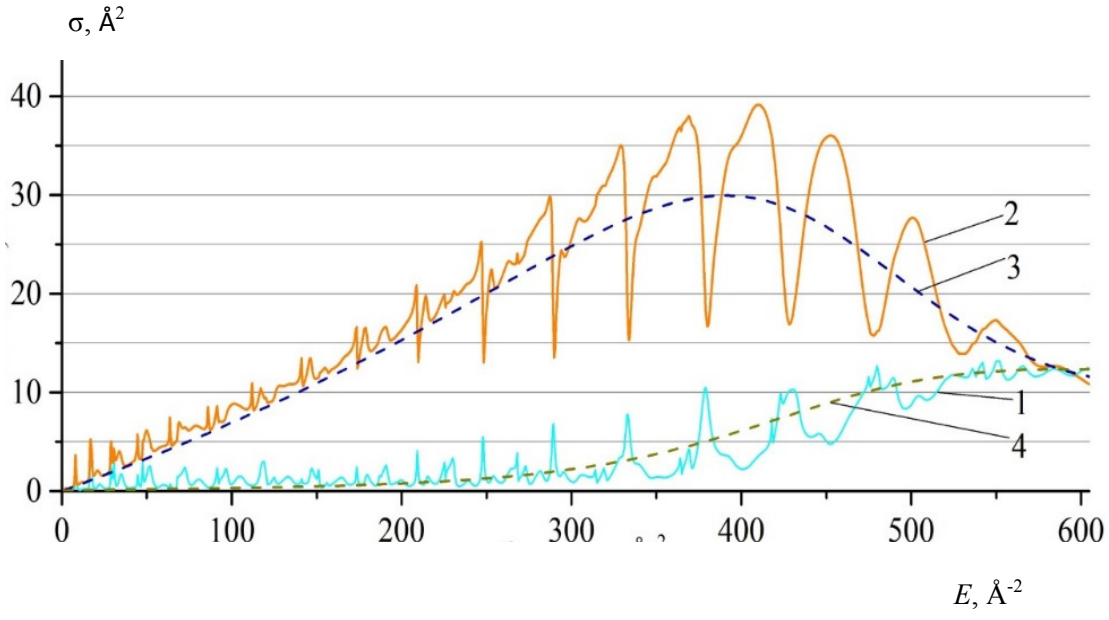

Figure 1 – The scattering cross sections of the hydrogen molecule on the disk at R = 3 Å. 1 – σ_t, 2 – σ_f, 3 – σ_b, 4 – backward scattering cross section for a particle with a doubled hydrogen atom mass

Figure 1 shows the results from calculating thedependence of the total scattering cross section of rigidhydrogen molecule H_2 by a thin disk with a radius of 3 Å and a width of 0.2 Å on the energy. Parameter $d$is0.7416 Å for hydrogen [10]. It can be seen that the backscatteringcross section of the molecule generallyrepeats the pattern of the scattering cross section for anunstructured particle, but it has characteristic resonance deviations.

The diffraction scattering cross sections of rigidberyllium molecule $Be_2$are given for comparison in Figure 2. Parameter d is 2.47 Å [11, 12]. The greater numberof quasi-bound states are due to the greater distancebetween atoms that is observed on the cross section by a large number of resonances. The main dips inthe cross section (resonances) coincide with the positionsof the energy levels in a rectangular one-dimensionalwell with a width of d, just as in the pattern forthe resonant passage of a rigid molecule [4]. This leadsto the differences between the scattering of hydrogenand beryllium molecules observed in the figures. Thenumber of minima in the total scattering cross sectionof a rigid beryllium molecule is much higher.

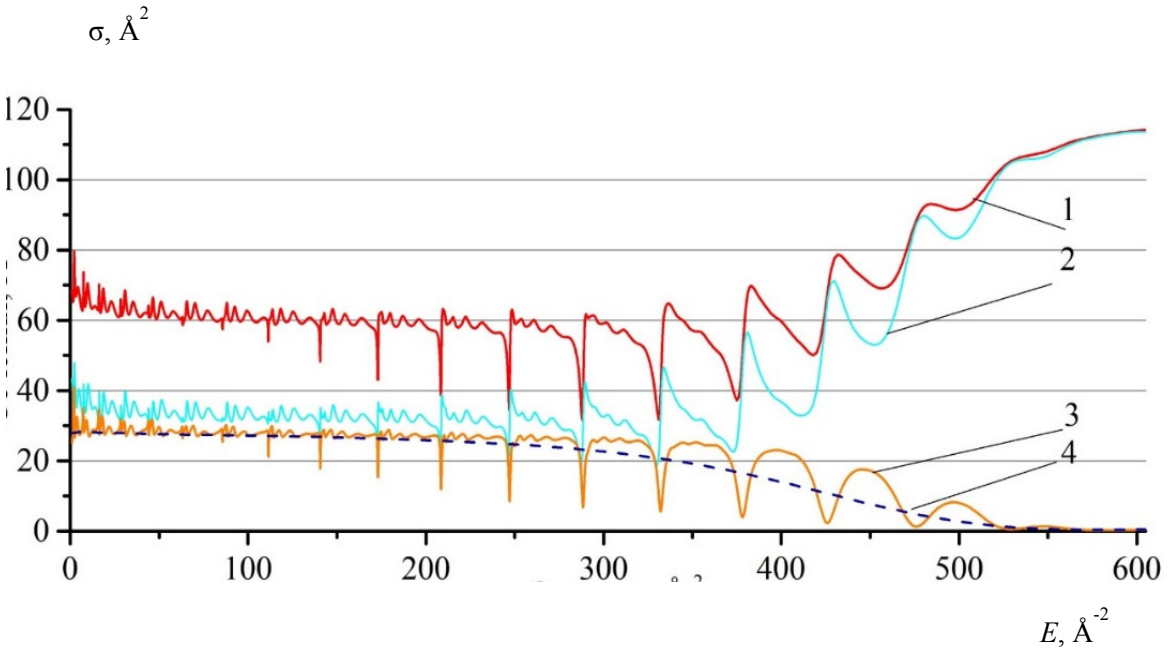

Figure 2 – The scattering cross sections of the Beryllium molecule on the disk at R = 3 Å. Numerical line are liked one in Figure 1.

The calculation of two-dimension scattering at non-symmetrical center can be used for problem of scattering at holes in infinity wall. The Babinet's principle [13] has been used for it. The numerical example is presented by Figure 3.

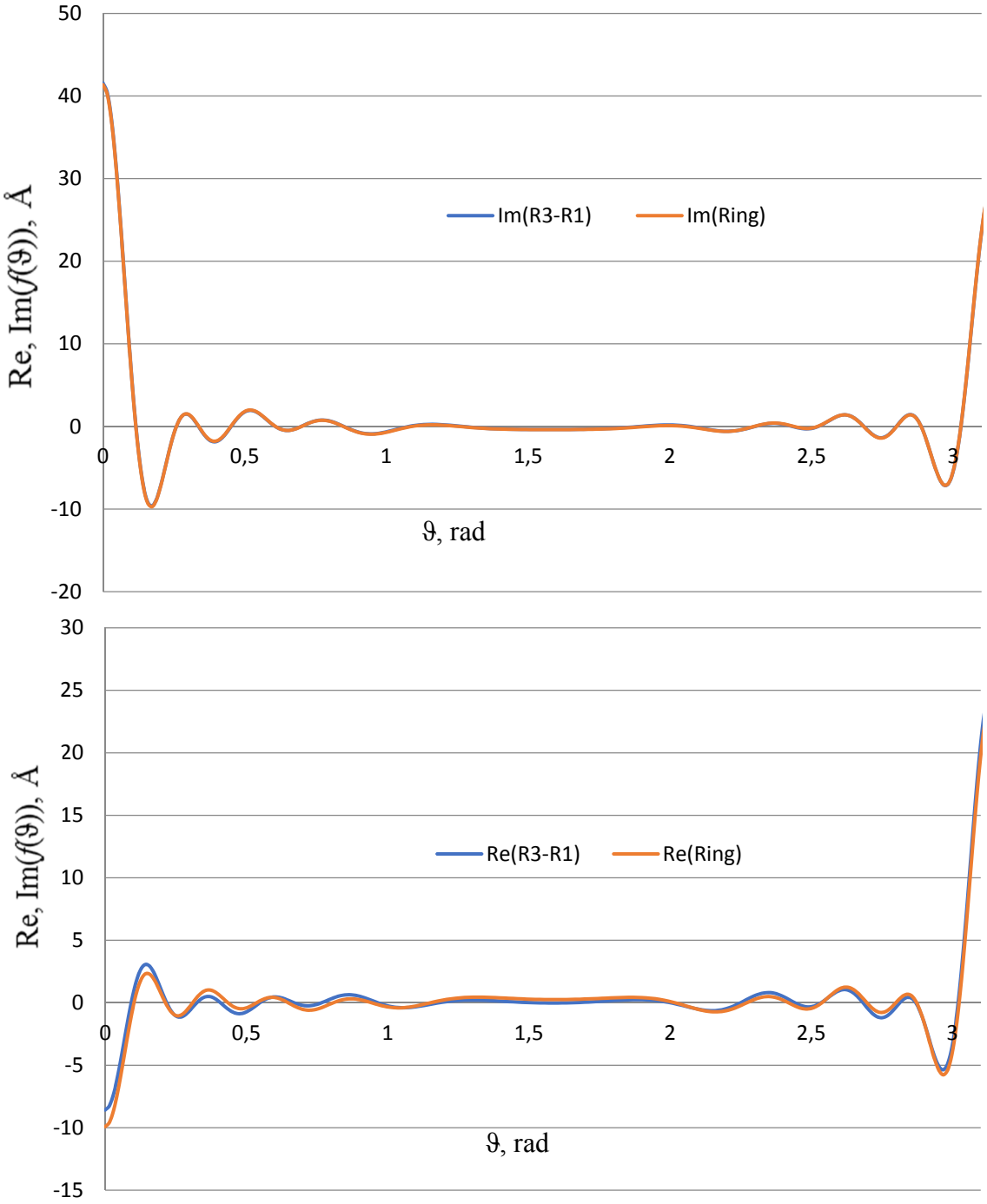

Figure 3 – Comparison of beryllium atom scattering at an energy of 100 $Å^{-2}$. R3 is the scattering on a disk of 3 Å, R1 is scattering on a disk of 1 Å, Ring is scattering on a ring 3 Å wide with a hole of 1 Å.

It can be seem, that calculated scattering on the disk with big radius is equivalent a sum of scattering on ring with external radius which equal big disk's one and little disk with radius which equal hole's one.

The calculation of scattering on hole is presented at Figure 4.

It can seem that the resonance structure is exist here too.

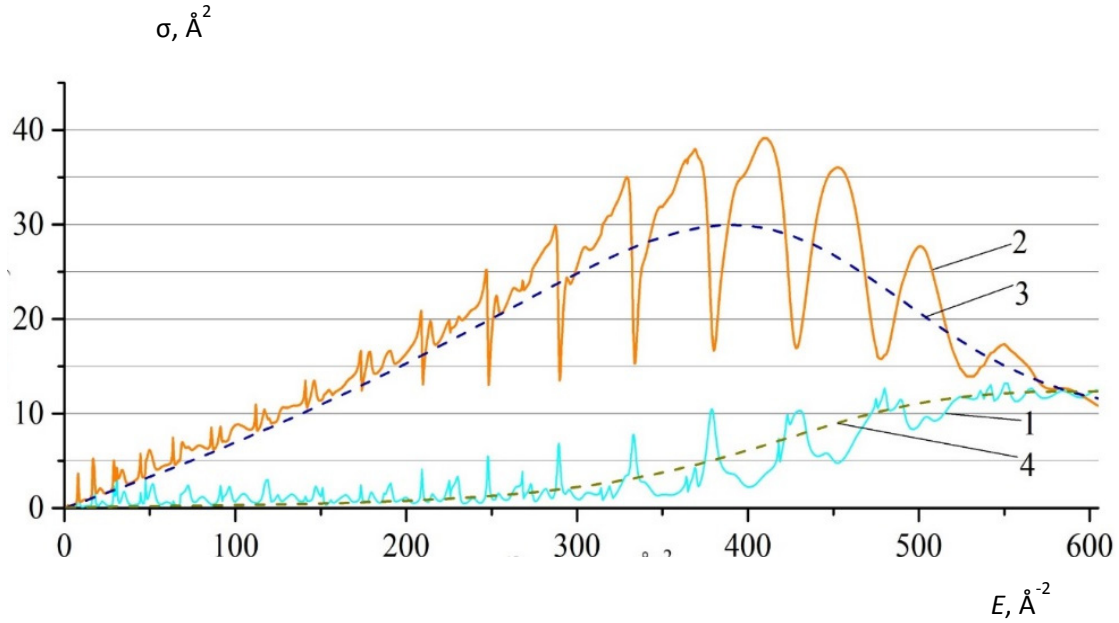

Figure 4 – Diffraction of beryllium on hole R=2 Å.
Numerical line are liked one in Figure 1

4 Conclusions

The problem for scattering of rigid molecules bythe disks was successfully solved using an improvedsampling scheme that provides the correct asymptotic behavior. The result could be useful for analogical topics of investigation [14-22]. Corresponding diffraction scattering curves are of a pronounced resonance nature. The units of the problem length E were determinedby the interaction parameters. A femtometer (fm) isconveniently chosen as units of length in problems ofnuclear physics. The proposed way of correcting for thewave parameter in asymptotic behavior can thus beapplied in different areas that study diffraction using two-dimensional differential equations (e.g., in studyingparticle scattering by nonspherical atomic nuclei).

References

1. P. Krassovitskiy, F. Pen'kov. Quantum scattering by nonspherical objects. // Bull. Russ.Acad. Sci.: Phys.-2017. -Vol. 81, – No. 6. – P. 730-734.

2. G. Satchler, Direct Nuclear Reactions. Oxford: Oxford Univ.Press, – 1983.

3. P. Krassovitskiy, F. Pen'kov. Contribution of resonance tunneling of molecule to physical observables //J. Phys. B. – 2014. – Vol. 47. – No. 22. – P. 225210-225214.

4. R. Mathaes, et al. Non-spherical micro-and nanoparticles: fabrication, characterization and drug delivery applications. // ExpertOpin. Drug Delivery.-2015 – Vol. 12. – No.3. – P. 481-492.

5. A. Ikot, et al. Exact solutions of Schrodinger equation with improved ring-shaped non-spherical harmonic oscillator and Coulomb potential // Commun. Theor. Phys. – 2015. – Vol. 65. – No.5. – P. 569-574.

6. A. Statt, et al. Crystal nuclei in melts: a Monte Carlo simulation of a model for attractive colloids. Mol. Phys.-2015. – Vol. 113. –No. 17-18. – P. 2556-2570.

7. A. Cronin, et al. Optics and interferometry with atoms and molecules. Rev. Mod. Phys. – 2009. -Vol. 81. -No. 3. – P. 1051-1129.

8. L. Landau, E. Lifshitz. Kvantovaya mekhanika (nerelyativistskaya teoriya) (Quantum Mechanics: Non-Relativistic Theory), Moscow: Nauka, – 1989. – P. 583.

9. Spravochnik khimika (Chemistry Handbook), Moscow–Leningrad: GNTI Khim. Lit., – 1966, – Vol. 1. – P. 338.

10. W. Jinlan, et al. Density functional study of beryllium clusters with gradient correction. // Phys.: Condens. Matter. – 2001. – Vol. 13. – P. L753-L758.

11. J. Merritt, et al. Beryllium Dimer—Caught in the act of bonding // Science. – 2009. – Vol. 324. – No. 5934. – P. 1548.

12. M. Born, E. Wolf. Principles of Optics. Cambridge: Cambridge University Press, – 1999.

14. A. Gusev, et al. Adiabatic representation for atomic dimers and trimers in collinear configuration // Physics of Atomic Nuclei. – 2018. – Vol. 81, – No 6. – P. 911-936.

15. A. Gusev, et al. Metastable states of a composite system tunneling through repulsive barriers // Theoretical and Mathematical Physics. -2016. – Vol. 186. – No.1.- P. 21-40.

16. O. Chuluunbaatar et al. Quantum transparency of barriers and reflection from wells for clusters of identical particles // Bull. Russ.Acad. Sci.: Phys. – 2018. – Vol. 82. – No. 6. – P. 648-653.

17. O. Chuluunbaatar et al. Solution of quantum mechanical problems using finite element method and parametric basis functions // Bull. Russ.Acad. Sci.: Phys. – 2018. – Vol. 82. – No. 6. – P. 654-660.

18. A. Gusev, et al. Resonant tunneling of a few-body cluster through repulsive barriers. // Physics of Atomic Nuclei. – 2014. – Vol. 77. – No. 3. – P. 389-413.

19. A. Gusev, et al. Parametric bases for elliptic boundary value problem // Journal of Physics Conference Series. – 2018. – Vol. 965. – P. 012016-1-7.

20. A. Gusev, et al. Symbolic-numerical algorithms for solving elliptic boundary-value problems using multivariate simplex lagrange elements // Lecture Notes in Computer Science. – 2018. – Vol. 11077. – P. 197-213.

21. A. Gusev, et al. “Interpolation hermite polynomials for finite element method // EPJ Web of Conferences. – 2018. – Vol. 173. – P.03009.

22. S. Vinitsky, et al. Three-body scattering model: diatomic homonuclear molecule and atom in collinear configuration // Proceedings of SPIE. – 2017. – Vol. 10337. – P. 103370j.

IRSTI 29.05.27

The fundamental equation of the field theory in De Sitter pulse space

R.M. Ibadov* and S.N.Murodov

Department of Theoretical Physics, Samarkand State University,
University blv. 15, 140104,
Samarkand, Republic of Uzbekistan
**e-mail: ibrustam@mail.ru*

The fundamental equation of the field theory in De Sitter pulse 5-dimensional space is obtained. The wave function, subordinated to this equation in usual space-time, doubles. One of these functions, probably to consider as the candidate on "the Phantom field" responsible for expansion of the Universe with acceleration. The cross sections of $e^-e^- \to e^-e^-$, $e^-e^+ \to e^-e^+$ and $e^-e^+ \to \mu^-\mu^+$ processes at high energies calculated taking into account polarized initial and final particles. Is estimated contribution FM to cross-section sections. Some experimental consequences are predicted. In all these calculations the polarization of particles be taken into account. The Lagrangian of quantum electrodynamics with the fundamental mass is chosen as an effective interaction Lagrangian. All the calculations are made in the Euclidian space, the transfer to the ordinary pseudoeuclidian space is established in the final expressions only. The approach has been based on the assumption that the momentum space possesses the geometric structure of a de Sitters pace of constant curvature. A key role has been be assigned to this constant radius of curvature.

Key words: field theory, De Sitter pulse, cross sections, quantum field theory.
PACS numbers: 10, 04.20.-q, 03.67.Lx, 04.62. + V, 02.30.Ик

1 Introduction

This work continues earlier researches of the academician of Kadyshevsky V.G. and its pupils [1,2] towards constructing a consistent new Quantum Field Theory (QFT) with fundamental mass (FM) M, defining a hypothetical but universal scale in the region of ultrahigh energies. From a theoretical point of view the fundamental mass M and corresponding the fundamental length $\ell = \hbar/Mc$ are supposed to play a major role such as Planck's constant $\hbar$, the speed of light c or Newton's gravitational constant $\varkappa$. The existence of so-called ultra-violet divergences, i.e., infinitely large values, arising as a result of direct application of equations QFT in area of very small space-time distances, or equivalently, to the region of very high energies and pulses is one of lacks of standard QFT. There were ideas about presence of a new universal constant dimension of mass or length in nature [3,4,5,6], which would fix the certain scale in the field of high energies or on small space-time distances because of the purpose to give the decision of this problem in the most various contexts. They testify only that the modern high-energy physics still far will defend from that boundary behind which can be shown new geometrical properties of space-time. From a position of today it is represented to many theorists rather probable, that the "true" theory of the field, capable to give the adequate description of all interactions of elementary particles, will be at least renormalized by Lagrange theory having local gauge supersymmetry. It is asked, whether such scheme can contain such a parameter as the fundamental length? The future experiments can give the answer to this question only. However, numerous attempts to construct more general QFT, proceeding from such parcels, did not give essential results. This failure is probable speaks that for today the mathematical theory of spaces which geometry only "in small" differs from (pseudo) Euclidean geometry is not developed almost and, especially, in similar kinds of spaces the mathematical device adequate to requirements QFT is not advanced. But, the output from the created situation is prompted by QFT. As it is known, within the framework of this

theory space-time description is completely equal in rights with the description in terms pulse-power variables. If the theory is formulated in pulse representation fields, sources, Green's functions and other attributes of the theory appear certain in four-dimensional (pseudo) Euclidean p-space. This modified quantum field theory has an elegant geometrical basis: in momentum representation one faces a momentum space corresponding to de Sitter space of curvature radius [1,2,7,8]. The approach developed earlier has been based on the assumption that the momentum space possesses the geometric structure of a de Sitters pace of constant curvature. A key role has been be assigned to this constant radius of curvature.

2 Theory

Experimental Detection of the new fundamental scale testifying to existence specific atoms of space-time, would mean, that in knowledge of a nature the new step, commensurable on the value with opening quantum properties of a matter is made. According to modern data, if the constant ℓ also exists then if submits to restriction $\ell \leq 10^{-19}$ cm. This boundary still extremely far will defend from "Planck lengths" ℓ_{Planck}~10^{-33} cm, determining spatial scales of effects of quantum gravitation. And, certainly, it is impossible to exclude, that in process of overcoming an enormous interval $10^{-19} - 10^{-33}$ cm will be open the new physical phenomena and laws, associate with new "scale of a nature" – fundamental length ℓ.

In the papers cited [9], the key role was played by the following geometric idea: to construct QFT providing an adequate description of particle interactions at super high energies, one should write down the standard field theory in the momentum representation, and then pass it from the Minkowski p-space to the de Sitter p-space with a large enough radius.

The de Sitter space has a constant curvature. Depending on its sign there are two possibilities

$$p_0^2 - p_1^2 - p_2^2 - p_3^2 + p_5^2 \equiv g^{KL} P_K P_L = M^2; \quad (1)$$

$$K, L = 0,1,2,3,5$$

(positive curvature: $g^{00} = -g^{11} = -g^{22} = -g^{33} = g^{55} = 1$)

$$p_0^2 - p_1^2 - p_2^2 - p_3^2 - p_5^2 \equiv g^{K\square} P_K P_L = -M^2; \quad (2)$$

$$K, L = 0,1,2,3,5$$

(negative curvature: $g^{00} = -g^{11} = -g^{22} = -g^{33} = -g^{55} = 1$).

The non-Euclidean Lobachevsky imaginary 4-space (2) is also called the Lobachevsky imaginary 4-space. It is natural that QFT based on momentum representation of the form (l)-(2) must predict new physical phenomena at energies $E \geq M$. In principle, the parameter may turn out to be close to the Planck mass

$$M_{Planck} = \sqrt{\frac{\hbar c}{\kappa}} \approx 10^{19} \text{ GeV}.$$

Then, the new scheme should include quantum gravity. The standard QFT corresponds to the "small" 4-momentum approximation

$$|p_0|, |\vec{p}| \ll M, \quad p^5 = g^{55} p_5 \cong M,$$

which formally can be performed by letting $M \to \infty$ (flat limit). Such features of the considered generalization of the theory as geometricity and minimality are intriguing. This is due to the fact that the Minkowski momentum 4-space having a constant zero curvature is a degenerate limiting form of each of the spaces with constant nonzero curvature (l)-(2).

If we substitute in (2) standard

$$p_\mu = i\hbar \frac{\partial}{\partial x^\mu}$$

and

$$p_5 = i\hbar \frac{\partial}{\partial x^5}$$

receive the quantum version of the de Setter equations (2) in five-dimensional field equation

$$\left[\frac{\partial^2}{\partial x^\mu \partial x_\mu} - \frac{\partial^2}{\partial x_5^2} - \frac{M^2 c^2}{\hbar^2}\right] \Phi(x, x^5) = 0, \quad (3)$$

$$\mu = 0,1,2,3.$$

We deliberately use in (3) the normal units to emphasize those three universal constants $\hbar$, c and M are grouped into one parameter-fundamental length $\ell = \hbar/Mc$. Eq. (3) may be considered as the "fundamental" equation of motion. It is natural to

extend the term "fundamental" to eq. (3) itself (for short f.e.). All the fields independent of their tensor (or spinor) character must obey eq. (3) since similar universality is inherent in the "classical" prototype, i.e. – de Sitter p-space (2). As applied to scalar, spinor, vector and other fields we shall write down the five-dimensional wave function $\Phi(x,x^5)$ in the form $\varphi(x,x^5)$, $\psi_\alpha(x,x^5)$, $A_\mu(x,x^5)$,.. . The field theory based on f.e. (3) turns out to be more consistent and more general than the scheme developed in the de Sitter p-space (2). Thus, by virtue of (2) the 4-momentum components should obey the constraint

$$p^2 = p_0^2 - \vec{p}^2 \geq -M^2,$$

which does not follow from eq. (3). Indeed, passing in (3) to a mixed (p,x^5) representation we get the equation

$$\left[p^2 + M^2 + \frac{\partial^2}{\partial x_5^2}\right]\Phi(p,x^5) = 0, \qquad (4)$$

having a solution at all p^2 including the region $p^2 + M^2 < 0$. Consequently, $p^5 = \sqrt{p^2 + M^2}$ now takes both real and pure imaginary values. For further application let us define this quantity as a generalized function

$$p^5 = \sqrt{p^2 + m^2 + i0} =$$

$$= \begin{cases} \sqrt{p^2 + M^2}\,, & \text{if } p^2 + M^2 > 0 \\ i\sqrt{p^2 + M^2}\,, & \text{if } p^2 + M^2 < 0 \end{cases} \qquad (5)$$

with (5) one can easily write down the general solution of (4)

$$\Phi(p,x^5) = \cos\left(x^5\sqrt{p^2 + m^2 + i0}\right)\Phi(p,0) +$$

$$+ \frac{sin\left(x^5\sqrt{p^2+m^2+i0}\right)}{\sqrt{p^2+m^2+i0)}}\frac{\partial\Phi(p,0)}{\partial x^5}, \qquad (6)$$

where the "initial data" of $\Phi(p,0)$ and $\frac{\partial\Phi(p,0)}{\partial x^5}$ are determined at all values of 4-momenta. The Fourier transformation of (6), results in the formal solution of fundamental equation (3)

$$\Phi(x,x^5) = \frac{1}{(2\pi)^{3/2}}\int e^{-ipx}\,d^4p\Phi(p,x^5) = \frac{1}{(2\pi)^{3/2}}\int e^{-ipx}d^4p \times$$

$$\times\left\{\cos\left(x^5\sqrt{p^2 + m^2 + i0}\right)\Phi(p,0) + \frac{sin\left(x^5\sqrt{p^2+m^2+i0}\right)}{\sqrt{p^2+m^2+i0)}}\frac{\partial\Phi(p,0)}{\partial x^5}\right\}. \qquad (7)$$

To compensate growing terms

$ch(\sqrt{-p^2 - M^2}x^5)$ and $sh(\sqrt{-p^2 - M^2}x^5)$

and thus to give the meaning to integral (7), the arbitrary function $\Phi(p,0)$ and $\frac{\partial\Phi(p,0)}{\partial x^5}$ should obey at least the exponential conditions of decreasing in the region

$$p^2 + M^2 < 0 \text{ as } p \to \infty.$$

In other words, $\Phi(p,0)$ and $\frac{\partial\Phi(p,0)}{\partial x^5}$, satisfying the above criterion, form a class of functions which admits a correct formulation of the Cauchy problem for f.e. (3) with respect to the variable x^5

$$\left[\frac{\partial^2}{\partial x^{\text{м}}\partial x_{\text{м}}} - \frac{\partial^2}{\partial x_5^2} - M^2\right]\Phi(x,x^5) = 0, \qquad (8)$$

$$\Phi(x,x^5)\big|_{x^5=0} = \frac{1}{(2\text{p})^{3/2}}\int e^{-ipx}\Phi(p,0)d^4p, \qquad (9)$$

$$\frac{\partial}{\partial x^5}\Phi(x,x^5)\big|_{x^5=0} =$$

$$= \frac{1}{(2\text{p})^{3/2}}\int e^{-ipx}\frac{\partial\Phi(p,0)}{\partial x^5}d^4p. \qquad (10)$$

It should be noted that if we would develop the Euclidean version of QFT, the f.e. would have the form

$$\left[\frac{\partial^2}{\partial x_n^2} + \frac{\partial^2}{\partial x_5^2} + M^2\right]\Phi(x,x^5) = 0, \qquad (11)$$

$$n = 1,2,3,4$$

the region $p_n^2 > M^2$, would be an analog to $p^2 + M^2 < 0$ and the condition of correctness of the relevant Cauchy problem for f.e. (10) would require the initial data in the p-representation, $\Phi(p,0)$ and $\frac{\partial\Phi(p,0)}{\partial x^5}$, to decrease exponentially outside the sphere $p_n^2 = M^2$. Thus, the fundamental mass M in some sense should play the role of the cutoff parameter in the ultraviolet region.

3 Results and discussion

Let us explain why one should pose the Cauchy problem for f.e. with respect to the coordinate x^5 and just in the correct formulation. The point is that the Cauchy date $\Phi(p,0)$ and $\frac{\partial\Phi(p,0)}{\partial x^5}$ are the fields defined in the four-dimensional space-time. Their number depends on the order of the differential equation (8) with respect to the variable x^5. If the Cauchy problem (8-10) is correct, the f.e. solution is given by the Fourier integral (7), being unique by construction. Consequently, there is a one-to-one correspondence

$$\Phi(x,x^5) \leftrightarrow \binom{\Phi(x,0)}{\partial\Phi(x,0)/\partial x^5}. \qquad (12)$$

In other words, the statement that to each field in the 5-space there corresponds its wave function $\Phi(x,x^5)$, obeying f.e. (3), implies that each of these fields in the usual space-time is described by the wave function with a doubled number of components

$$\binom{\Phi(x,0)}{\partial\Phi(x,0)/\partial x^5} = \binom{\Phi_1(x)}{\Phi_2(x)}. \qquad (13)$$

We should like to note that having placed the Cauchy problem equation (3) for with respect to the coordinate x^5 and just in the correct formulation in the basis of QFT, in fact, we have introduced a new concept of the field, which is not equivalent to the notion of the field developed in the theory with constant curvature momentum space.

From here we see that fields are doubled. It appears the field $\Phi_2(x)$ participates only in interactions. Due to it there are new members in diagrams. Then, it is natural to assume that the initial data obey the Lagrangian equations of motion following from the action principle

$$S = \int d^4xL\left[\Phi(x,0), \frac{\partial\Phi(x,0)}{\partial x^5}\right]. \qquad (14)$$

The basic problem of the new theory was is to construct explicit expressions for the Lagrangians $L\left[\Phi(x,0), \frac{\partial\Phi(x,0)}{\partial x^5}\right]$ in physically interesting cases, to clarify the meaning of additional field variables and to extract new physical effects in the region of super-high energies $E \geq M$. Partially, this problem has been solved earlier [3-6, 17-20]. Thus, a doubled number of field degrees of freedom specific of the new scheme disappears as $M \to \infty$. Hence, specifically,

$$\lim_{M\to\infty} L\left[\Phi(x,0), \frac{\partial\Phi(x,0)}{\partial x^5}\right] = L[\Phi(x,0)]. \qquad (15)$$

Certainly, if in formulating the Cauchy problem we imposed the initial conditions at an arbitrary fixed value

$$x^5 = const,$$

then all our conclusions would be the previous ones and the formulae would undergo trivial changes. For instance, there would appear the following expression for the action

$$S = \int_{x^5=const} d^4xL\left[\Phi(x,x^5), \frac{\partial\Phi(x,x^5)}{\partial x^5}\right]. \qquad (16)$$

Thus, we receive actions for scalar, Dirac and vector fields. Basically symmetry of the equation of motion-simultaneously is the symmetry of action. Therefore it is satisfied

$$\partial S/\partial\, x^5 = 0.$$

Let's consider for a neutral scalar field $\Phi(x,x^5)$ particles with zero mass. According to

$$\Phi(x,x^5) \simeq e^{iMx^5}\Phi(x,0),$$

in the limit $M \to \infty$

$$\varphi(x,x^5) \simeq e^{iMx^5}\varphi(x,0). \qquad (17)$$

The choice of a solution of f.e. in the form of (13) corresponds to the following initial data (5,6)

$$\varphi(x,x^5) \equiv \varphi(x),$$

$$-\frac{i}{M}\frac{\partial\varphi(x,x^5)}{\partial x^5} \equiv X(x).$$

We can conclude that of the two field functions $\varphi(x) = \varphi(x,0)$ and $X(x) \equiv -\frac{i}{M}\frac{\partial\varphi(x,0)}{\partial x^5}$ used in the new formalism to describe a massless neutral scalar field only the first $\varphi(x)$ is physical since only it has a fully adequate equation of motion. The field $ч(x)$ is pure auxiliary. It has no its own equation of motion and its values fully depend on its values of the field $\varphi(x)$.

Maybe, in future $X(x) \equiv -\frac{i}{M}\frac{\partial\varphi(x,0)}{\partial x^5}$ will be interpreted as a candidate on the "Phantom field", responsible for acceleration of expansion the Universe.

Thus, the action for the field of no interacting neutral scalar particles with zero mass has in our approach the following form:

$$S = \frac{1}{2}\int d^4x \left[\frac{\partial\varphi(x,x^5)}{\partial x_{\text{м}}}\frac{\partial\varphi(x,x^5)^+}{\partial x_{\text{м}}} + \left|-i\frac{\partial\varphi(x,x^5)}{\partial x^5} - M\varphi(x,x^5)\right|^2\right] =$$

$$= \tfrac{1}{2}\int d^4x \left[\frac{\partial\varphi(x)}{\partial x_{\text{м}}}\frac{\partial\varphi(x)^+}{\partial x_{\text{м}}} + M^2\big(X(x)-\varphi(x)\big)^2\right]. \qquad (18)$$

This expression satisfies the correspondence principle with the standard theory since at $M \to \infty$ by virtue of $\varphi(x,x^5) \simeq e^{iMx^5}\varphi(x,0)$

$$S = \tfrac{1}{2}\int d^4x \frac{\partial\varphi(x)}{\partial x_{\text{м}}}\frac{\partial\varphi(x)^+}{\partial x_{\text{м}}}. \qquad (19)$$

The action of the free Dirac field can be written also in the configuration 5-space:

$$S = \frac{1}{2}\int d^4x \ \{\,\bar{\Psi}(x,x^5)\big(i\,\hat{\partial} + M\big)\left(-\frac{i}{M}\frac{\partial}{\partial x^5}\Psi(x,x^5)\right) + \overline{\left(-\frac{i}{M}\frac{\partial}{\partial x^5}\Psi(x,x^5)\right)}\ \big(i\,\hat{\partial} + M\big)\Psi(x,x^5) -$$

$$-M\ \overline{\left(-\tfrac{i}{M}\tfrac{\partial}{\partial x^5}\Psi(x,x^5)\right)}\left(-\tfrac{i}{M}\tfrac{\partial}{\partial x^5}\Psi(x,x^5)\right) - \bar{\Psi}(\,x,x^5)(M + \tfrac{(i\,\partial)^2}{M^2})\Psi(x,x^5)\ \},\qquad (20)$$

where the spinor field $\psi(x,x^5)$ satisfies f.e. (3). According to our general concept, $\psi(p)$ and $\varphi(p)$ are Fourier transforms of the initial data

$$\Psi(x,0) = \Psi(x), -\frac{i}{M}\frac{\partial}{\partial x^5}\Psi(x,0) \equiv X(x)$$

sufficiently decreasing in the region

$$p^2 + M^2 < 0 \text{ as } |p| \to \infty.$$

The same procedure, we applied in the scalar and spinor cases, leads to the following total action integral of the electromagnetic field in QFT with the fundamental mass

$$S = -\tfrac{1}{4}\int d^4x \left\{\begin{matrix} \mathrm{F_{KL}}(x,x^5)F^{KL}(x,-x^5) + \\ +2\left|\frac{\partial A^{\text{м}}(x,x^5)}{\partial x^5} - iM\mathrm{A_5}(x,x^5) - \frac{\partial \mathrm{A_5}(x,x^5)}{\partial x^5}\right|^2 \end{matrix}\right\} \qquad (21)$$

where

$$\mathrm{F_{KL}}(x,x^5) = \frac{\partial}{\partial x^K}\left(e^{-iMx^5}\mathrm{A_L}(x,x^5)\right) - \frac{\partial}{\partial x^L}\left(e^{-iMx^5}\mathrm{A_K}(x,x^5)\right) \quad L,K = 0,1,2,3,5. \qquad (22)$$

The Lagrangian density in (21) is not a pure local expression in the configurational 5-space but a quantity invariant under local gauge transformations of the 5- potential

$$e^{-iMx^5}\mathrm{A_K}(x,x^5) \to e^{-iMx^5}\mathrm{A_K}(x,x^5) - \\ -\frac{\partial}{\partial x^K}\left(e^{-i\,Mx^5}\Lambda(x,x^5)\right) \qquad (23)$$

$$K = 0,1,2,3,5.$$

where the function $\Lambda(x,x^5)$, like $\mathrm{A_K}(x,x^5)$, obeys f.e. (3). Naturally as usual,

$$\partial S/\partial\, x^5 = 0.$$

Could the advanced theory be free from ultra-violet divergences? At the present we do not have the final answer what this issue is concerned, however, we can calculate effective cross sections of some processes which are in good agreement with experiments, and this allows to estimate the contribution of fundamental mass. Research in building consecutive new QFT with fundamental weight are resulted also in publications [13, 14, 15, 16].

4. Conclusions

Further, we investigated the phenomenological (experimental) consequences of such a quantum field theoretical model [17,18,19,20]. Calculations of cross sections corresponding to various basic processes are executed to the second order. On the basis of the QFT with FM, calculations of cross sections for processes such as $e^-e^- \to e^-e^-$, $e^-e^+ \to e^-e^+$ and $e^-e^+ \to м^-м^+$ have been carried out by taking into account the polarization of particles. Is estimated contribution FM to cross-section sections. Some experimental consequences are predicted. In all these calculations the polarization of particles can be taken into account.

References

1. V. G. Kadyshevsky. On the theory of quantized space-time // JETF. – 1961. – Vol. 41. –No.6. – P.1885-1894 (in Russian).
2. V.G. Kadyshevsky. Fundamental length hypothesis and new concept of Gauge vector field // Nuclear Physics B. – 1978. –Vol. 141. – No. 4. – P. 477-496.
3. W. Heisenberg. Introduction to the unified field theory of elementary particles. // Iters. Publ. UK, – 1966. – 192 p.
4. C.N. Yang. On quantized space-time // Phys. Rev. – 1947. –Vol. 72. – P.874.
5. A.A. Komar, M.A. Markov. An example of a field theory with indefinite metric in Hilbert space II // Nucl. Phys. – 1959. –Vol. 12. – P.190.
6. J. D. Bjorken. Identification of elementary forces and Gauge theories. Harwood Academic Publisher. – 1979. – 701 p.
7. M.V. Chizhov, A.D. Donkov, R.M. Ibadov, V.G. Kadyshevsky, M.D. Mateev. Quantum field theory and a new universal high energy scale Dirac fields // Nuovo Cimento. – 1985. – Vol. 87A. – No.3. – P.350.
8. M.V. Chizhov, A.D. Donkov, R.M. Ibadov, V.G. Kadyshevsky, M.D. Mateev. Quantum field theory and a new universal high energy scale. Gauge vector fields // Nuovo Cimento. – 1985. – Vol. 87A. – No.4. – P.375.
9. R.M. Ibadov, V.G. Kadyshevsky. New formulation of quantum field theory with fundamental mass // Proceedings 5th International Symposium on Selected Topics in Statistical Mechanics, Dubna, World Scientific, Singapore. – 1989. – P. 131.
10. R.M. Ibadov, V.G. Kadyshevsky. About transformations of supersymmetry in theories of a field with fundamental mass // Preprint JINR. – 1986. –Vol. 86. – P. 4.
11. R.M. Ibadov, V.G. Kadyshevsky. The new point of view on auxiliary fields in supersymmetric models // Works of VIII International Meeting on problems of the Quantum Theory of a Field. Alushta. Dubna, – 1988. – Vol. D2-87-798. – P.141;
12. R. M. Ibadov, V. G. Kadyshevsky. On supersymmetry transformations in the field theory with a fundamental mass // JINR Preprint. – 1986. – Vol. R2-86-835.
13. V. G. Kadyshevsky, M. D. Mateev, V. N. Rodionov, A. S. Sorin. Towards a geometric approach to the formulation of the standard model // Dokl. Phys, 51. – 2006. – P. 287.
14. V.G. Kadyshevsky, M.D. Mateev, V.N. Rodionov, A.S. Sorin. Towards a maximal mass model // arXiv: 0708.4205v1[help-ph]. E-print. – 2007. – Vol. 150. – P. 1-28.

15. V.G. Kadyshevsky, M.D. Mateev, V.N. Rodionov, A.S. Sorin. Towards a geometric approach to the formulation of the standard model // Dokl.Phys. – 2006. – Vol. 51. – P. 287-290.

16. V. N. Rodionov, G. A. Kravtsova. An algebraic PT-symmetric quantum theory with a maximal mass // Physics of Particles and Nuclei. -2016. – Vol. 47. – No. 2. – P. 135-156.

17. A.D. Donkov, R.M. Ibadov, V.G. Kadyshevsky, M.D. Mateev, M.V. Chizhov. Some experimental consequences of a hypothesis about fundamental length // Izvestiya AN USSR, Series Physics. – 1982. –Vol. 46. – No. 9. – P.1772.

18. R.M. Ibadov, M.V. Chizhov. Application of quantum electrodynamics with in the fundamental length to high power process // Izvestiya AN UZSR, Series Physics and Mathematics. – 1983. –Vol. 5. – P.38.

19. R.M. Ibadov. Deep elastic scattering of electron in nucleons and fundamental lengths // Izvestiya AN UZSR, Series Physics and Mathematics, – 1984. – Vol. 3. – P.44.

20. R. Ibadov, S. Tuhtamishev, U. Khodjaeva. Some experimental consequences hypotheses about fundamental mass // European Science. – 2017. –Vol. 24. – No.2. – P. 6-13.

IRSTI 45.43.41

Obtaining of aluminum nano-powders by thermal treatment

G. Paskalov

Plasma Microsystems LLC, 22002 Linda Dr., Torrance CA 90503,
Los Angeles, California USA
e-mail:paskal567@yahoo.com

It is known that the formation of a dispersed phase under extreme conditions (high temperatures and process speed) leads to the formation of a non-equilibrium structure of particles. Therefore, the first to attract attention are technologies based on pulsed processes with high rates of change in the thermodynamic parameters of the system. One of these promising methods for obtaining a wide range of nano-powders of inorganic materials is the technology based on the process of electrical explosion of a conductor (EVP, EVP technology) [1-5]. Unfortunately, this method is not applicable on industrial scales. In this thesis, production of Al nanoparticles by hydrogen reduction of metal chlorides in gas phase was studied. Nanoparticles have unique properties not found in bulk or micron-scale materials. These enable new products or reduced use of raw materials. Metal nanoparticle production has been studied widely, but especially for coated metal particles, research of coating mechanisms and economic production methods is still needed. The used method combines a high yield, a high production rate, low production costs, high particle quality, and a good range of available particle number average diameters and other properties. Control of the product parameters has been carried out by using a special quenching system and plasma reactor configuration. Highly hydrogen enriched Al nanopowder were collected in metal form and tested for different applications.

Key words: RF plasma, hydrogen, nano-aluminum, quenching.
PACS numbers: 52.77.–j, 82.33.Xj

1 Introduction

Metals, such as aluminum have high combustion energies and have been employed as energetic additives in propellant and explosives [6-9]. Ultrafine aluminum powder with the size range of 300 to 15000 Angstroms may be produced by electrical explosion of aluminum wire in the hydrogen and argon containing media. Mass spectroscopy and thermal desorption analytical methods of powder produced from wires showed that aluminum powder consisted of spherical particles with distorted crystal lattice, and contained amorphous phase, surface gases, and gases inside of particle volume of about 5 to 7% mass [10]. Those results are in agreement with our results. However, the electrical explosion procedure of Al powder is not applicable for industrial production of such powder. Different chemical processes and properties of metals saturated with argon and hydrogen and aluminum hydrides are described in literature [11-16]. The properties of chemical aluminum hydride, AlH_3 (calorific value of about 9500 kcal/kg) are well known. The drawback of conventional materials is their low stability when exposed to the atmospheric air and poor temperature stability, tending to dissociate at temperature above 105 C^0. The powder produce by using RF plasma process has a similar size range, but narrower particle size distribution. The plasma process of saturation of aluminum powder with hydrogen is not well known and the efforts have been made to increase the calorific value and stability of the product [17-20].

2 Experimental set up

The RF plasma system used for this experiment consist five major parts: inductive plasma torch, reactor, feeder, quenching device and powder collector. The plasma torch include gas forming block, water-cooled copper discharge chamber, exit nozzle and is mounted on the top of the reactor. Plasma gas system is capable to mix argon and hydrogen at differ-

ent ratio starting from pure argon and ending by pure hydrogen. Exit nozzle is combined together with the powder input device. High purity aluminum powder (average particle size of 5 μm) is feeding into plasma stream by quartz feeder and water cooled probes with the controller and carrier gas system. The following quenching units were used: 28 mm diameter and 92 mm diameter cylinder type quench devices; spraying liquid argon directly into the reactor and a quench system combining liquid argon spraying and a heat exchanger consisting of a 40 turn coil. Calorific value was determined using a Parr Model 1261 calorimeter; the unburned aluminum was determined by solution with sodium hydroxide on the residue in the calorimeter using and analyses by Perkin Elmer ICP 3000. The hydrogen was determined using a LECO CHN 1000 instrument.

3 Calculation and theoretical predictions

The following parameters were calculated: surface area of the quenching components, quenching rate of the product on water-cooled surfaces, quenching rate of the product with liquid argon spray in the reactor, thickness of the collected powder on the quenching surfaces and cartridge filter. Variable parameters are: initial Al powder rate, argon-hydrogen ratio of plasma gas, Al powder quality, RF discharge power, plasma gas flow rate, carrier gas flow rate, and quenching rate. Plasma processed aluminum powder can contain approximately 2.2 times more hydrogen than chemically obtained AlH_3 [11]. Oxidation of this hypothetical substance is as follows:

$$2(AlH_{6.7}) + 4.85O_2 = Al_2O_3 + 6.7\ H_2O$$

The thermal effect of this reaction is 1435 kcal/mol or 21300 kcal/kg. Molecular hydrogen is absorbed on the surface of the melted aluminum particles. The hydrogen then dissociates into atoms and diffuses into the depth of the metal. The atomic nature of hydrogen diffusion in metals was experimentally verified during the research of hydrogen diffusion in a deuterium mixture. Having diffused into the metal, the gas is distributed among atoms of metal. The absorption of hydrogen by aluminum is endothermic. This is why the amount of absorbed hydrogen increases with the increase of temperature and reaches a peak at 2000 to 3000 K. Thus, hydrogen absorbed by aluminum is present in various states, such as:

1. Dissolved in the metal,
2. Segregated of imperfections of the crystal structure,
3. Absorbed on the surface of micro-cavities and on the particles of secondary phases,
4. Accumulated in micro-cavities in molecular form,
5. Creates metal hydrides,
6. Interact with secondary phases,
7. Dissolved in hydride of metal,
8. Dissolved in amorphous metal,
9. Dissolve in amorphous hydride of metal.

Hydrogen may exist in various states inside ultra-fine aluminum powder. However, it is the atomic hydrogen that provides the greatest improvement in available power. A hydrogen saturated aluminum powder with the formula of ($AlH_{6.7}$), has a theoretical Specific Calorific Power (SCP) above 20000 kcal/kg. Quantum theory restricts the degree of saturation of crystalline aluminum with hydrogen above AlH_3. These restrictions are removed by the transition of aluminum into an amorphous state through thermal treatment of Al powder in hydrogen RF plasma at atmospheric pressure.

4 The process and experimental results

The technology is based on direct vaporization of powdered aluminum in an RF hydrogen plasma discharge at atmospheric pressure. The resulting matrix is rapidly quenched into ultra-fine aluminum powder. SCP is not directly measured in bomb calorimeter. Standard procedure includes the burning of samples and measurement of temperature increase. The coefficient of bomb calorimeters and accurate weight of samples are taken into consideration to calculate the SCP. If the weight of incombustible components is deducted from the total weight of the sample, the SCP of combustible component can be obtained. Of course, the more content of incombustible component in the samples such as oxides, the grater the difference between SCP of sample and SCP of combustible component. One of the typical plasma sample (FM2-1) content: Al = 51.4%; Total Al = 69.5%; free carbon = 2.15%. SCP presents the total calorific value for both combustible (0.64 gr.) and incombustible (0.36 gr.) components in 1 gram of sample: 3799 (Al) + 168 cal (C) + 2995 cal (H_2) = 6962 cal. The combustible components should include: 0.514g (Al) + 0.0215g(C) + 0.1045g (H_2) = 0.64 g. The content of H_2 is calculated based on SCP of the sampleFM2-1. SCP of 1 gram of combustible components in the sample FM2-1 based on experimental data: 6962: 0.64 =10878 cal/g = 19577 BTU/lb. The composition of combustible components in sample FM2-1 is 80.31% (Al) + 3.3% (C) + 16.33% (H_2) = 100%. The gross formula for produced

combustible components is Al*5.5H_2*0.08C. In case the hydrogen in the sample FM2-1 is in atomic state, the 0.037g of H would provide the same 2995 cal as 0.1045 g of molecular hydrogen. The combustible components would include: SCP for all combustible components in 1 gram of sample: 3799 cal (Al) +168 cal(C) + 2995 cal (H) = 6962 cal. The combustible components would include: 0.514g (Al) + 0.0215g(C) + 0.037g (H) = 0.5725 g. The composition of combustible components in sample FM2-1 would be: 89.8% (Al) + 3.75 %(C) + 6.45% (H) = 100 %. SCP for all combustible components for sample FM2-1 assuming the atomic state of Hydrogen would be: 6962: 0.5725 = 12160 cal/g = 21888 BTU/lb.

There are several stages of Aluminum powder processing in plasma reactor:

Stage I (Heating process) includes:

a – heating of solid particles from T_0 to T_{melt};

b – melting of particles;

c – heating of the melted particles from T_{melt} to $T_{boiling}$;

d – evaporation of Al particles;

e – heating of Al vapor from T_{boil} to T_{plasma};

f -dissociation of Al molecules/clusters;

and g – ionization of Al atoms.

Stage II (cooling process) includes:

a – bulk or volume recombination of Al ions;

b – association of Al atoms in Al molecules;

c – formation of clusters and nucleation in amorphous states;

d – capture of Hydrogen by Al particles both on its surface and in its body;

e – increase of the particle size in amorphous state;

f – increase of hydrogen content;

g – formation of crystal lattice of Al particles;

h – stopping the increase of the Al particle size in crystal form;

i – release of most captured hydrogen

and j – final cooling of the solid particles.

In order to produce Al particles saturated with hydrogen and interrupt the increase of particle size (i.e. to fix the particle in its meta-stable form) the quenching procedure is required. The A-type samples were obtained as a consequence of quenching of Al powder on cooled surface after stage II-f (see above) and before stage II-g. The B-type samples were obtained by volume liquid Argon quenching of Al particles after stage II-c and before stage II-d. The quality of the plasma processed aluminum depends of quenching procedure. The quenching rate has a decisive importance for retention of captured hydrogen. The volume quenching procedure is widely used in plasma-chemical processes. Most plasma-chemical products have meta-stable form, which is achieved by rapid quenching.

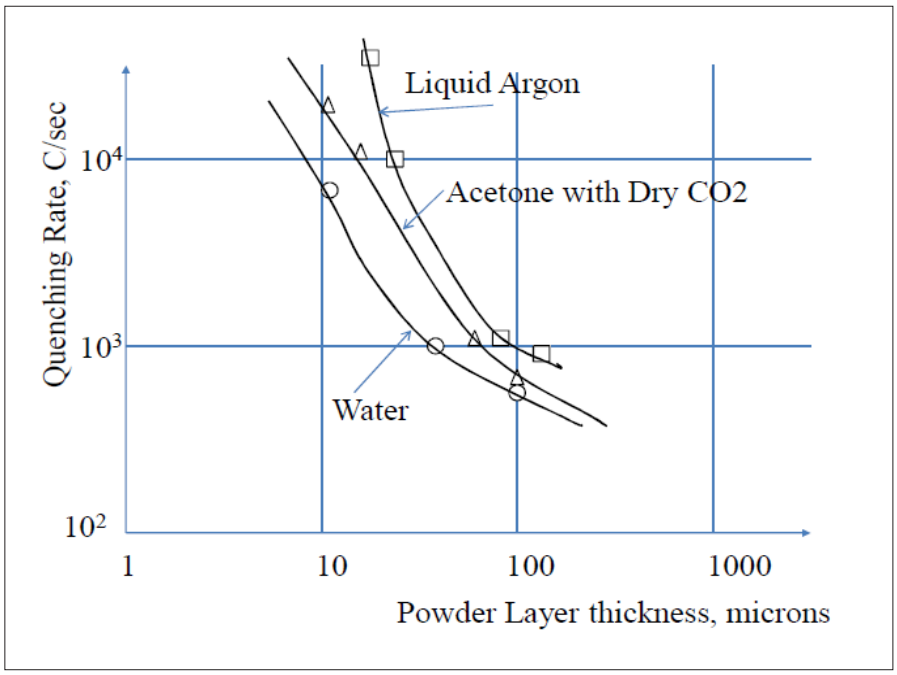

Figure 1 – Quenching Rates for the Liquid Cooled Reactor using: liquid Argon, acetone with dry CO_2 and water

Rapid solidification can be achieved by imposing a high cooling rate (103 – 109 C^0/sec) for the layer thickness not more than 10 microns. When the powder layer thickness becomes more than 10 microns, the quantity of produced powder per surface unit is increased, but the quenching rate goes down to 103 C^0/sec (see Figure 1 and Figure 2) and the upper layers of powder on the well cooled metallic surface release the captured Hydrogen. Brushing off the 100 microns thick layer led to a mixture of a high quality 10 microns layer with a "bad" quality 90 microns upper layer powder in the same sample. We apply this quenching procedure to the RF plasma method of saturation Al powder with Hydrogen and fixation of saturated Al powder in its meta-stable state. The quenching rate for three different types of cooling substances is shown in Figure 1. The following tests were performed on each sample: Aluminum content, % mass (indicate the efficiency of the Aluminum Hydrogen reaction); Hydrogen content, % mass (indicate how much Hydrogen is trapped in Aluminum particles); Carbon content, % mass (indicate impurities from other sources); Oxygen content, % mass (indicate the stability of the product) and Specific calorific power (SCP), kcal/kg (indicate the quality of the product) and Nitrogen content, % mass. As a result, the average quantity of captured Hydrogen in was about 1 % to 3.2% (see Table 1).

Figure 2 – SEM of aluminum – hydrogen saturated powder

Typical SEM of the sample is shown in Figure 2. Average particle size is 250 nm. Surface area is approximately 40 m^2/g (based on BET analysis). It is important to know the stability of the hydrogen saturated aluminum powder. The experiment was performed in special calorimeter, which could control the gas extraction depends of the sample temperature. The temperature was increased by 10 degrees per minute. Typical hydrogen release curve is shown in Figure 4. The material is very stable up to the temperature of 600 C^0.

The degree of the saturation of Al particles by Hydrogen depends of the quenching rate and is shown in Figure 3.

The best technique for the scale up to industrial production was determined. The necessary plasma power for Al powder (initial particle size 1 to 10 microns) rate equal of 1 g/sec will be in the range

of 16 to 18 kW. Taking in account that the total efficiency of RF generator, RF torch and the heat transfer from plasma to the solid-liquid Al particles is about 10%, we have determined that RF power output of the production system could be in the range of 160 to 175 kW.

Table 1 – Experimental data on the amount of elements for different samples.

Name	FM2-11	FM2-12	FM2-13	FM2-14
Calorific Value, BTU/lb	11884	11259	11922	12855
Total Aluminum, %wt	96.76	97.85	96.31	98.05
Unburned Aluminum, % wt	5.46	3.52	2.44	2.30
Hydrogen, % wt.	3.18	0.86	0.78	0.44

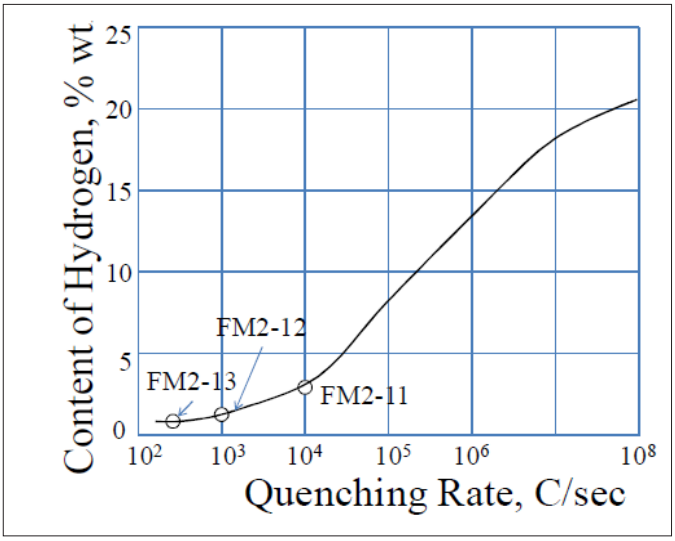

Figure 3 – The degree of the hydrogen saturation vs quenching rate for FM2-11, FM2-12 and FM2-13

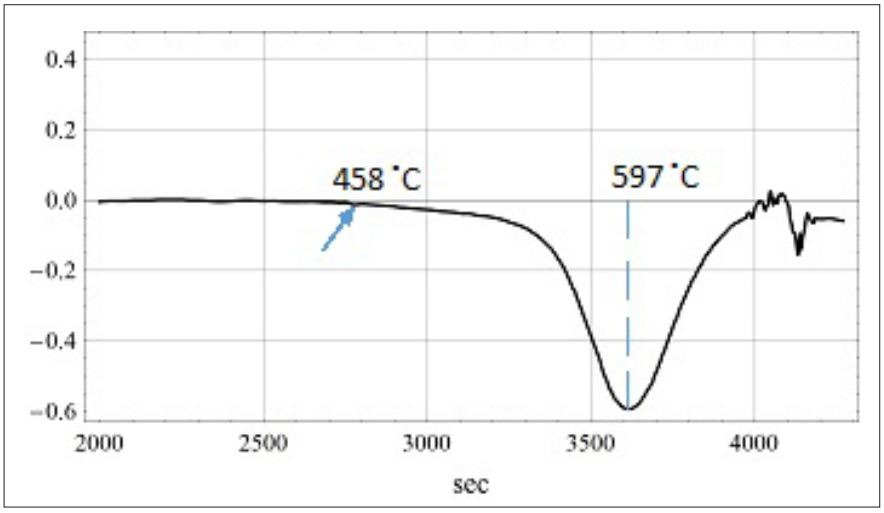

Figure 4 – Typical Hydrogen release curve

5 Conclusions

The technology to produce a new high energy hydrogen saturated aluminum powder using RF plasma process at atmospheric pressure is successfully demonstrated. Standard methods of product analysis such as bomb calorimeter, derivatograph and differential scanning calorimeter (DSC) need to be modified to provide adequate analysis for meta-stable Al powder. The measured quantity of captured Hydrogen was 3.18% wt. Heat of combustion for combustible components of produced Al powder was in the range of 10878 to 12160 cal/g. This value overcome the SCP of chemical AlH_3 and can be increased up to 20000 cal/g. The optimum processing conditions were ascertained, and the best techniques for scale up to industrial production of 8 lbs/Hr of AlH* powder at 160 to 175 kW RF plasma system were determined.

References

1. F. Tepper, M. Lerner, D. Ginley. Nanosized alumina fibers // Bulletin American Ceramic Society. – June 2001. – Vol. 60. – P.57.

2. M. I. Lerner, V. V. Shamanskii, G. G. Savel`ev, T. A. Yurmazova. Chemical reactions between metal and active gases in the electric explosion of wires for the production of nanopowders // Mendeleev communication. – 2001. – Vol. 11. – No. 4. – P.159 – 161.

3. F. Tepper, L. Kaledin, D. Ginley, C. Curtis, A. Miedaner, T. Rivkin, M. Lerner. Characteristics of nano-metal and nano-ceramic precursors // Proceedings of the American Society for Composites, Technical Conference. – 2001. – Vol. 16. – P.376 – 387.

4. S. Tarasov, A. Kolubaev, S. Belyaev, M. Lerner, F. Tepper. Study of friction by nanocopper additives to motor oil // Wear. – 2002. – Vol. 252. – P.63 – 69.

5. F. Tepper, M. Lerner, D. Ginley. Metallic nanopowders // Dekker Encyclopedia of Nanoscience and Nanotechnology. – Marcel Dekker, Inc., N. Y., – 2004. – P. 1921 – 1933.

6. R.A. Yetter et al. Proc. Comb. Inst. – 2009. –Vol. 32. –P. 1819-2838.

7. P.P. Edwards, V.L. Kuznetsov, W.I.F. David, N.P. Brandon. Hydrogen and fuel cells: towards a sustainable energy future // Energy Policy. -2008. – Vol. 36. -Pp. 4356-4362.

8. V.C.Y. Kong, F.R. Foulkes, D.W. Kirk, J.T. Hinatsu. Development of hydrogen storage for fuel cellgenerators. i: Hydrogen generation using hydrolysishydrides // Int. J. Hydrogen Energy. -1999. –Vol. 24. – Pp. 665-675.

9. C.R. Jung, A. Kunddu, B. Ku, J.H. Gil, H.R. Lee, J.H. Jang. Hydrogen from aluminium in a flow reactor for fuel cell applications // J. Power Sources. -2008. –Vol. 175. – Pp. 490-494.

10. G.V. Ivanov et al. Self-propagating sintering of ultra-dispersed metallic powders //Report of Russian Academy of Science, Tech. Phys. – 1982. Pp. 873-875.

11. L.M. Sorokin. Evalation of energy of ultradispersed substance type Al*nAr// Physics and Chemistry of Material Treatment. -1991. – No.1. –P. 1.

12. D. Milcius et al. Behavior of hydrogen implanted during physical vapor deposition in Al, Mg and MgAl films // Materials Science. – 2004. -Vol. 10. -No. 3. – Pp. 217-220.

13. P. Escot Bocanegra, C. Chauveau, I. Gokalp. Experimental studies on the burning of coated and uncoated micro and nano sized aluminum particles // Aerospace Science and Technology. -2007. –Pp. 33 – 38.

14. G.G. Savel'ev, A. Yurmazova, A.I. Galanov, S.V. Sizov, N.B. Danilenko, M.I. Lerener, F. Tepper, L. Kaledin. Adsorption capacity of nanoscale fibrous alumina // Tomsk Politech. University Bulletin. – 2004. – Vol.307. – No1. – Pp.102 – 107. (in Russian).

15. Y. Huang, G.A. Risha, V. Yang, R.A. Yetter. Effect of particle size on combustion of aluminum particle dust in air // Combustion and Flame. – 2009. –Vol. 5 – P.13.

16. J. Duan, J. Coagulation by hydrolysing metal salts // Gregory Adv. Colloid Interface Sci. -2003. –Vol. 100–102. Pp. 475-502.

17. E. S. Caballero, J. Cintas, F.G. Cintas, J. M. Cuevas, J. M. Gallardo. A new method for synthetizing nanocrystalline aluminium nitride via a solid-gas direct reaction // Powder Technology. – 2015. –Vol. 287. –Pp. 341-345.

18. L. Soler, J. Macanas, M. Munoz, J. Casado. Aluminum and aluminum alloys as sources of hydrogen for fuel cell applications // Power Sources. -2007. –Vol. 169. -Pp. 144-149.

19. C.R. Jung, A. Kunddu, B. Ku, J.H. Gil, H.R. Lee, J.H. Jang. Hydrogen from aluminum in a flow reactor for fuel cell applications // J. Power Sources. -2008. –Vol. 175. _Pp. 490-494.

20. L. Soler, A.M. Candela, J. Macanás, M. Mu˜noz, J. Casado. In situ generation of hydrogen from water by aluminum corrosion in solutions of sodium aluminate // Journal of Power Sources. – 2009. –Vol. 192. -Pp. 21-26.

IRSTI 29.19.17

Analysis and identification of platinum-containing nanoproducts of plasma-chemical synthesis in a gaseous medium

D.V. Schur*, An.D. Zolotarenko, Al.D. Zolotarenko, O.P. Zolotarenko, M.V. Chimbai, A.D. Zolotarenko, N.Y.Akhanova and M. Sultangazina

[c]*Institute of Problems of Materials Science, National Academy of Sciences of Ukraine, 3, Krzhizhanovskogo str., 03142, Kiev, Ukraine*
**e-mail: dmitry.schur@gmail.com*

This article studies a nanoproduct that is formed by simultaneous plasma-chemical evaporation of graphite and platinum. It was shown that the resulting deposits under different synthesis conditions have a similar and well-defined structure and consist of two main parts (core and enclosing bark). The structure of both parts is investigated at the micro- and nanoscale levels. The products of synthesis and similar products obtained without the use of platinum has been compared. The distribution of platinum in synthesis products is studied. It is proved that the atoms of the platinum catalyst influence the process of formation of the deposit. Namely, it stimulates the formation of a deposit where the deposit core containing platinum-containing bundles of CNT exists as an independent core that does not have a strong connection with the deposit shell. It is found that differential-thermal analysis of CNM in air by the methods of TG, DTG, DTA allows to reveal insignificant differences in the heat resistance of different carbon nanostructures, and thus it can be used for their identification. Such studies are of great importance for the synthesis of platinum-containing catalysts for fuel cells and other chemical industries.

Key words: plasma-chemical synthesis, platinum nanostructures, deposit, CNTs.
PACS numbers: 61.48.De, 52.40.Hf.

1 Introduction

Platinum-containing carbon nanostructures can now be used not only in the design of fuel cells, but also allows in finding solutions to the problem of effective hydrogen storage [1]. It is possible that in the future the fullerit-metal-hydrogen system can boldly compete with modern advanced structures for storage of hydrogen – the environmentally clean energy source [2-6].

To date, the synthesis of CNTs as well as the CNM is carried out by different methods: laser action on metal-graphite electrodes; plasma-chemical evaporation of graphite in a gas [7-14] and liquid medium in the presence of catalysts [15-24]; pyrolysis of hydrocarbon structures on catalysts; pyrolysis of benzene in the presence of organometallic compounds (ferrocene and metal phthalocyanides); the dissolution of carbon monoxide on catalysts.

The method of plasma-chemical evaporation of graphite in an inert gas environment is relatively common, productive and quite effective due to the fact that it allows to obtain both soluble [25-26] and insoluble CNM [27-28]. But only the plasma-chemical evaporation of the anode in a gas medium can guarantee the synthesis of fullerene particles. In this case, the method makes it possible to easily change the synthesis modes, use a different gas medium and, most importantly, achieve a high yield of CNM with different structure and morphology.

However, for today, the oxidation of the CNM deposit (products formed on the cathode) obtained by the plasma chemical method in the gaseous medium which allow the identification of new nanofibers of carbon has not been studied enough.

2 Experimental

To obtain platinum-containing nanoproducts, a plasma chemical plant was used to evaporate the electrodes in a gaseous medium (Figure 1). During the synthesis, electrodes made of high-grade graphite of the PGM-7 grade were used. Also, hollow graphite electrodes containing platinum were used which was

evaporated in a plasma at a pressure of 0.02-0.09 MPa in an inert helium medium.

In a vertical reactor the consumable anode electrode remained stationary and the non-consumable cathode electrode moved along the axis of the reactor. Thus, a uniform distribution of soot over the entire surface of the reactor walls was observed, and relatively the same thermodynamic conditions were obtained for the condensation of the synthesis products.

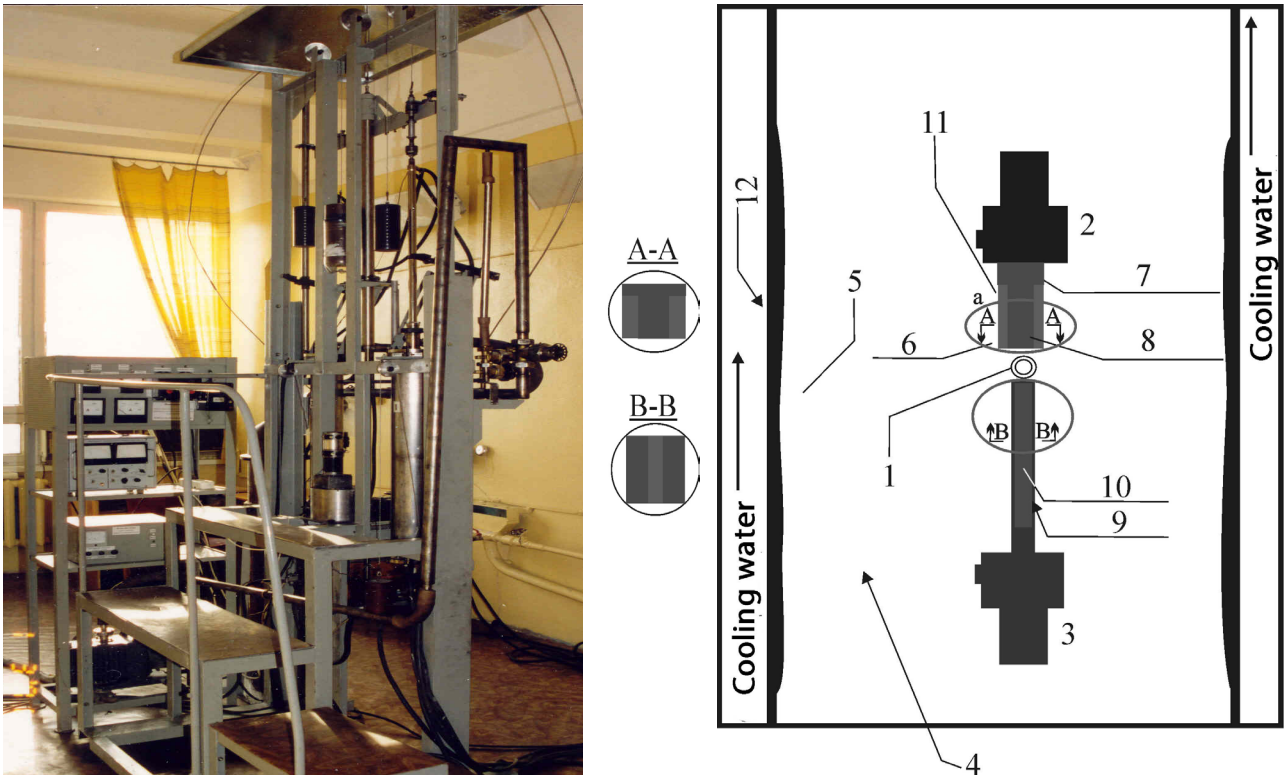

Figure 1 – General view of the set up, diagram of a cylindrical reactor for plasma-chemical synthesis of nanostructures in a gaseous medium: 1 – plasma; 2 – cathode; 3-anode; 4 – helium-containing medium; 5 – platinum-containing carbon black; 6 – deposit; 7 – non-consumable electrode; 8 – the core of the deposit containing MNT; 9 – consumable electrode; 10 – wire catalyst fixed with graphite dust; 11 – the external layer of the deposit; 12 – reactor wall.

A hollow graphite anode containing platinum in the form of a wire was used to introduce the platinum catalyst into the plasma-chemical synthesis zone, the catalyst in the anode cavity was fixed with graphite dust. The cavity of the anode electrode is located along the axis of the atomized part of the anode (Figure 2).

In a number of plasma-chemical syntheses, the anode was evaporated from pure graphite, and also the anode doped with a platinum catalyst (Table 1). The time of plasma-chemical synthesis in the presence of a platinum catalyst lasted more by 40 minutes, considering that the length of the anode doped with platinum (18 cm) was less than the length of a pure graphite anode (21.1 cm). In addition, the evaporation of the platinum platinum-containing electrode was accompanied by fluctuations in the current (175-225 A) and 35-37 V, while the evaporation of the graphite anode was relatively quiet (current strength 185-200 A, voltage 30-33 V). This effect can be explained by the higher evaporation temperature of the platinum-containing anode.

At the end of the evaporation of the platinum-containing anode, the mass of the synthesis product (*Deposit and Wall soot*) exceeds the mass of the product multiple times when the graphite anode evaporates, both along the wall soot and along the mass of the deposit. The large mass of *Wall soot* suggests that in the process of plasma-chemical synthesis, most of the platinum atoms in the process of synthesis of CNM move to the zone of lower pressures and temperatures, namely toward the periphery of the synthesis zone until they cool down on the reactor wall.

Figure 2 – Anode which contains platinum and carbon dust.

Figure 3 – Appearance of the platinum-containing deposit on the cathode.

3 Results and Discussion

The length (5 cm) and therefore the mass (44.990 g) of the platinum deposit significantly exceeds the parameters of the deposit obtained by evaporation of the graphite electrode (length 2.1 cm, weight 7.5 g) (Table 1). This suggests that the atoms of platinum reorganize carbon atoms in the process of plasma-chemical synthesis which makes it possible to accelerate the formation of ONS having resistance to plasma precursor temperatures, and also having sufficient electrical conductivity to form an electric arc.

Table 1 – Conditions and results of plasma-chemical synthesis

		Graphite (C)	**C-Pt**
Conditions	The anode contains	Only graphite	Graphite and Pt
	Length of cathode	8.4 cm	8.4 cm
	Length of anode	21.1 cm	18 cm
	Catalyst (length * width)	-	11*0.1 cm
	Current strength	185-200 A	175-225 A
	Voltage	30-33 V	35-37 V
	Vacuum gauge	0.190-0.174 atm	0.70-0.13-0.33 atm
	Temperature of cooled reactor jacket	31°C	25°C
	The synthesis medium	Helium	Helium
Results	Soot	10.400 g	24.690 g
	Deposit	7.500 g	44.990 g
	Chips	4.700 g	8.495 g
	Anode Remainder	6.6 cm	1.8 cm
	Length of deposit	2.1 cm	5 cm
	Synthesis time	120 minutes	160 minutes

Deposit

In the course of synthesis, when a platinum-containing anode was evaporated on a non-consumable electrode (cathode), a build-up called a deposit was formed during the synthesis (Figure 3). The deposit consists of two parts: a loose core formed by multiwalled nanotubes (MNTs) having a minimum number of structural defects (Figure 4), and a strong crust formed by layered graphite-like structures containing in their volume a smaller amount of MNT.

The shell (crust) of the deposit formed, as in the case of syntheses in the presence of other catalysts, consisted of layered structures located perpendicular to the deposit axis (Fig. 5), densely packed in a single structure.

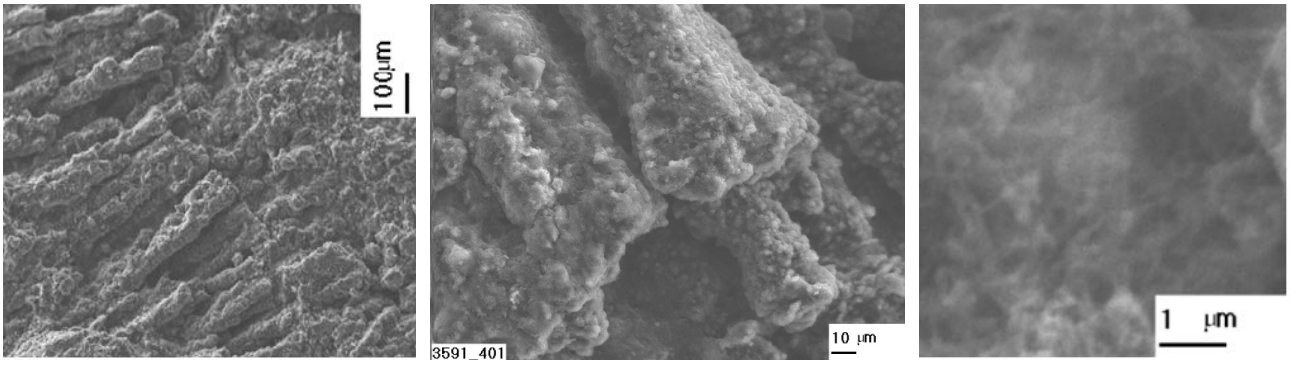

(a) (b) (c)

Figure 4 – Loose-core deposit core: (a) – general view of core conglomerates; (b) – a conglomerate consisting of bundles of NT; (c) – bundles of nanotubes constituting conglomerates.

The core is porous and loose (Figure 4 (a)), a deposit consisting of conglomerates (Figure 4 (b)) oriented along the deposit axis and formed of carbon-like carbon nanotubes (Fig. 4 (c)). The bundle-like structures are joined by multiwalled carbon nanotubes in diameter from 4 to 25 nm (Figure 6).

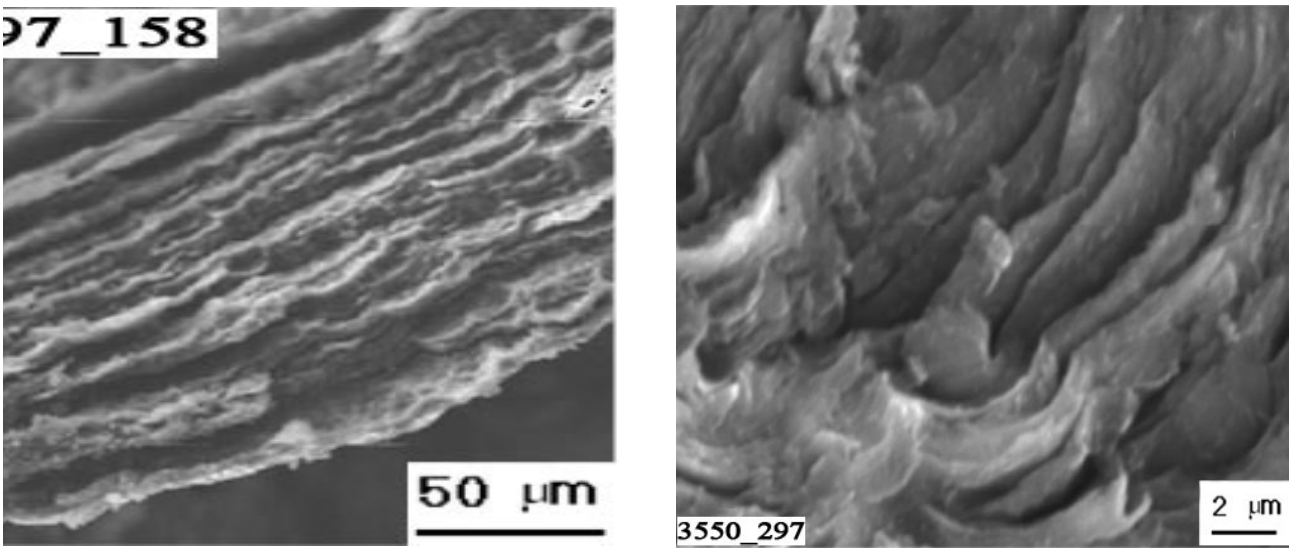

Figure 5 – Dense crust of deposit, formed by layered graphite-like structures.

Figure 6 – Carbon nanotubes constituting the core of the deposit, obtained by the simultaneous evaporation of a graphite electrode doped with platinum.

Upon evaporation of a graphite electrode doped with platinum, a core is formed which has a much denser structure than that obtained by a non-catalytic method. Forming columnar structures are oriented parallel to the deposit axis and have a diameter of 100 – 150 μm (Figure 7 (a), (b), (c)). They are also formed from beam-like carbon nanotubes (CNTs) (Figure 6), in diameter 4-25 nm.

In the plasma-chemical synthesis of platinum-containing carbon nanostructures, not only hollow carbon nanotubes (CNTs) are formed, but also tubes having various structural anomalies. Nanotubes have a rougher outer surface and some inclusions. As shown by the X-ray microanalysis in the core, the content of platinum turned out to be negligible, reaching hundredths of a percent. X-ray diffraction analysis also recorded hexagonal graphite with an admixture of the rhombohedral phase in all parts of the deposit (core and shell).

However, studies of the platinum-containing deposit showed that, unlike similar plasma-chemical syntheses in the gaseous medium, the core of the platinum-containing deposit is well separated from the deposit shell (bark) mechanically and can exist as a single rod.

Thus, a platinum catalyst in plasma-chemical synthesis in a gaseous medium allows the creation of centimeter rods made of beam-like carbon nanotubes (CNTs) that withstand super high temperatures (12000 K) [29].

The possibility of separating the deposit core, consisting of bundles of CNTs, from the deposit crust allows us to consider depositary parts (core and core) as independent products of plasma-chemical synthesis. Moreover, the possibility of separating deposited CNTs from graphite-like bark increases the purity of deposit CNTs and consequently reduces their cost price. Since earlier deposits were crushed to separate the ONS from graphite-like structures. A platinum-containing graphite -like bark (shell) can be used to produce graphite already enriched with platinum.

Platinum-containing CNTs and graphite-like structures, as the final product of processing a platinum-containing deposit, can be key elements of fuel cells which is relevant to this day. Platinum-containing CNTs and graphite-like structures, as the final product of processing a platinum-containing deposit, can be key elements of fuel cells which is relevant to this day.

Thus, it should be noted that during the evaporation of a graphite electrode doped with platinum in an electric arc in an inert helium medium, the bulk of the metal participates in all plasma-chemical reactions and is redistributed among different products.

Most of it moves in the flow of condensate to the walls of the reactor. According to the emission spectral analysis, the largest amount of platinum is in the wall soot (more than 1 % by mass). A small fraction of platinum is less than 1 wt.% In the cationic state, under the influence of a strong electric field, together with the carbon vapor moves to the cathode, forming a platinum-containing deposit. Despite the high temperature in the deposit formation zone which exceeds the boiling point of platinum (3800°C), platinum was present in the deposit.

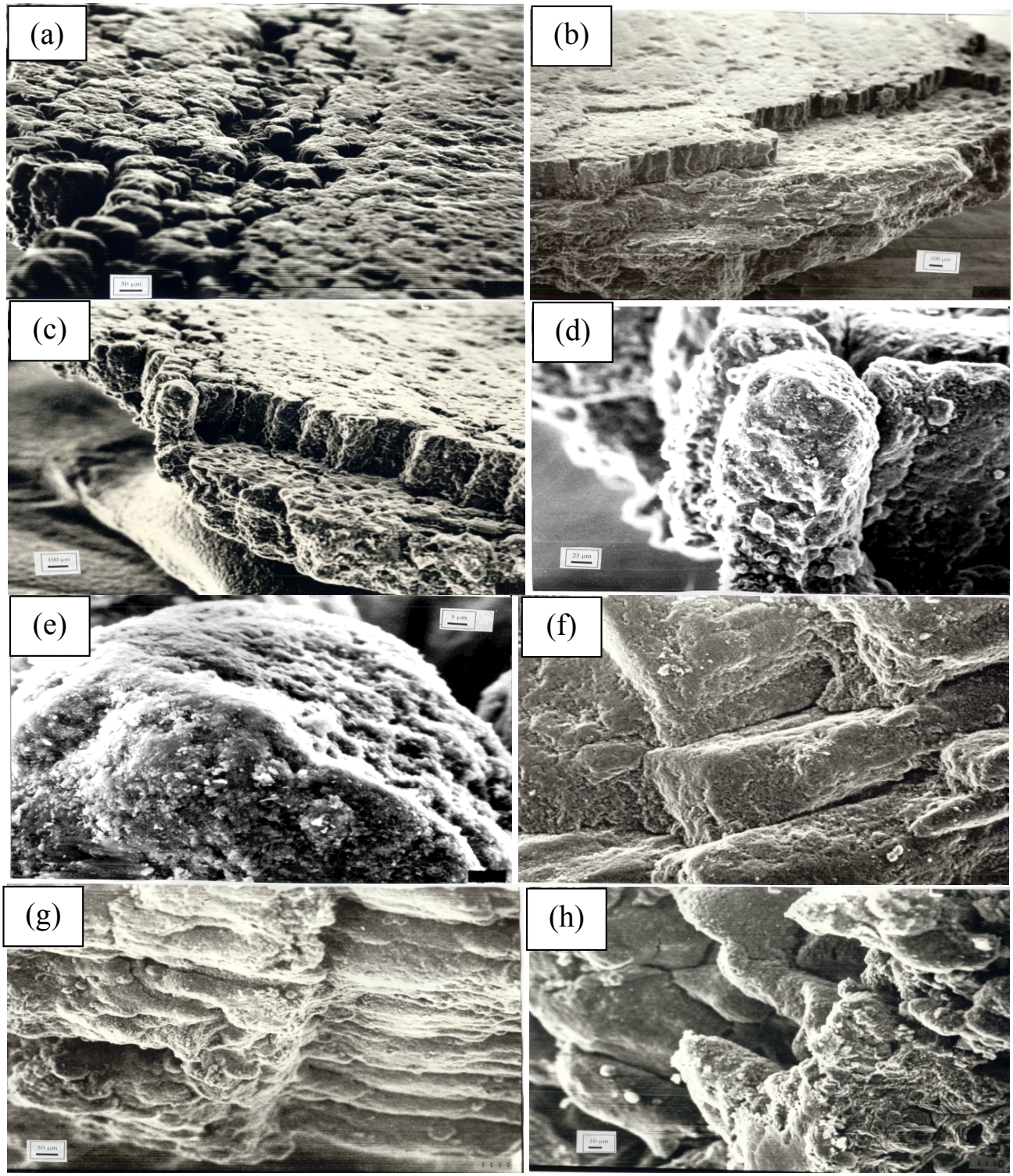

Figure 7 – Morphology of the core of a platinum-containing deposit (SEM) formed by the simultaneous evaporation of a graphite electrode doped with platinum: (a), (b), (c), (d) – core blocks; (e) – block morphology; (g) – is the boundary between the shell and the core; (f), (h) – are the structures of the boundary layer.

As a result of studying the chemical composition of the parts of the platinum-containing deposit, it was determined that the Pt atoms in the deposit are distributed unevenly. Most of the deposit Pt is less than 1 % concentrated in the bark of the deposit itself. We believe that in the case of an electric arc, the flow of electrons passing through the forming deposit that heats it not only affects the formation of the structure of the carbon part of the deposit, but also exerts various processes for the separation of platinum atoms. It settles only in the low-temperature part which is the crust of the deposit.

The presence of platinum explains the higher thermal stability of the platinum deposit crust. Differential-thermal analysis (DTA), thermogravimetric (TG) and differential thermogravimetric (DTG) analyzes confirm these findings. Thus, the temperature at which the platinum-containing bark begins to interact with oxygen in the air (680°C) (Table 2, item 2) exceeds the temperature of interaction with the pure carbon bark (T. = 575°C) (Table 2, item 1) (Figure 8 (a), (b)).

The DTA curve (Figure 8 (b)) marks the biphasic nature of the deposit crust containing platinum. Apparently, in addition to the graphite-like component, this sample contained multi-walled nanotubes, the growth of which initiated the presence of platinum in the cortex.

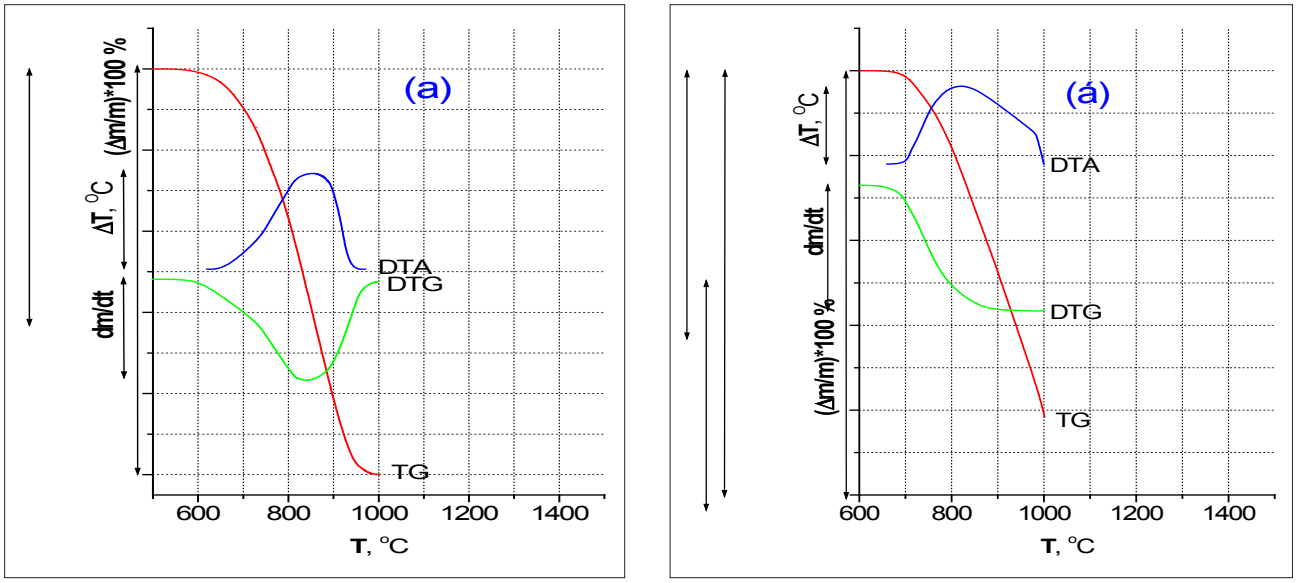

a) b)

Figure 8 – Investigation of the thermal stability of the shell of deposits of plasma-chemical synthesis in a gaseous medium: (a) – the crust of the deposit, obtained during the uncatalyzed synthesis; (b) – the bark of the deposit containing Pt.

Table 2 – Thermal stability of parts of platinum-containing deposits of plasma-chemical synthesis in a gaseous medium.

№	Material	Interaction interval, °C	DTG	DTA	
			T_{1max}, °C	T_{1max}, °C	T_{2max}, °C
1	Shell without catalyst	575-980	840	840	
2	Shell with catalyst (Pt)	680->1000	865	825	990
3	Core with catalyst (Pt)	690-965	865	800	910
4	Core without catalyst	575-990	870	850	960

The core of the deposit formed from carbon-like carbon nanotubes where a scanty platinum content is found also shows a higher thermal stability than the core of the deposit obtained from uncatalculated plasma-chemical synthesis in a gas medium (575°C). The beginning of the reaction with oxygen of air is 690°C.

Thermal analysis showed that in the core of the deposit synthesized in the presence of a platinum catalyst, there are two phases that react with air oxygen at 800°C and 910°C (Table 2).

Wall-mounted soot

A mixture of condensate formed on the walls of the reactor and in the gas phase forms a walled carbon black. It contains both a fullerene-like and an insoluble fraction in liquid hydrocarbons.

At the micro level, the layer of walled soot has the structure shown in Figure 9. The layer of wall soot was previously subjected to sonication in alcohol. The nanostructures that make up it have different geometric shapes and structures (Figure 10).

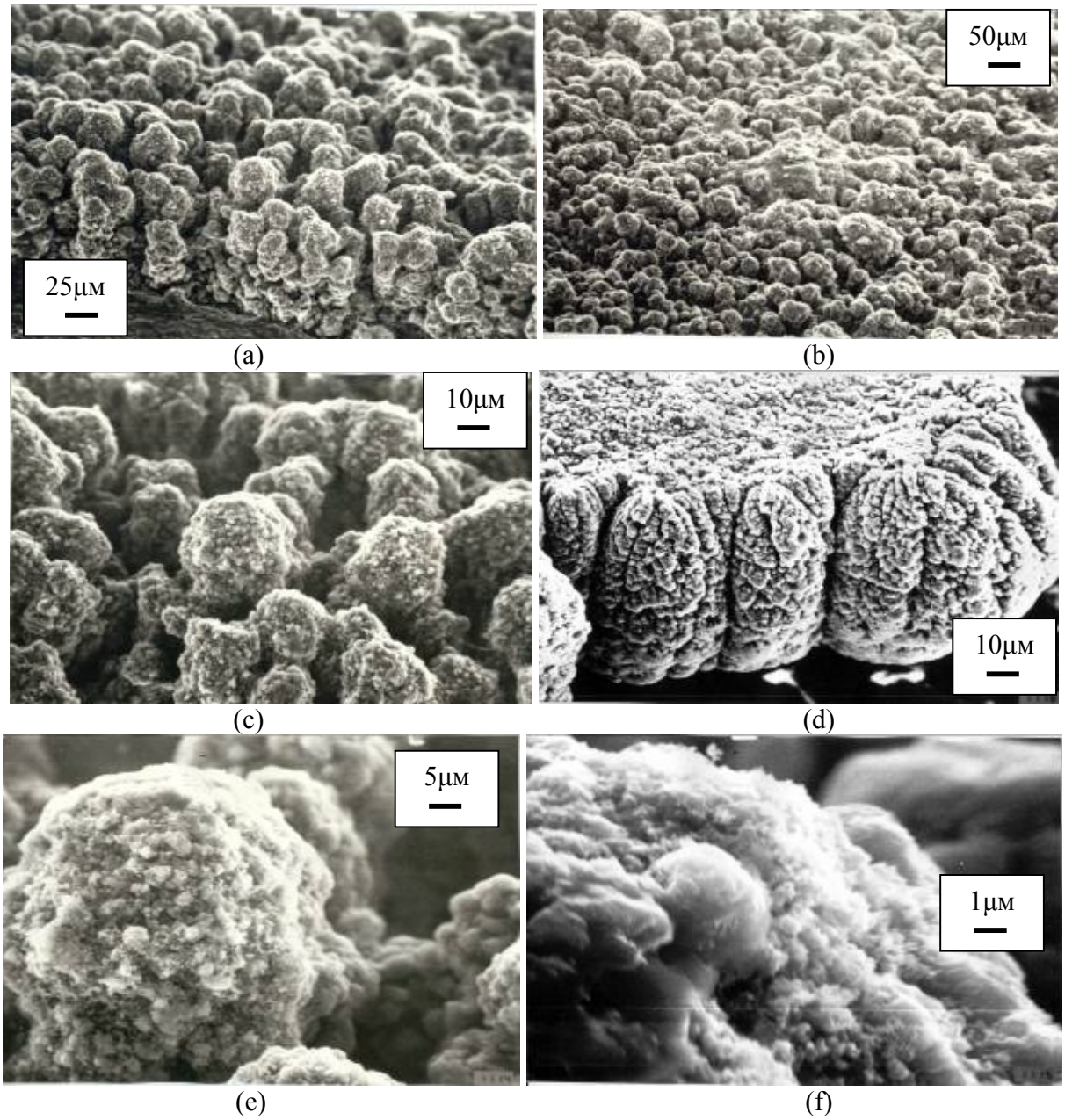

Figure 9 – Wall-mounted soot. Surface morphology after ultrasound treatment in ethanol: ((a), (b), (c), (d), (e), (f) – SEM photo with varying degrees of magnification).

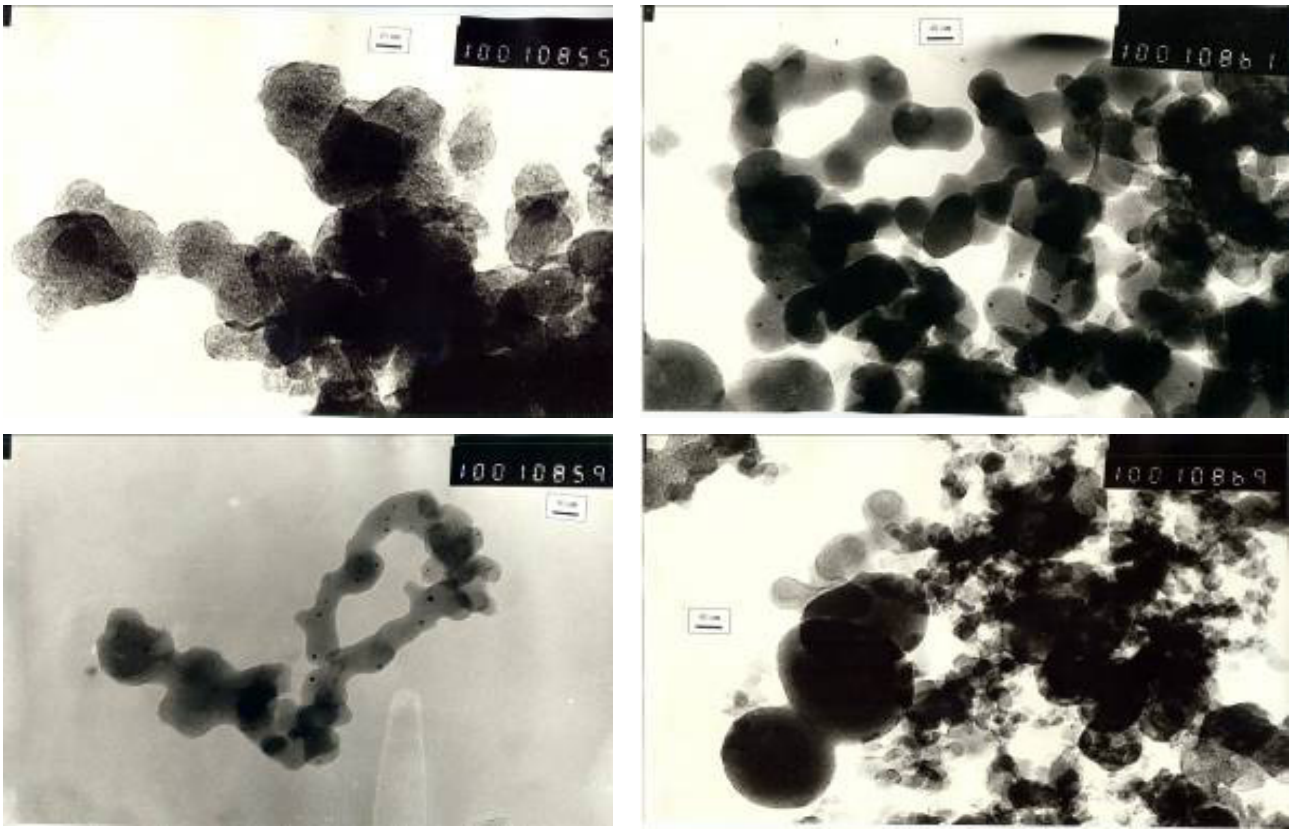

Figure 10 – Photographs of nanoscale particles composing platinum-containing wall soot (TEM).

4 Conclusions

When analyzing the chemical composition of the platinum-containing deposit, it turned out that the Pt atoms in the deposit structure are distributed unevenly. The central part of the deposit (the core) contains trace amounts of platinum that is confirmed by the results of emission spectral analysis and by the X-ray microanalyzer of the core shear surface. The bulk of the platinum in the deposit focuses on the deposit shell. We believe that a large flow of electrons passing through the emerging deposit and plasma temperatures have a significant effect on the formation of the deposit structure as well as the separating effect on the atoms, molecules and particles that make up the synthesis zone.

It is proved that the atoms of the platinum catalyst influence the process of formation of the deposit. Namely, it stimulates the formation of a deposit where the deposit core containing platinum-containing bundles of CNT exists as an independent core that does not have a strong connection with the deposit crust. The possibility of separating the deposit core consisting of bundles of CNTs from the deposit crust allows one to consider depository parts (core and shell) to be independent products of plasma-chemical synthesis.

It is established that differential-thermal analysis of CNM in air by the methods of TG, DTG, DTA allows to reveal insignificant differences in the heat resistance of different carbon nanostructures, and therefore, it can be used for their identification.

References

1. D.V. Shchur, Z.A. Matysina, S.Yu. Zaginaychenko. Carbon nanomaterials and phase transformations in them: Monograph. – Dnipropetrovsk: Science and Education, 2007. P – 680 (in Russian).

2. D.V. Schur, A.A. Lyashenko, V.M. Adejev, V.B. Voitovich, S. Yu. Zaginaichenko. .Niobium as a construction material for a hydrogen energy system. // International journal of hydrogen energy. -1995. –Vol. 20 (5). – Pp.405-407.

3. Z.A. Matysina, S.Y. Zaginaichenko, D.V. Schur. Hydrogen solubility in alloys under pressure // Int. J. Hydrogen Energy. -1996,. -Vol. 21. – No. 11/12. -Pp. 1085-1089.

4. Y.M. Lytvynenko, D.V. Schur. Utilization the concentrated solar energy for process of deformation of sheet metal / // Renewable energy. – 1999. –Vol.16 (1-4). – Pp. 753-756.

5. An. D. Zolotarenko, Z.A. Matysina, S. Yu. Zaginaichenko, D.V. Schur, A. Veziroglu, T.N. Veziroglu, M.T. Gabdullin, N.F. Javadov, Al. D. Zolotarenko. Hydrogen in Crystals. Monograph.- Kiev Publishing house "KIM", Kiev, – 2017. 1061 p. (in Russian).

6. Z.A. Matysina, S. Y. Zaginaychenko, D. V. Schur, An. D. Zolotarenko, Al. D. Zolotarenko, M. T. Gabdullin. Bilary and Potassium Alanates are promising Hydrogen accumulators. // International scientific Alternative Energy and Ecology magazine (ISJAEE). -2017. -No. 13-15. –Pp. 37-60.

7. S. Iijima. Helical microtubules of graphitic carbon //Nature. – 1991. –Vol. 354. – Pp. 56-58.

8. N. Sano, H. Wang, M. Chhowalla, I. Alexandrou, G. A. J. Amaratunga. Synthesis of carbon'onions' in water // Nature. - 2001. – Vol. 414. – P. 506.

9. Lange H. / Lange H., Sioda M., Huczko A., Zhu Y.Q., Kroto H.W., Walton D.R.M. Fullerenes and nanotubes: materials for the new chemical frontier // Carbon. – 2003. – Vol. 41. – P. 1617.

10. E. Tatarova, N. Bundaleska, J. Ph. Sarrette, C. M. Ferreira. Plasmas for environmental issues: from hydrogen production to 2D materials assembly // Plasma Sources Science and Technology. – 2014, – Vol. 23. – P. 063002.

11. An.D. Zolotarenko, Zolotarenko Al.D,, Zolotarenko A.D, Voichuk G.A., Schur D.V., Zaginaychenko S.Yu. Synthesis of endofullerenes by an arc method deposit // Nanosystem, nanomaterials, nanotechnology. – 2005. – Vol. 3. – No. 4. – P. 1133-1144. (in Russian)

12. Al.D. Zolotarenko, An.D. Zolotarenko, V.A. Lavrenko, S.Yu. Zaginaichenko, N.A. Shvachko, O.V. Milto, V.B. Molodkin, A.E. Perekos, V.M. Nadutov, Yu. A. Tarasenko. Encapsulated ferromagnetic nanoparticles in carbon shells. Carbon Nanomaterials in Clean Energy Hydrogen Systems // NATO Science Series. The Netherlands. – 2011. - P. 127-135.

13. E.I. Golovko, A.D. Zolotarenko, A.D. Zolotarenko, G.A. Vojchuk, A.D. Zolotarenko, V.M. Adeev, A.V. Kotko, A.J. Koval', S.A. Firstov, D.V. Schur, O.V. Mil'to, S.J. Zaginaychenko. Synthesis of platinum-containing Carbon Nanostructures // Proc. of 9th International Conference "Hydrogen Materials Science and Chemistry of Carbon Nanomaterials", Sevastopol, Crimea, Ukraine, September. 5-11. -2005. –Pp.1014-1016.

14. Yu.M. Shulga, D.V. Schur, S.A. Baskakov, A.P. Simanovskiy, A.A. Rogozinskaya, A.A. Rogozinskiy, A.P. Mukhachev. XRD Patterns of cathode deposits formed in electric arc sputtering Zr-Me-graphite electrodes // Proc. of NATO ARW "Hydrogen Materials Science and Chemistry of Carbon Nanomaterials. – Boston: Kluwer Academic Publishers. -2004. – Vol. 172. – Pp.137-142.

15. A. Huczko. Synthesis of aligned carbon nanotubes // Appl. Phys. A. – 2002. – Vol. 74. –P. 617–638.

16. A.D. Zolotarenko, A.D. Zolotarenko, A.D. Zolotarenko, G.A. Voichuk, A.D. Zolotarenko, V.M. Adeev, A.B. Korotko, A.Y. Koval, C.A. Firstov, D.V. Shchur, O.M. Milto, S.I. Zaginaychenko, E.I. Golovko. Synthesis of endofullerenes by the arc method deposit // The journal "Nanosestemi, nanomaterials, nanotechnologies. – 2005. ol.3, №4, C. 1133-1144 (in Russian);

17. D.V. Schur, A.G. Dubovoy, A.F. Savenko, S.Yu. Zaginaichenko. Method for synthesis of carbon nanotubes in the liquid phase // Abstracts of International Conference on Carbon "Carbon'04", Providence, Rhode Island, USA, July 11-16. -2004. – P. 187.

18. D. V. Schur, A. G. Dubovoy, S.Yu. Zaginaichenko, V. M. Adejev, A.V. Kotko, V.A. Bogolepov, A.F. Savenko, Al. D. Zolotarenko. Production of carbon nanostructures by arc synthesis in the liquid phase // Carbon. – 2007. – Vol. 45. –N.6. -Pp. 1322-1329.

19. N.S Koprinarov., M.A. Constantinova, G.V. Pchelarov, M.V. Marinov. Fullerene macro structures // Journal of Crystal Growth. – 1997, – Vol. 171, – P. 111.

20. / And. Zolotarenko, A.G. Dubovoy, A.E. Perekos, V.A. Lavrenko, T.V. Efimova, V.P. Zalutsky, T.V. Ruzhitskaya, A.V. Kotko, Al. Zolotarenko. The effect of the magnetic field on the phase-structure state and the magnetic properties of highly dispersed Fe powders obtained by electrospark dispersion // Journal of Nanosystems, Nanomaterials, Nanotechnologies. -2013. – Vol. 11. – No. 1.2. – P. 131-140.

21. Biro L.P., Z.E. Horvath, L. Szalmas, K. Kertesz, F. Weber, G. Juhasz, G. Radnoczi, J. Gyulai. Continuous carbon nanotube production in underwater AC electric arc // Chemical Physics Letters. – 2003. – Vol. 372, – P. 399–402.

22. V.A. Lavrenko, I.A. Podchernyaeva, D.V. Shchur, An.D. Zolotarenko, Al.D. Zolotarenko. Features of physical and chemical adsorption during interaction of polycrystalline and nanocrystalline materials with gases // Springer US «Powder Metallurgy and Metal Ceramics», USA, January. – 2018. -Vol. 56. – Issue 9-10. -Pp. 504-511.

23. Al.D. Zolotarenko, An. D. Zolotarenko, V.A. Lavrenko, S. Yu. Zaginaichenko, N.A. Shvachko, O.V. Milto, V.B. Molodkin, A.E. Perekos, V.M. Nadutov, Yu.A. Tarasenko. Encapsulated ferromagnetic nanoparticles in carbon shells // Springer «Carbon Nanomaterials in Clean Energy Hydrogen Systems», NATO Science Series. The Netherlands – 2011. – P. 127-135.

24. An. D. Zolotarenko. Physicochemical features of the synthesis of carbon nanoparticles in the arc phase in the rare phase // Abstract. dis. Cand. chem. Sciences: spec. 02.00.04 "Physical Chemistry" / // IPM of NAS of Ukraine. – Kiev, 16 herbs 2014. P. – 22 (in Russian).

25. N.S. Anikina, Z.S. Yu, M.I. Maistrenko, A.D. Zolotarenko, G.A. Sivak, D.V. Schur. Spectrophotometric analysis of C60 and C70 fullerences in the toluene solutions // Springer «Hydrogen Materials Science and Chemistry of Carbon Nanomaterials», NATO Science Series II. – 2005. –Vol. 172. – P. 207-216.

26. A.D. Zolotarenko, D.V. Shchur, S.I. Zaginaychenko, N.A. Anikin, O.Y. Krivushchenko, V.V. Skorokhod, And. Zolotarenko, Al. Zolotarenko. Discovery of the "Ordering Effect" of the meta-isomer-product of nitration of monosubstituted benzene and its relation to the reactivity of monosubstituted benzenes in reactions of intermolecular donor-acceptor interaction with fullerene C60. // Book of Abstracts of the XIth Int. "Hydrogen material science and chemistry of carbon nanomaterials", Yalta, Crimea, -2009. – P. 606-609 (in Russian).

27. Y.M. Shulga, S.A. Baskakov, A.D. Zolotarenko, E.N. Kabachkov, V.E. Muradyan, D.N. Voylov, V.A. Smirnov, V.M. Martynenko, D.V. Shchur, A.P. Pomytkin. Staining of graphene oxide nanolides and colored polymer compositions on their basis // Journal of Nanosystems, Nanomaterials, Nanotechnologies. – 2013. – Vol. 11. -No. 1.2. – P. 161-171 (in Russian).

28. A.A. Volodin, A.D. Zolotarenko, A.A. Belmesov, E.B. Gerasimova, D.V. Shchur, B.P. Tarasov, S.I. Zaginaychenko, S.V. Doroshenko, An. D. Zolotarenko, Al. D. Zolotarenko. Electroconductive composite materials based on metal oxides and carbon nanostructures // The journal "Nanosestemi, nanomaterials, nanotechnology". – 2014. –Vol.12. –No. 4. -Pp. 705-714 (in Russian).

29. The Great Soviet Encyclopedia. – Moscow: Soviet Encyclopedia. 1969-1978 (in Russian).

IRSTI 29.27.07

On distribution function of free and bound electrons in equilibrium Coulomb system

S.A. Maiorov[1,2,*] and A.L. Khomkin[1,2]

[1]*Prokhorov General Physical Institute of the Russian Academy of Sciences, 38, Vavilov Str., 119991, Moscow, Russia.*
[2]*Institute for High Temperatures, Russian Academy of Sciences, 13, Izhorskaya Str. Bd.2, 125412, Moscow, Russia,*
e-mail: mayorov_sa@mail.ru

In classical thermodynamics, the velocity distribution function of particles is always Maxwell distribution for any density. This is due to the fact that the dependences on the pulses and coordinates in the expression for the total energy are separated. Integration over coordinates leads to the appearance of a configuration integral, and the remaining part is divided into the product of Maxwell distribution functions. In the case of formation of bound states (molecules) in an atomic gas, the full phase space of the relative motion of two particles is divided into two parts. The first corresponds to negative energies of relative motion (molecular component), and the second to positive (free atoms). The velocity distribution function remains Maxwellian, if we ignore the fact of separation of the phase space. It can be assumed that for free atoms the velocity (kinetic energies) distribution may be different from Maxwell. For plasmas, the assumption of the non-Maxwellian velocity distribution function of free electrons was made. The influence of the non-Maxwell electron distribution function on the recombination coefficient is estimated.

Key words: distribution function, electrons, Coulomb system, recombination coefficient.
PACS numbers: 52.65.−y, 52.40.Mj.

Introduction

The velocity distribution function of particles is always Maxwellian for any density in classical thermodynamics [1]. This is because the dependences on the pulses and coordinates in the expression for the total energy are separated. Integration over coordinates leads to the appearance of a configuration integral, and the remaining part is divided into the product of Maxwell distribution functions. Hill [2] drew attention to the fact that in the case of formation of bound states (molecules) in an atomic gas, the full phase space of the relative motion of two particles is divided into two parts. The first corresponds to negative energies of relative motion (molecular component), and the second to positive (free atoms). The velocity distribution function remains Maxwellian, if we ignore the fact of separation of the phase space. It can be assumed that for free atoms the velocity (kinetic energies) distribution may be different from Maxwell. For atomic plasmas, the assumption of the non-Maxwellian velocity distribution function of free electrons was first made in [3].

Following [3], we illustrate the above with the example of an atomic plasma, where the formation of bound states (atoms) occurs and there are free particles (electrons and ions). Considering the ions as massive particles, we write the Boltzmann distribution function for momenta p and coordinates r, considering the interaction potential to be Coulomb:

$$V(r) = -e^2/r$$

$$F(p,r) = \frac{1}{(2\pi\hbar^2)^3}\int d\mathbf{p}d\mathbf{r}\exp(-\beta(\frac{p^2}{2m} - \frac{e^2}{r})) \quad (1)$$

where $\hbar$ is the Planck constant, β is the inverse temperature, m is the mass, e is electron charge. Let us determine the phase space Ω for free

electrons in a Wigner-Seitz cell of radius a in order not to burden yourself considering the effect of Debye screening.

$$\Omega = \{r < a; \frac{p^2}{2m} - \frac{e^2}{r} > -\frac{e^2}{a}\}$$
$$\frac{4\pi a^3}{3} n_i = 1 \quad (2)$$

We introduce dimensionless values and variables: $\gamma = \beta e^2/a$, $x = \beta p^2/2m$, $y = \beta e^2/r$.

Integrating over the coordinates in (1), for the distribution function of the kinetic energy we obtain:

$$f(x,\gamma) = A(\gamma)\sqrt{x}\exp(-x)H(x,\gamma), \quad (3)$$

where

$$H(x,\gamma) = \int_{\gamma}^{x+\lambda} \frac{\exp(y)}{y^4} dy. \quad (4)$$

In (3) $A(\gamma)$ normalization constant determined from the condition

$$\int_0^{\infty} f(x,\gamma)dx = 1. \quad (5)$$

Maxwell distribution in our variables is

$$f_M(x) = \frac{2}{\sqrt{\pi}}\sqrt{x}\exp(-x). \quad (6)$$

Figure 1 shows the distribution functions calculated by the formulas (3) and (6) for $\gamma = 1$.

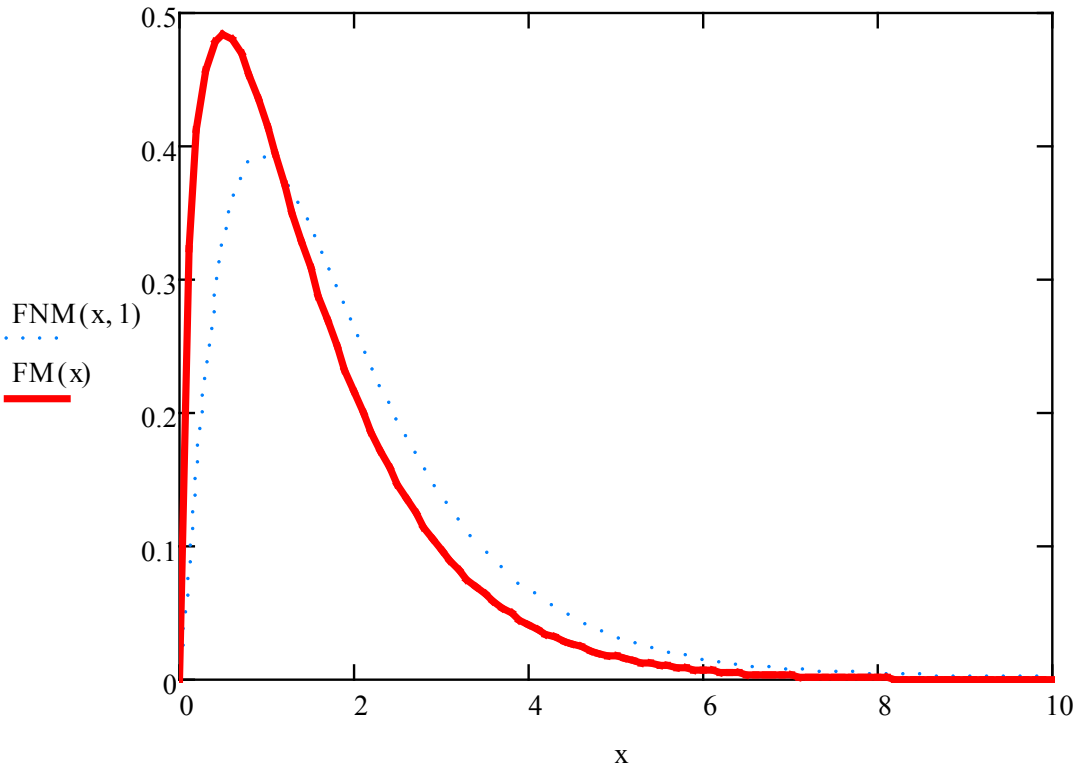

Figure 1 – The distribution function of edekronov on speeds: the solid line – Maxwell (6); dashed – nonmaxwell (3).

It can be seen that the non-Maxwell effect manifests itself quite noticeably, especially at high kinetic energies. When confirming this effect, we can expect a noticeable modification of various kinetic coefficients, in the calculation of which it is necessary to perform velocity averaging.

The papers [4-20] is devoted to the study of the non-Maxwell configuration effect, in which the molecular dynamics method considered the relaxation of the Coulomb system, which allows the formation of bound states, to equilibrium. A similar, but pure quantum effect was considered in (see [5] and references therein), where the non-Maxwell effect was discovered by quantum statistics methods due to quantum broadening. The influence of the deviation from the Maxwell distribution on the speed of various kinetic processes was also considered. In this paper, a direct measurement of the distribution function of free electrons by kinetic energies was performed using the numerical simulation method [6] of a model Coulomb system, provided that about half of the electrons are in bound states. The non-Maxwell effect is shown explicitly.

In the present work based on the application of the molecular dynamics method:

the relaxation of the distribution function of free electrons in the course of transition to an equilibrium state is investigated;

b) equilibrium configurations of particles are calculated and the correlation function of the model Coulomb system is determined;

using statistical averaging, its thermodynamic functions are calculated.

for the first time at the microscopic level, the dynamics of the formation of bound complexes consisting of a different number of initial particles can be traced, which makes it possible to model clustering processes in the system.

Calculation of parameters of the charge-symmetric model system

Consider a model Coulomb system consisting of particles of the same mass. Choose the model potential of interaction between particles in the form:

$$V(r)=\begin{cases} e^2/\sigma\left[(\sigma/r)^{12}-(\sigma/r)\right], \text{ in } +- \text{ interaction,} \\ e^2/r, \text{ in } ++, -- \text{ interaction.} \end{cases} \quad (7)$$

Its asymptotic behavior for opposite charges at small distances r has the character of repulsion, and with $r\to\infty$ it is attractive and coincides with the Coulomb potential 1/r. For intermediate values of r, the potential has a well and allows the formation of classical bound states. The choice of the model potential in the form of (7) is due to the need to eliminate the Coulomb potential feature at $r\to0$, which makes it impossible to integrate the equations of motion of particles. At such a potential, bound states are formed in the system. The thickness of the soft wall σ can always be chosen equal to the diameter of the ion core. In the present work, the choice of potential parameters: σ and ε=e2/σ – the depth of the potential well was carried out in such a way as to realize the required values of the nonideality parameter Γ and the degree of ionization α (σ = 2 Å). The latter was estimated by the classical Saha formula with the potential 12-1 (7).

The temporal evolution of the system was modeled using the multi-particle dynamics method (DMP) [4, 6, 16-20]. The trajectories of N positive and N negatively charged ions were determined by numerical solution of Newton's

$$\ddot{r}_k = F_k/m_k, F_k=\sum_{l\neq k}^{2n} f_{kl}, k=1,2,...,2N, \quad (8)$$

$$f_{kl}=\begin{cases} \dfrac{e^2(r_k-r_l)}{|r_k-r_l|^3} \\ \dfrac{e^2(r_k-r_l)}{|r_k-r_l|^2\sigma}\left[\left(\dfrac{\sigma}{r}\right)^{12}-\left(\dfrac{\sigma}{r}\right)\right], \end{cases} \quad (9)$$

where rk is the radius vector of the particle number k; mk is it's mass (the mass of protons was taken); e is electron charge.

At the initial time t=0 the coordinates and velocities of the particles were set using a random number generator. The coordinates are in accordance with the uniform distribution, and the speed in accordance with the Maxwell distribution for the initial temperature T0. Maxwell distribution was defined as follows:

$$V_x=\sqrt{-2\overline{V^2}\ln\xi_1}*\cos(2\pi\xi_3)$$
$$V_y=\sqrt{-2\overline{V^2}\ln\xi_1}*\sin(2\pi\xi_3)$$
$$V_z=\sqrt{-2\overline{V^2}\ln\xi_2}*\cos(2\pi\xi_4)$$

$$\xi \in (0,1)$$
$$\overline{V}^2 = kT / m \quad (10)$$

The particles were in a cube with thermostatic walls. The length of the cube edge was chosen such as to ensure the desired density of particles. Particles reaching the walls returned to the cube with an equilibrium distribution of kinetic energy corresponding to the wall temperature Tst.

In the calculations, the algorithm [4] was used to reduce computer time. Let at the time t0 be known all coordinates rk(t0) and velocities vk(t0) of particles. The procedure for determining the quantities rk(t0+Δt) and vk(t0+Δt), where Δt – a step in time, is as follows.

a). The coordinate values r0k(t0+Δt/2), corresponding to the rectilinear motion of the particles, are calculated.

b). The values of the forces acting on the particles are calculated:

$$F_k^c(t_0 + \Delta t/2) = \sum_{l \neq k}^{2N} f_{kl}(r_k^0 - r_l^0). \quad (11)$$

c). Each particle is determined by the two nearest neighbors of the particles of each sign and the distance to them.

d). The force acting on a particle is calculated as the sum of two forces

$$F_k = F_k^c + F_k^\tau,$$

where F_k^τ due to the interaction with the nearest neighbors of a given particle, F_k^c – interaction with all other particles.

e). Newton's equations are integrated according to the fourth-order Runge-Kut scheme with a step

$$\tau = \Delta t / N\tau,$$

where Nτ is the number of internal steps.

In the course of integration, only interaction with the nearest particles is considered temporary.

$$F_k(t) = F_k^c(t_0 + \Delta t/2) + \quad (12)$$
$$+ F_k^\tau(t), t_0 < t < t_0 + \Delta t,$$

After determining the values rk(t0+Δt) and vk(t0+Δt) the condition of the particles leaving the cube boundary is checked. Particles that go beyond the cube bound are returned back to the cube with an equilibrium distribution of kinetic energy corresponding to the wall temperature Tst.

The following values were used in the calculations:

$$\Delta t = 0.05\ \tau ei,\ N\tau = 10\ ,$$

where τei is the mean time interparticle distance.

The simulation results and discussion

At the first stage, the relaxation of a system of charges of equal mass to an equilibrium state was studied, which was fixed by the temperature and ionization degree to equilibrium values.

Figure 2 shows the dependence of the number of bound states on time. A system of 400 negative and the same number of positive ions is considered. External parameters: density nk=1020 cm-3 and temperature T=1200 K. The degree of ionization, calculated according to the classical Saha formula, was about 0.5. The exit of the system to ionization equilibrium is clearly visible. The wave-like nature of relaxation can be associated with the reflection of a diffusion flow of bound particles from the bottom of a potential well. Such a relaxation pattern is observed in all the considered modes. The relaxation time increases with decreasing of density. For nk=1019 cm-3 time to equilibrium is about 2500τei.

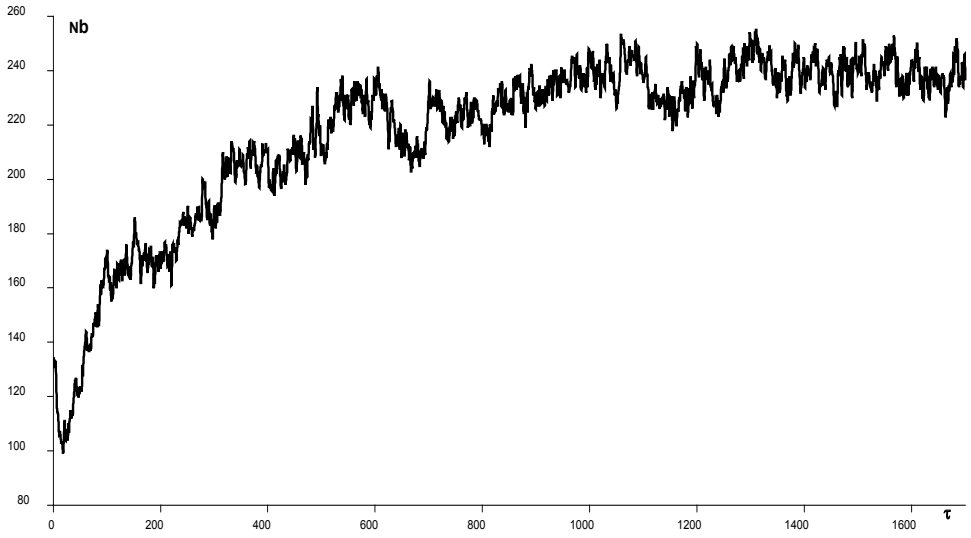

Figure 2 – The dependence of the number of bound states on time (ne=1020 cm-3 and T=1200 K)

Figure 3 shows the particle temperature relaxation (two thirds of the average kinetic energy) for the same mode as in Figure 1. The previous stage can be considered as preparation for the process of measuring equilibrium characteristics. In the equilibrium region, the particle distribution function was measured by kinetic energy and distances to the nearest ion. Averaging was performed over several dozens of equilibrium configurations. Measurements were carried out both for free particles and for particles bound into atoms.

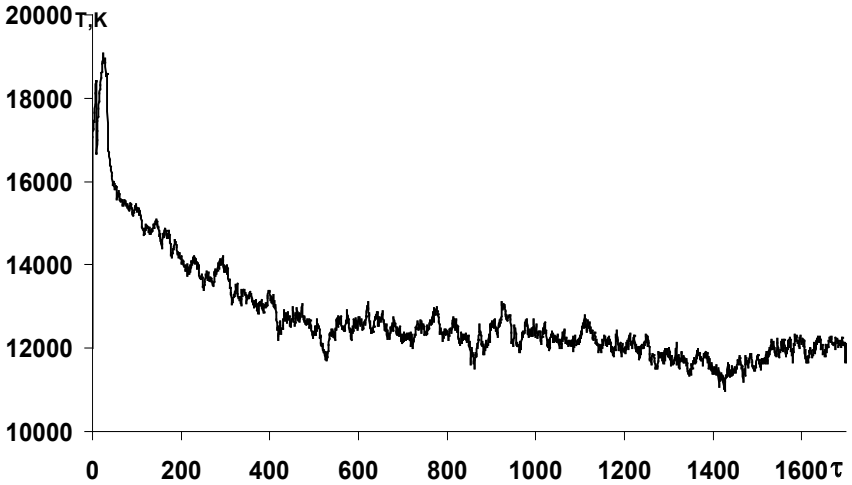

Figure 3 – Particle temperature relaxation (ne=1020 cm-3 and temperature T=1200 K).

Figures 4 a), b), c) show the measured distribution functions of free negatively charged ions by kinetic energies (ε – is the dimensionless kinetic energy related to temperature) for the three regimes in density and temperature.

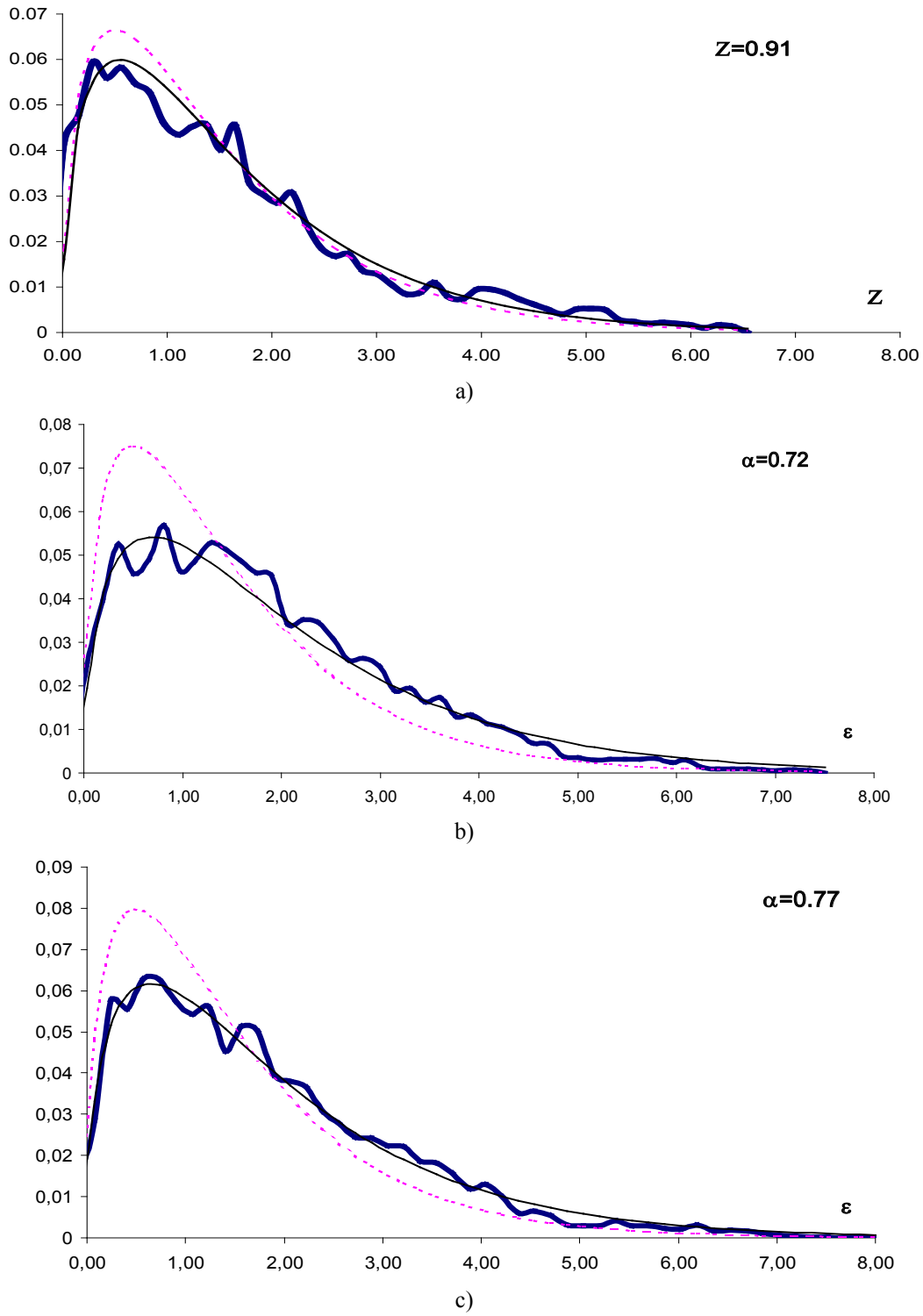

a)

b)

c)

Figure 4 – The distribution function of free negatively charged ions by kinetic energy:
a). ne=1019 cm-3 and T=8000 K, b). ne=1020 cm-3 and T=12000 K, c). ne=1021 cm-3 and T=18000 K.

Solid smooth lines correspond to the function of the form:

$$f(\varepsilon) = \frac{2}{\sqrt{\pi}} \sqrt{\varepsilon} \alpha^{\frac{3}{2}} \exp(-\alpha\varepsilon). \quad (13)$$

with the values of the parameter α, indicated in the figures. The deviation of the equilibrium distribution function of free particles from the Maxwell distribution is quite clearly seen. With increasing nonideality, these deviations increase. At low energies, there is a shortage, and at high energies, an excess of free ions. Qualitatively, this behavior corresponds to the results of [3]. It is noticed that in the system with the formation of bound states there appear molecules consisting of more than two particles. The following connectivity criterion was chosen: a pair of particles is connected if the total energy of their relative motion is less than the interaction energy at an average distance. All bonds in the system were considered and the molecular composition was analyzed. After that, averaging was performed over several dozens of equilibrium configurations.

Figure 5 shows how many molecules of each type are represented in the system; Nат is the number of particles in a molecule. It can be seen from the figure that as the density increases, the specific gravity of the pairs decreases, and more and more heavy molecules appear. Numerical calculation shows that the lifetime of molecules consisting of more than four particles does not exceed 20 characteristic times, whereas the average lifetime of pairs is about 100 characteristic times.

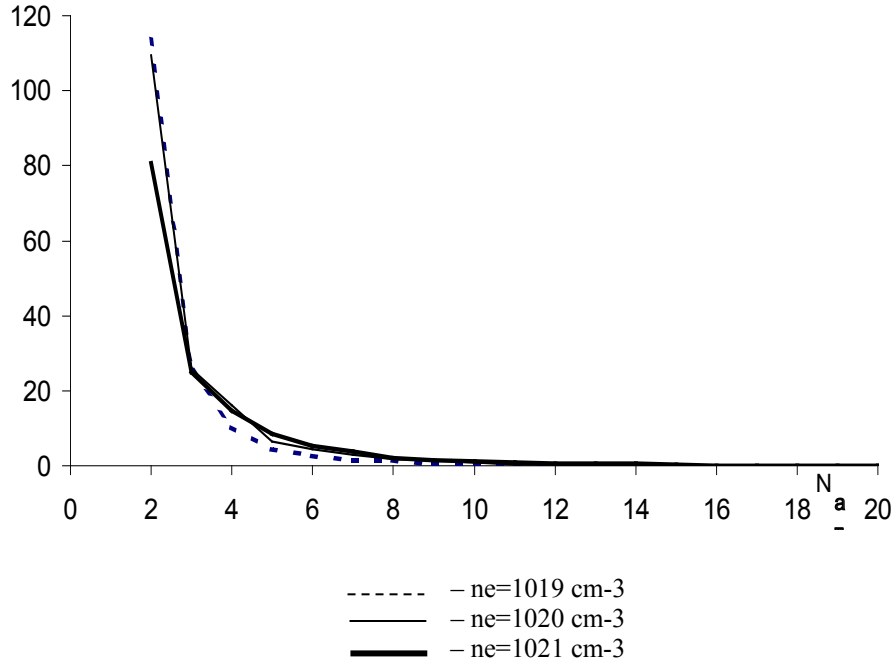

Figure 5 – The average number of polyatomic complexes in the system

Figure 6 shows the charge distribution of molecules. It can be seen that the highest number is represented by singly charged molecules.

We also measured the average energy of the interaction of a free electron with the system. It was taken into account that some heavy molecules were charge carriers, which had an additional effect on the motion of free particles. The obtained data are presented in Figure 7. Solid thick line – the energy of the interaction of particles at a medium distance, the dashed line and the double dashed line are the Debye theory in the large and small canonical ensemble, respectively, the data of molecular dynamics calculations are shown by dots. It can be seen that the measured average interaction energy of a free electron with the entire system turns out to be close to the interaction energy of particles at an average distance, but slightly exceeds the latter.

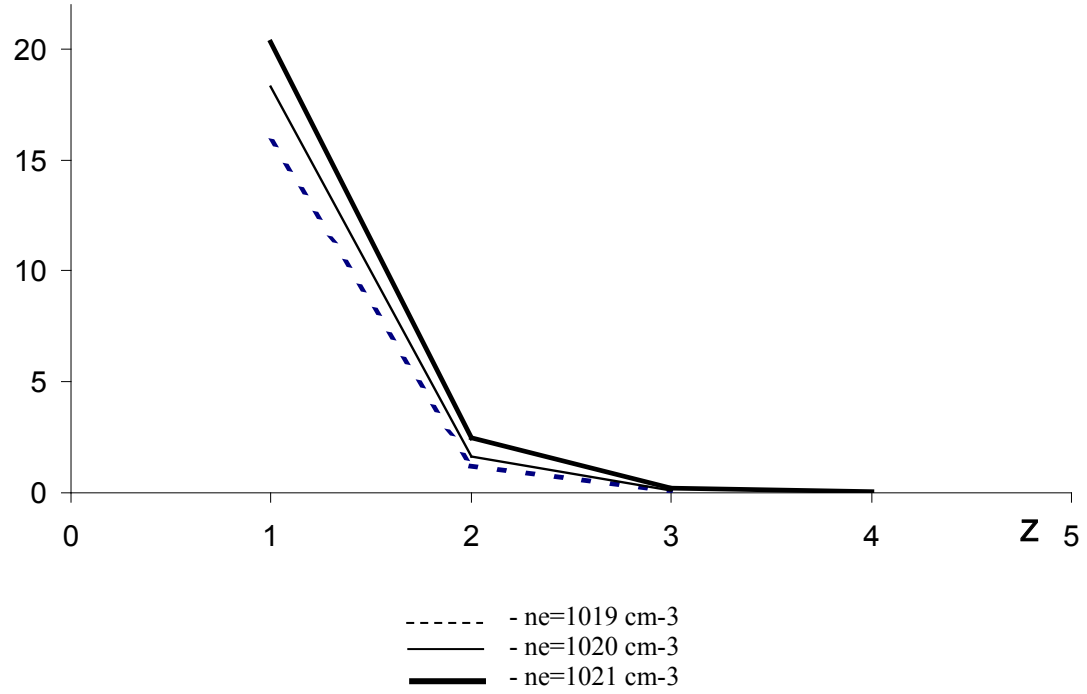

Figure 6 – The distribution of polyatomic complexes on charges

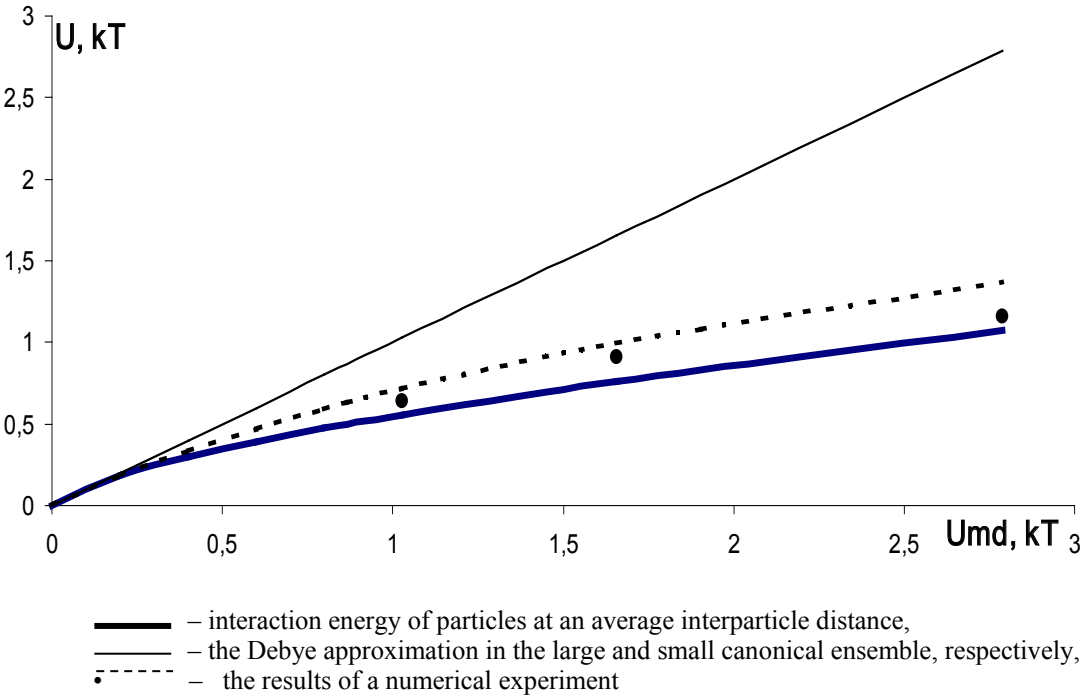

Figure 7 – The average energy of the interaction of a free electron with free particles

The relaxation of model Coulomb systems is studied by the molecular dynamics method in papers [7–9] and the recombination coefficient in a nonideal plasma is calculated. The flux in the energy space is calculated in [7], and in [8] the increase of the number of bound states is analyzed, which are determined by the number of revolutions of the electron around the ion. In the present work, we evaluated the role of non-Maxwell in the recombination coefficient. In accordance with Thomson's theory, the recombination frequency is proportional to the velocity of the incident electron, the scattering cross section, and the cube of the Landau length, which leads to the dependence $T^{-9/2}$.

The correction factor was calculated by the formula

$$K(\gamma) = \frac{\left\langle \left(\frac{p^2}{2m} \right)^{9/2} \right\rangle_{Max}}{\left\langle \left(\frac{p^2}{2m} \right)^{9/2} \right\rangle_{Non\ Max}} \qquad (14)$$

where in the numerator averaging was performed with the Maxwell distribution function (6), and in the denominator with (3).

Using the expression for the Thomson recombination coefficient α

$$\alpha = 2.07 \frac{e^{10}}{\sqrt{m}\, T^{9/2}} \qquad (15)$$

we get $\alpha_{NM} = \alpha K(\gamma)$. Figure 8 presents theoretical dependencies α and α_{NM} from γ in coordinates $\alpha n_e / \omega_p, \gamma$, as well as numerical simulation data [7,8] and [9].

4 Conclusions

This paper investigates the relaxation of a charge-symmetric system of Coulomb particles to an equilibrium state. It is shown that in the system with the selected interaction potential (7) bound states arise. The temperature relaxation process coincides in time with the establishment of ionization equilibrium between bound and free states. A direct “measurement” of the distribution function of free particles by the kinetic energy in the equilibrium state was carried out. Its deviation from Maxwellian, due to a decrease in the configurational space of free particles, was recorded. The free charge subsystem turned out to be “hotter” than all the charges in general. The kinetic energy distribution of the entire set of charges (bound and free) remains Maxwellian.

The influence of the non-Maxwell of the electron distribution function on the recombination coefficient is estimated.

The relaxation of the radial distribution function of all particles is investigated in the approximation of the nearest neighbor. At equilibrium, the radial distribution function measured in this way coincides with the theoretical one within the error of averaging.

The measured average interaction energy of a free electron with the entire system is close to the interaction energy of particles at an average distance, which indicates the saturation of the Coulomb nonideality in the system of free charges. In the subsystem of bound particles with increasing density, along with paired particles, polyatomic complexes are also formed, i.e. there is a clustering process.

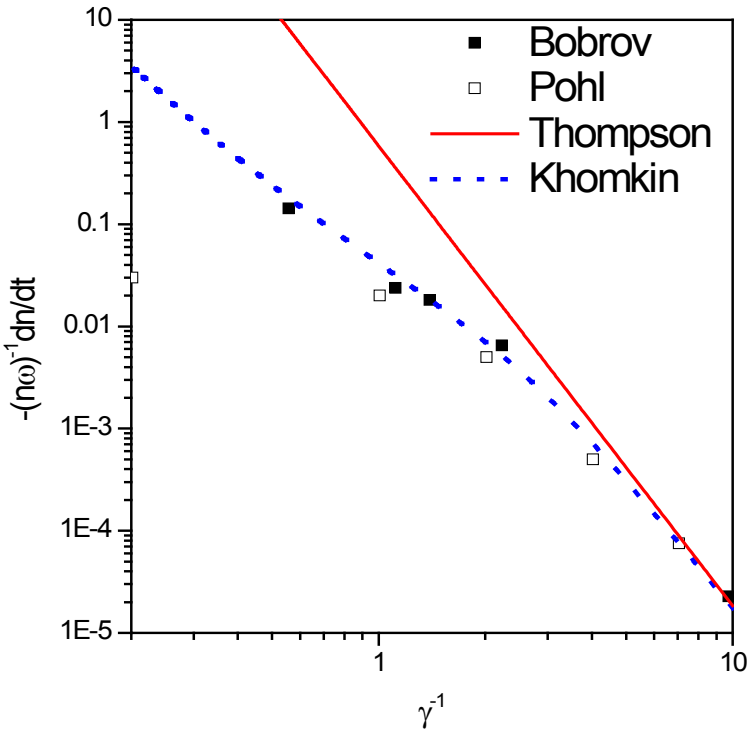

Figure 8 – Theoretical dependencies α and α_{NM} from γ in coordinates $\alpha n_e / \omega_p$, γ

Thus, the main effect of nonideality in the system with increasing density is associated with the formation of composite complexes, while the interaction energy of free charges grows slightly.

References

1. L.D. Landau, E.M. Lifshitz. Course of Theoretical Physics. Volume 5: Statistical Physics, Part 1, Oxford: Butterworth–Heinemann, 1975, 584 p.

2. T. Hill. Statistical mechanics. Principles and selected applications. New York a. o., McHaw-Hill, 1956, 520 p.

3. T.P. Wright, O. H. Theimer. Non-Maxwellian equilibrium distribution for free electrons in a plasma // Phys. Fluids. -1970. – Vol.13. – No.4. –Pp. 895-901.

4. S. Novikov, A.L. Khomkin. Investigation of relaxation and equilibrium properties of a non-ideal Coulomb system using the molecular dynamics method // Proceedings of the Conference FNTP-98, Petrozavodsk, 1998, part 1. -1998. -Vol. 2. -Pp.476-479.

5. A.V. Eletsky, A.N. Starostin, M.D. Taran. Quantum corrections to the equilibrium rate constants of inelastic processes // Phys.—Usp. – 2004. -Vol. 175. –No.3. –Pp. 299-313.

6. S.A. Maiorov, A.N. Tkachev, S.I. Yakovlenko. Studies of the fundamental properties of Coulomb plasma by the method of the dynamics of many particles // Sov. Phys. J. -1991. -Vol. 34. -No.11. –P. 951.

7. A.A. Bobrov, S.Ya. Bronin, B.B. Zelener, B.V. Zelener, E.A. Manykin, D.R. Khikhlukha. Collision recombination coefficient in ultracold plasma. Molecular dynamics calculation // JETP. – 2011. – Vol. 139. -Pp. 605.

8. A. V. Lankin, G. E. Norman. Collisional recombination in strongly coupled plasma // J. Phys. A. – 2009. -Vol. 42. -P. 214032.

9. G. Bannasch, T. Pohl. Rydberg atom formation in strongly correlated ultracold plasmas // Phys. Rev.A. – 2011. -Vol. 84. – P. 052710.

10. D.N. Zubarev. Nonequilibrium statistical thermodynamics, Berlin: Springer Verlag, 1974, 416 p.

11. P. Landsberg. Problems in thermodynamics and statistical physics, Ed., London: Pion, 1989, 640 p.

12. A. Isihara. Statistical Physics, New York: Academic, 1971, 472 p.

13. Yu.L. Klimontovich. Statistical Physics, Boca Raton, Florida, United States: CRC Press, 1986, 608 p.

14. Ya.P. Terletskii. Statistical Physics, Amsterdam, The Netherlands: North Holland, 1971, 280 p.

15. J. Mayer, M. Goeppert-Mayer. Statistical Mechanics, New York: Wiley, 1977, 544 p.

16. S.A. Maiorov, A.N. Tkachev, S.I. Yakovlenko. Unexpected properties of classical Coulomb plasma, discovered on the basis of first principles modeling // Mat. Model. – 1992. -Vol. 4. – No.7. – P. 3. (in Russian)

17. S.A. Maiorov, A.N. Tkachev, S.I. Yakovlenko. Recombination on of a Coulomb plasma and nonbinary interaction effects // Russ. Phys. J. – 1993. -Vol.36., No.1. – P. 55.

18. S.A. Maiorov, S.I. Yakovlenko. S.I. Development of a method for modeling the dynamics of many coulomb particles // Russ. Phys. J. – 1994. – Vol. 37., No. 11. – P.1048.

19. S.A. Maiorov, A.N. Tkachev, S.I. Yakovlenko. Metastable supercooled plasma // Phys. — Usp. – 1994. – Vol. 37., No. 3. – P. 279.

20. S.A. Maiorov. Effect of ion collisions on the parameters of dust-plasma structures // Plasma Phys. Rep. – 2006. – Vol. 32., No. 9. – P. 737.

IRSTI 29.27.19

The plasma parameters and neutron yield at device of "Plasma focus"

A.M. Zhukeshov[1,*], Zh.M. Moldabekov[1] and A.Ioffe[2]

[1]*al-Farabi Kazakh National University, 71, al-Farabi Ave, 050040, Almaty, Kazakhstan*
[2]*Centre for Neutron Science at Heinz Maier-Leibnitz Zentrum, Lichtenberg str.1, 85747, Julich, Germany*
[*]*e-mail: azhukeshov@gmail.com*

Present work presents calculations and experimental studies on the formation and dynamics of plasma on the "plasma focus" set up. Physical conditions were determined and critical parameters were calculated for estimating the neutron yield for kilojoule and megajoule set ups. The results of plasma diagnostics and flow formation in the CPA-30 and PF-4 set ups are also shown. A comparison of calculated data and experimental values is performed. The value of the neutron yield parameter is justified and the possible cause of the appearance of saturation is indicated. The rationale for the development of further research in the direction of creating conditions for thermonuclear fusion in installations of the plasma focus type is given. The neutron flux was observed on high-voltage gas discharges with a specific geometry of the electrodes. The result of measuring the anisotropy of the neutron yield along the axial z and radial φ directions was equal to $Y_n(z)/Y_n(\varphi) \sim 2 \div 3$, which contradicts the thermonuclear mechanism.

Key words: neutron yield, plasma focus, maximum discharge current, electrode, silver and indium foils.
PACS number: 29.40.−n.

1 Introduction

The tasks of creating powerful sources of neutron fluxes and X-ray radiation are relevant for a number of industries of production and medicine, but the problem of solving the problem of thermonuclear fusion is even more acute [4-5]. One of the new developing approaches in the creation of thermonuclear installations is the method based on plasma generation in installations of the plasma focus type. Plasma focus (PF) is a pulsed unsteady clotof hightemperature dense hot plasma. When using deuterium as working gas, the PF is a localized source of neutrons and hard radiation. However, when using other materials, such as boron, the synthesis reaction may be without a neutron yield, but in this case, the energy yield of the reaction will be different. Therefore, the study of the possibilities of using plasma focus in thermonuclear energy is very important.

The phenomenon of "plasma focus" was discovered in the middle of the twentieth century, independently to each other by N.V. Filippov (USSR) [1] and J. Mather (USA) [2] in studies conducted under the program of controlled thermonuclear fusion. PF attracted interest by researchers, when the working chamber of the PF was filled with a rarefied isotope of hydrogen with deuterium, a powerful short impulse of fast neutrons and X-rays is generated inside the chamber of the discharge current. The discharge current usually measured in hundreds of kilo Amperes [3,4]. The first PF installations had an energy reserve of 50 kJ. In this case, the neutron yield achieved at these facilities was $\sim 10^9$ neutrons per pulse. The neutron pulse duration of the PF is t ~ 100 ns. From the practical point of view, installations with PF are used as sources of neutrons and hard radiation for solving a number of scientific and technical problems: materials science and blanket tests for controlled thermonuclear fusion; neutron therapy; pumping laser media; interactions of powerful beams with plasma, etc. In recent years, the direction of creating devices that are more compact has been developing [5, 6].

There is more than a dozen PF set up in the world: the PF-1000 set up (Warsaw, Poland) has a capacity of 1 MJ, the Tulip plasma set up with power from 4 kJ to 0.4 MJ (Moscow, Russia), and others [7-8]. Previously, the authors conducted experiments on a pulsed plasma accelerator PF-30. The power of the CPA-30 set up is 35 kJ, the discharge current is 450 kA, and the duration is 7 μs. On this set up we have formed dense, discharge plasma clots, and studied their dynamics, as well as the basic laws of plasma beam focusing [9]. In particular, it has been shown that the dynamics of light and dense plasma flows differ significantly not only in flow rate but also in the role of ions in plasma acceleration and the whole structure of the plasma flow [10].

The use of focus plasma in thermonuclear reactors was considered in [11–12]. With an adequate level of understanding of these processes, new perspectives are emerging for the creation of a fusion reactor based on new data. Therefore, it is necessary both to study the possibility of creating an alternative type of thermonuclear reactor at the plasma focus installations and to conduct experiments on existing installations. In this paper, the problem is posed to theoretically calculate the parameters of the neutron yield and then compare it with the experiment.

2 Theoretical part.

A feature of the plasma focus-type installations is the dependence of the neutron yield on the energy E stored in a capacitor battery, and accordingly on the magnitude of the discharge current at the moment of pinching I_p:

$$Y_n = 10E^2 \tag{1}$$

$$Y_n = 10^{-13} I_p^4 \tag{2}$$

The PF set up of the kilojoule range, the inductance of the discharge chamber and the plasma column can be neglected, and then the discharge inductance will be determined by the inductance of the battery and lead wires. The value of the maximum discharge current for these installations is found by the formula (2), taking into account the energy stored in the capacitor battery is equal to:

$$I_m = \sqrt{\frac{2E}{L}} \tag{3}$$

Expressing the energy from equation (6), and substituting the resulting expression into equation (3), we obtain

$$Y_n = 2{,}5 \cdot I_m^4 L \tag{4}$$

From equation (6) it follows that the neutron yield for installations with kilojoule power is determined by the magnitude of the maximum discharge current.

The practical evaluation of formula (4), was calculated the neutron yield value for the PF-30 experimental setup. The capacitor battery consisted of 9 to 18 capacitors, each with a capacity of 3 μF and an inductance of 10^{-7} H.The maximum battery voltage is 30 kV. The maximum neutron yield for an installation with a capacitor battery with a capacity of 27 μF (9 capacitors) was $1.5 \cdot 10^9$ neutrons/pulse, and for a battery with a capacity of 54 μF (18 capacitors) consist $5.9 \cdot 10^9$ neutron/pulse.

The electron concentration can be found using the following expression for the electrodynamic model:

$$n_e = \frac{I^2 f_0 \mu_0 t}{4\pi\varepsilon r^2} \tag{5}$$

Where I – current, f_0 – frequency, μ_0 - magnetic constant, r – the distance between the electrode, ε – ionization energy. From equation (5) it follows that the concentration of electrons depends on the current and the distance between the electrodes, which is illustrated in Figure 1. One can see that the electron concentration decreases with increasing anode radius. The change in the current of the circuit also affects n, it is clear that an increase in the electron temperature is affected by an increase in the current, but at the same time, the pulse time decreases. If the maximum current value is 1 MA, the electron temperature will take its maximum value of 126 eV, and the pulse time will be a minimum of 1 μs. More accurate determination of the maximum electron temperature is necessary to calculate the optimum ratio of the anode and cathode [19]. The obtained data allows us to determine the values of the electron temperature when the anode radius varies from 0.25 cm to 2.25 cm.

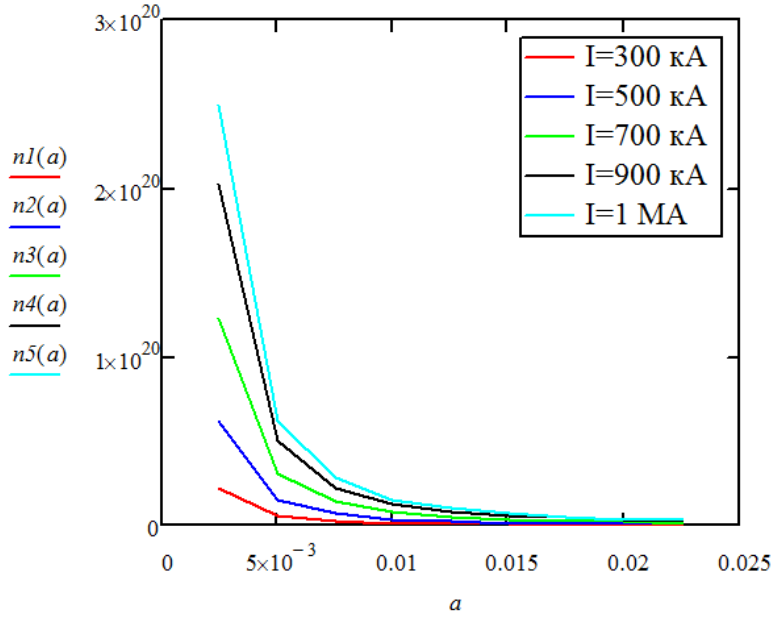

Figure 1– Changes in the concentration of electrons from the distance between the electrodes for different values of current

Thus, the maximum temperature and electron concentrations were $2.5 \cdot 10^{16}$ cm^{-3} and 126 eV, and the neutron yield for the PF-30 installation may be $5.9 \cdot 10^{9}$ neutron/pulse. Calculations on the electrodynamic model show that the electron concentration decreases with increasing anode radius.At the same time, an increase in current leads to an increase in concentration. In addition, it was found that an increase in the electron temperature is influenced by an increase in the current, but at the same time, the pulse time is reduced.

3 Measurement of neutron yield

To register a short duration neutron emission from Plasma Focus type pulsed sources at the P.N. Lebedev Physical Institute of Russian Academy of Sciences, a special detection system was developed, which is described in detail in [15-16]. The task was to develop equipment for the registration of neutron radiation of the DD reaction for PF type set ups of relatively low intensity ($5 \cdot 10^{6}$–$2 \cdot 10^{7}$ neutrons per discharge) under conditions of powerful fluxes of electromagnetic plasma radiation in the presence of intense electrical and magnetic interference, the calibration of this system. Measurement of neutron fluxes in these conditions can be successfully carried out using activation detectors. Activation detectors allow it possible to make measurements with a shift in time with respect to the moment of plasma generation after extinguishing of electromagnetic radiation and the cessation of interference [16-19]. Measurements produce on standard equipment and with greater accuracy than the accuracy achieved indirect measurements of the amplitude of the neutron pulse.

The halogen Geiger counters CTC–5 (CTC–6) used as sensors in these detectors (Figure 2) were wrapped with indium (or silver) foil and placed in the center of the cylindrical moderator box. The type of sensor used has a relatively large “dead time” (~100 μs). Therefore, when measuring large neutron yield, it is also important not to have an excessively large number of samples on the recording equipment in order to minimize the errors of the recording system due to the relatively large resolution time of the system on the counting input.

The activation detector variant with the CTC–5 sensors are characterized by lower sensitivity as compared to activation detectors of similar types, as the detector has a relatively small container – moderator and the CTC–5 sensor itself has small dimensions compared, for example, the CTC–6 sensor with similar propertieswith, respectively, fewer counting on the measuring equipment. Measurements of neutron fluxes under these conditions can be successfully carried out using activation detectors [7, 14, 15, 16].

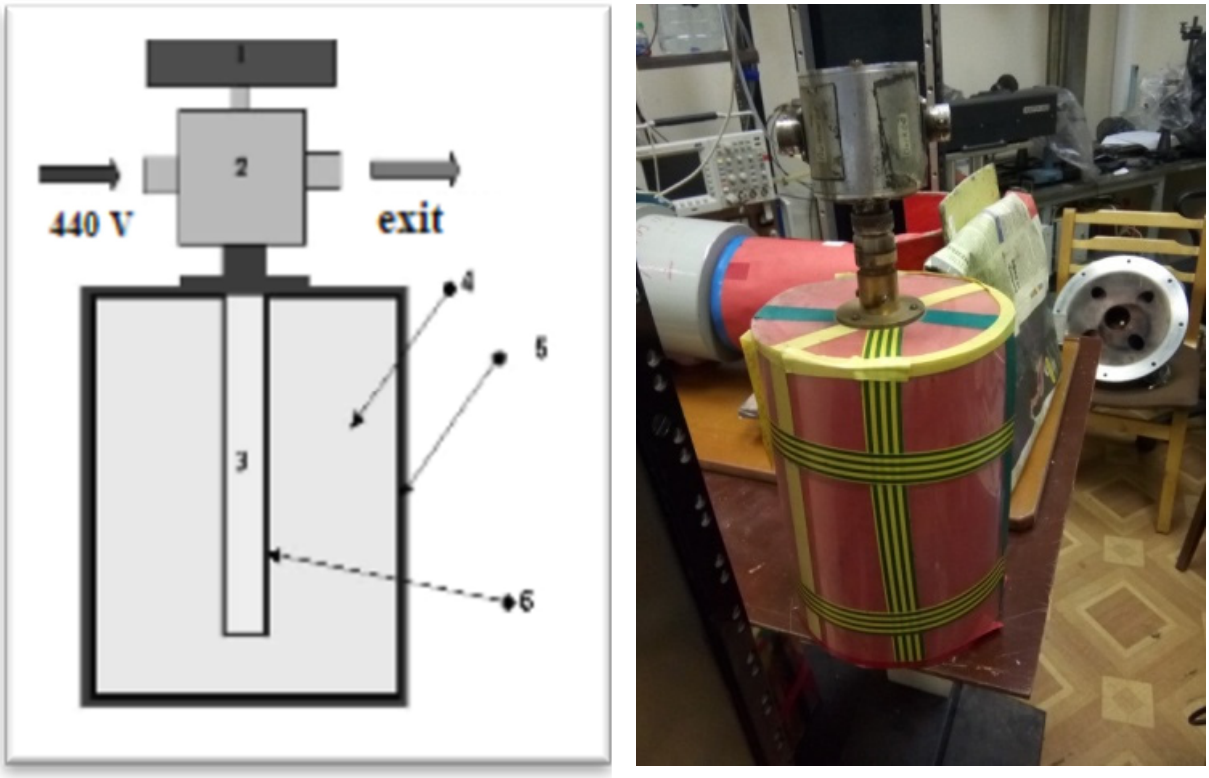

1 –battery power supply of the electric circuit; 2 – electrical diagram of the activation counter; 3 – halogen Geiger counter CTC–5 (CTC–6); 4 – cylindrical block of activation counter retarder; 5 – the layer of cadmium; 6 – activated foil (InorAg).

Figure 2 – Neutron detector developed in P.N. Lebedev Physical Institute of Russian Academy of Sciences.

Let the detector be irradiated with fast (2.5 MeV) neutrons from a constant source of intensity I (neuter./sec.) located at the point from which the detector is visible at a solid angle Ω. Thermal neutrons (after the process of slowing down fast neutrons) inside the moderator block activate foils that wrap the sensor. In general, the absolute neutrons yield:

$$N + \Delta N - \overline{N}_{ph}^{\Delta t} = I\left(\frac{\Omega}{4\pi}\right)\left[\varepsilon' T'\left(1 - e^{-t_1/T'}\right)e^{-t_2/T'}\left(1 - e^{-\Delta t/T'}\right) + \varepsilon'' T''\left(1 - e^{-t_1/T''}\right)e^{-t_2/T''}\left(1 - e^{-\Delta t/T''}\right)\right] \quad (6)$$

The indices “one stroke” and “two strokes” refer respectively to the parameters for indium isomers In^{116} and In^{116m} or the isotopes Ag^{108} and Ag^{110}. Description of other parameters in the formula (6) is given in [8, 9].

The results of experiments on measuring the neutron yield at the PF-4 installation [7] are shown in Figures 3 and 4 for indium and silver foil respectively, used as a fast neutron moderator.

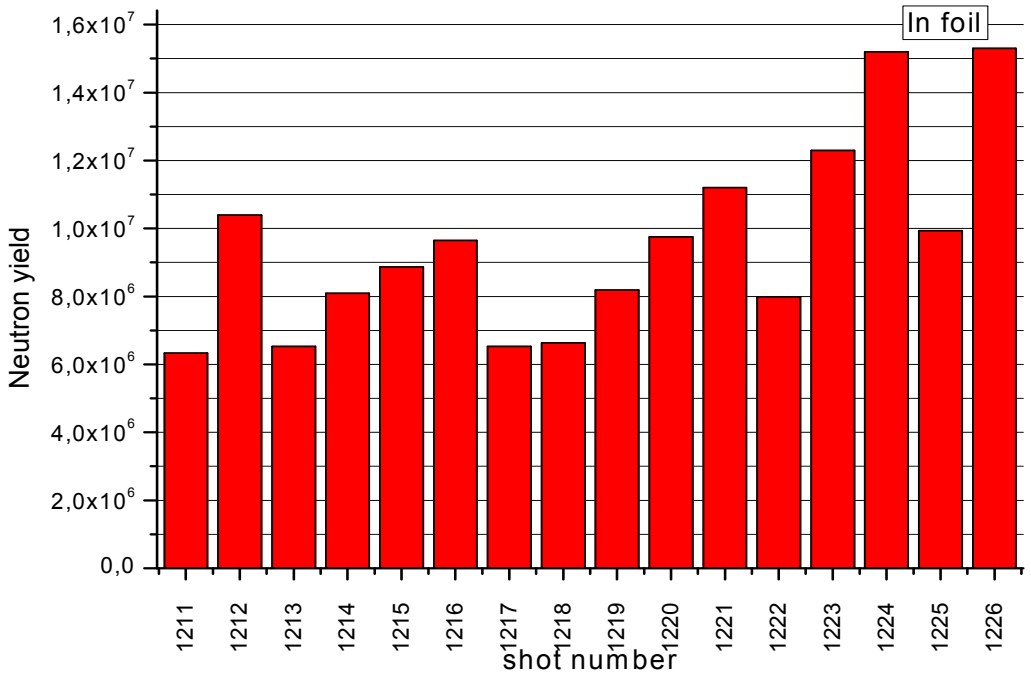

Figure 3 – PF-4 neutron yield with indium foil

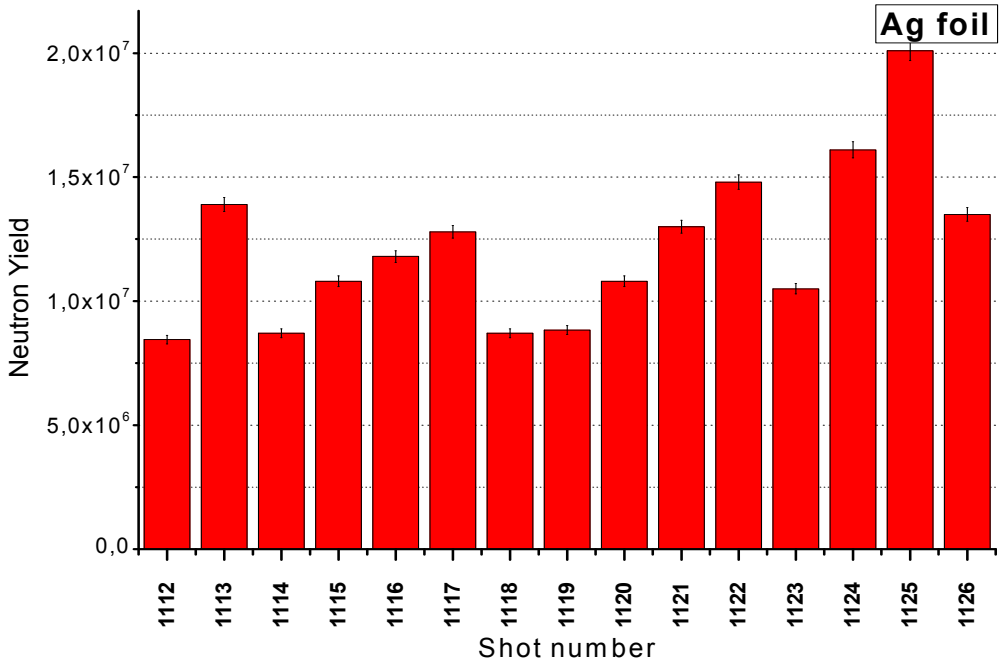

Figure 4 – PF-4 neutron yield with silver foil.

4 Conclusions

The results of calculations and experiments shown that for installations like plasma focus PF-30 and PF-4 it is possible to obtain discharge currents of hundreds of kiloamperes and current rise rates up to ~ 10^{11} A/s.The current data determined from the experiments and the plasma parameters agree with the calculated values given above. At the same time, the neutron yield was calculated on the basis of the thermodynamic model, i.e. a priori assuming its thermonuclear origin. But a review of the experimental facts suggests that neutron emission may be associated with other conditions and is not characteristic only of "plasma focus". For example, the neutron flux was also observed on high-voltage gas discharges with a specific geometry of the electrodes, creating field strength sufficient for "runaway of electrons" [13]. In this case, the typical times of processes are counted in hundreds of nanoseconds, which are also observed for a plasma focus.

Previously reported experimental work that when using deuterium gas in the PF, neutron yield is observed with the energy distribution along the axis of the system and energy of 2.45 MeV.Neutron radiation had an isotropic distribution and its duration was of the order of tens of nanoseconds.It was assumed that these neutrons are of thermonuclear origin, which leads to isotropic neutron radiation. However, the result of measuring the anisotropy of the neutron yield along the axial z and radial φ directions was equal to $Y_n(z)/Y_n(\varphi) \sim 2 \div 3$, which contradicts the thermonuclear mechanism. In addition, the average energy of neutrons in the axial direction was greater than the energy of thermonuclear neutrons (2.45 MeV). This fact indicates that it is worth considering the non-thermal mechanism of neutron emission.

Thus, today, both thermonuclear and beam emission options are possible, but the details and mechanism of ion acceleration still need to be clarified.

References

1. V. I. Krauz. Progress in plasma focus research and applications // Plasma Physics and Controlled Fusion. – 2006. –Vol. 48, No.12. – P. B221.

2. J. W. Mather. Formation of the high-density deuterium plasma focus // Phys. Fluids. – 1965. – Vol. 8. – P. 366.

3. N.V. Filippov, T.I. Filippova, I.V. Khutoretskaia, V.V. Mialton, V.P. Vinogradov. Megajoule scale plasma focus as efficient X-ray source // Physics Letters A. – 1996. – Vol. 211, No. 3. – P. 168-171.

4. Y.C. Francis, R. Eskridge, J. Smith, A. Martin, J. Cassibry, S.T. Wu. A plasma accelerator concept for application to magnetized target fusion // Z-Pinches Conference. – Florence: Alabama university press. – 2006. – P. 456 - 467.

5. L. Soto, C. Pavez, J. Moreno, M. Barbaglia, A. Clausse. Nanofocus: an ultra-miniature dense pinch plasma focus device with submillimetric anode operating at 0.1 J // Plasma Sources Sci. Technol. – 2009. –Vol.18. – P. 015007.

6. A. Skoulakis, G. C. Androulakis, E. L. Clark1 et al. Portable pulsed neutron generator // International Journal of Modern Physics: Conference Series. – 2014. – Vol. 27. – P. 1460127.

7. V.Ya. Nikulin, S.N. Polukhin, A.A. Tikhomirov. A Simple criterion for the snowplowing efficiency of the working gas in a kJ plasma focus // Plasma Physics Reports. – 2005. – Vol. 31, No. 7. – P.591-595.

8. A.M. Zhukeshov, B.M. Ibraev, Sh.G. Giniyatova, B.M. Useinov, V.Ya. Nikulin, A.T. Gabdullina, A.U. Amrenova. Parameters calculation and design of vacuum camera for «Plasma Focus» facility // International Journal of Mathematics and Physics. – 2016. – Vol.7, №1. – P. 137-140.

9. A. Zhukeshov, A. Amrenova , A.Gabdullina, Z. Moldabekov. Calculation and analysis of electrophysical processes in a high-power plasma accelerator with an intrinsic magnetic field // Technical physics. – 2019. – Vol. 62, No.3. - P. 342 -347

10. L. Soto. New trends and future perspectives on plasma focus research // Plasma Phys. Control. Fusion. – 2005. – Vol. 47. – P. A361-A381.

11. F. Castillo, M. Milanese, R. Moroso, J. Pouzo. Evidence of thermal and non-thermal mechanisms coexisting in dense plasma focus D-D nuclear reactions // J. Phys. D: Appl. Phys. – 2000. – Vol. 33, No. 2. – P.1.

12. M.I. Lomaev, B.A.Hechaev, B.N. Padalko. Neutron emission at nanosecond discharge in deuterium in an inhomogeneous electric field // JTPh. – 2012. – Vol. 82, No.1. – P. 126–133 (in Russian).

13. O. N. Krokhin, V.Ya. Nikulin, M. Scholz, I.V. Volobuev. The measurements of neutron emission on plasma focus installations with energy ranging from 4 to 1000 kJ // Proc. of 20th Symp. on Plasma Physics and Technology. Prague. – 2002. – P. 61.

14. M. Scholz, B. Bieńkowska, M. Borowiecki, I. Ivanova-Stanik, L. Karpiński, W. Stępniewski, M. Paduch, K. Tomaszewski, M. Sadowski, A. Szydłowski, P. Kubeš, J. Kravárik. Status of a mega-joule scale Plasma-Focus experiments // Nukleonika. – 2006. – Vol.51, No.1. – P. 79-84.

15. O.N. Krokhin, V.Ya. Nikulin, I.V. Volobuev. Compact activation detectors for measuring of absolute neutron yield generated by powerful pulsed plasma installations // 21nd Symposium on Plasma Phys. And Techn., June 2004, (Praha, Czech. Rep.). Czech. J. Phys. – 2004. – Vol. 54. – P.1.

16. N. A. Vlasov. Neutrons. -1955. Moscow: State ed. technical – theoretical literature (in Russian)

17. A.M. Zhukeshov, B.M. Ibraev, B.M. Useinov, Sh.G. Giniatova. Pulsed plasma flow interaction with a steel surface //High Temperature materials and processes. – 2015. – Vol. 19, No.2. – P. 113-119.

18. H. Rahal, C. Deutch, M.M. Gombert. Temperature dependent quantum pair potentials and ionization in Helium like plasma //Physical Sciences and Thechnology. – 2017. – Vol.4, No. 2 – P. 29-46.

19. E. Ishitsuka, E. Kenzhina. Evaluation of tritium release curve in primary coolant of research reactor // Physical Sciences and Thechnology. – 2017. – Vol.4, No. 1. – P. 27-33.

20. B.M. Ibraev, A.M. Zhukeshov, A.T. Gabdullina, A.U. Amrenova. Research of plasma accelerator KPU-30 // Int. J. of Math. and Physics. – 2012. – Vol. 3, No.1. – P. 50 – 53

IRSTI 29.27.21

Search for structures in the distribution of particles from the central area of wide atmospheric showers conducted on the Adron-55 installation

K.M. Mukashev[1], A.Kh. Arginova[2], A.D. Baisenova[2], B.A. Iskakov[1,2], R.A. Mukhamedshin[3], O.A. Novolodskaya[2], V. V. Piskal[3], V.A. Ryabov[3], T.Kh. Sadykov[1,2,*], A.S. Serikkanov[2], Y.M. Tautaev[1,2], V.V. Zhukov[3] and N.N. Zastrozhnova[2]

[1]*Abai Kazakh National Pedagogical University, Dostyk Ave., 13, 050010, Almaty, Kazakhstan*
[2]*Satbayev University, Institute of Physics and Technology, 11, Ibragimov str.,040907, Almaty, Kazakhstan*
[3]*P.N. Lebedev Physical Institute of the Russian Academy of Sciences, Leninsky Prospect 53,119991, Moscow, Russia*
**e-mail: leodel@mail.ru*

The ionization calorimeter “Adron-55”, located at an altitude of 3340 meters above sea level, is part of the unified registration system for the shower installation of the Tian-Shan high-mountain station. The “Hadron-55” installation is a 2-tier ionization calorimeter consisting of a shower system, a gamma block and a hadron block located under it with a vertical air gap of 2.2 meters. The calorimeter consists of 6 layers of ionization chambers with 144 chambers in each layer and a spatial resolution of the WAS structure equal to 11 cm. The total area of the calorimeter is 55 square meters with an absorber thickness of 1150 g / cm^2. The calorimeter also contains helium counters for recording the neutron component. The central shower calorimeter system contains 30 scintillation detectors with an area of 400 m^2 and 8 peripheral Sc-detectors at a distance of up to 100 m. The total area of the entire recording system is ~ 30000 m^2. Over 4 years of operation, more than 120,000 events with energies above 10^{15} eV have been recorded. Currently, the processing and analysis of the data being obtained are performed.

Key words: detector, hadron, calorimeter, installation, ionization.
PACS numbers: 13.30.Eg, 29.40.Cs

1 Introduction

Quite often forgotten that particle physics has originated from cosmic ray physics. After splendid results of particle physics thanks to accelerator technique advances we are again witnessing some interest to super high energy cosmic ray studies due to some new effects observed at energy range above 10^{15} eV which are hard to explain within the conventional processes governed by Standard Model. These new phenomena observed in cosmic ray experiments can be accounted for by production of new particles or by new interaction mechanisms. The main types of the unusual phenomena in cosmic rays at energies greater than 10^{15} eV are as follows:

• the problem of the PCR energy spectrum "knee" at energy $E_0 \sim 3 \cdot 10^{15}$ eV;

• the cut-off of the primary cosmic ray spectrum at energy $E_0 \sim 3 \cdot 10^{19}$ eV;

• the appearance of so-called Centauro- and Anti-Centauro types of events with abnormal ratio of charged and neutral hadrons out of conventional statistical fluctuations;

• the abnormally high fraction of so-called "halo" events observed with XRECs which contain a diffuse macroscopic spots on X-ray films characterized by high energy flux (~20 TeV/mm^2);

• the alignment of super high energy ($\sum Evisible \geq 700$ TeV) gamma-ray-hadron families characterized by an alignment of tracks of the most energetic particles along a straight line;

• the so-called long-flying particles with abnormally weak hadronic absorption violating conventional exponential dependence.

It is worth noting that some indications to existence of the alignment effect, first observed in the *Pamir* XREC experiment [1], were recently obtained at collider experiments, i.e., RHIC and LHC, where so-called "ridge" effect manifesting strong azimuth anisotropy was discovered [2].

Thus, at present, an interesting situation has been created in cosmic rays at energies above 10^{15} eV. On the one hand, a certain number of phenomena are observed mainly in the region of the trunk (center) of a wide air shower (EAS), which do not fit into the framework of traditional ideas about the nuclear-cascade process in the atmosphere. On the other hand, so far no serious deviations from the accepted Standard Model have been found in experiments on accelerators. If we recall that a trunk region with a radius of up to 10 meters at a distance of 20-30 km from the point of the first interaction of a particle that produced an EAS, belongs to the pseudo-fastness region (η~12) that is not available on accelerators, then the study of the trunk is a good addition to accelerator experiments.

It is also possible that unusual particles can be present in the cosmic-ray flux at energies above 10^{15} eV, which are the primary cause of the observed anomalous phenomena in experiments with cosmic radiation and which, due to their properties, are not observed in accelerator experiments. The installation “Hadron-55” is aimed at solving a number of astrophysical and nuclear physics problems: the study of interactions of high-energy hadrons in the central part of EAS trunks; search for sources of high-energy cosmic rays [3].

2 Installation geometry

Figure 1 shows a schematic plan for the installation of the Hadron-55, consisting of the central and peripheral parts. The central part consists of an ionization calorimeter, a scintillation carpet and a muon hodoscope located in the building of the Physicotechnical Institute. The peripheral part consists of 8 SC-detectors located in circles 40 and 100 m. The geographical coordinates of the installation center are: N: $43^0$2’32”; E: 76^0 56’45”.

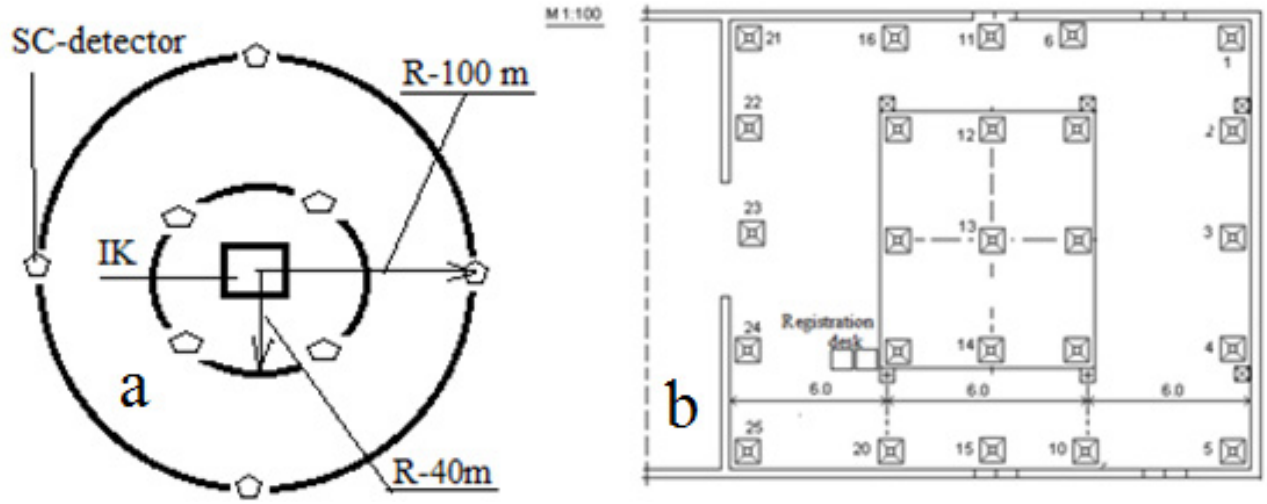

Figure 1 – Schematic plan of the location of the installation "Hadron-55" consisting of a – peripheral and b – central parts.

3 The HADRON-55 setup design

The installation is a two-tier ionization calorimeter (IC) with an area of 55 m^2 and a thickness of 1150 g/cm^2, (see Figure 2) located on the periphery of the installation both inside and outside the building of scintillation detectors covering an area of over 30,000 m^2.

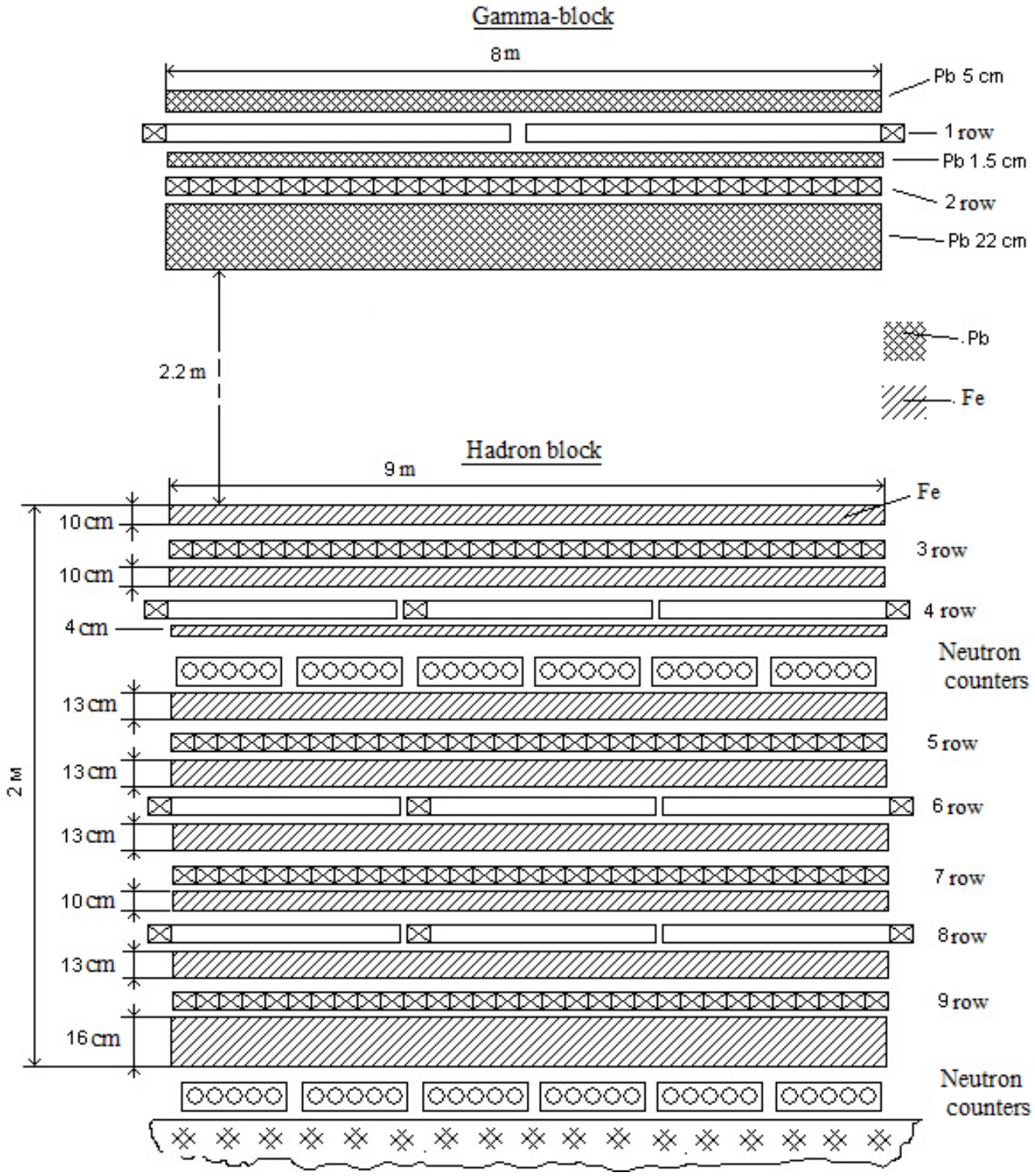

Figure 2 – The two-tier ionization calorimeter "Hadron-55"

The tiers are spaced vertically by 2.2 meters. The upper deck contains a standard XREC (socalled G-block) and two rows of ionization chambers (IC) under it, which are arranged in mutually perpendicular directions. Beneath them, there is a target lead block 22 cm thick in which hadrons of cosmic radiation interact effectively with lead nuclei. The design of the upper tier installation makes it possible to determine the energy of electron-photon component and, in conjunction with the lower tier ("hadron" block) enables experimentalists to reconstruct the particle trajectories.

There are also 24 scintillation detectors 0.25 m2 each which are spread over an area of 324 m^2 at the level of the upper tier.

The lower tier combines the XREC and the underlying ionization calorimeter, which consists of iron absorber with gaps where IC, neutron and Geiger counters are placed. This unit is used to measure the energy of the charged cosmic ray component as well as to determine the particle trajectories. The specific feature of the HADRON-55 setup is that it represents a set of different detectors thus allowing a much more detailed study of characteristics of cosmic ray particle interactions.

According to [3] and our calculations [4] the error in determination of interaction energy in an ionization calorimeter of 1,000 g/cm^2 thick containing six levels of registration is about 10%. Therefore the design of the calorimeter has 9 rows of detectors and the total thickness of the absorber is 1033 g/cm2 that is sufficient for a correct determination of the primary particle energy E_0 with a reasonable accuracy. Scintillation detectors measure the coordinates of the passage of EAS with an accuracy of ~0.5 m, ionization chambers 10 cm. The particle energies are determined with an accuracy of $\Delta E/E \sim 10\%$.

It is envisaged that, in the nearest future, the HADRON-55 setup will work as a part of a new shower array which is now under construction at TSRS. This array represents a network of scintillation detectors located on an area of about two km^2. Thus, measurements of the primary particle energy E_0 and determination of their mass be carried out more reliably that makes it possible to solve the problems planned.

4 Ionization chambers used in the IC

The upper tier of the IC (i.e., G-block) consists of two rows of IC arranged in mutually perpendicular directions. The first row contains 100 ICs and the second one comprises 144 chambers of size $300 \times 11 \times 6$ cm^3 each. The signal read-out of each IC is performed with in-house electronic recording channel developed and fabricated in TSRC. Figure 3 presents a schematic block diagram of a recording channel of the ionization chamber employing the 544UD1 chips of operational amplifiers and the SMP04 cell of analog memory. At the input of the amplifier, there are diodes D1 and D2, which limits the input voltage and partially compress the input range to a logarithmic scale. In the feedback circuit of the output cascade of the amplifier at the 544UD2 chip, a diode is also installed which provides a quasi-logarithmic transfer characteristic of the amplifier. The amplifier of ionization chamber makes it possible to boost signals from 100μV up to 100 V that means that it has a dynamic range (gain) of 10^6.

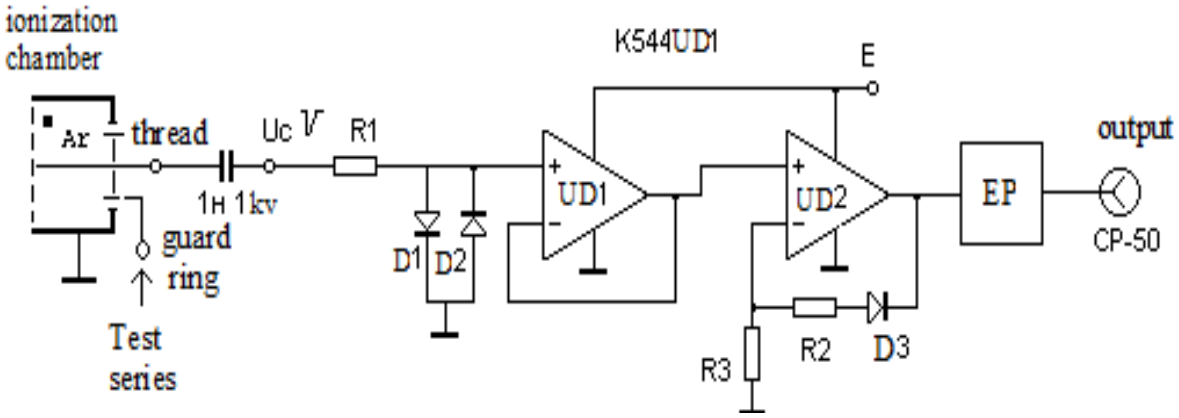

Figure 3 – A schematic block diagram of the logarithmic amplifier of an IC recording channel

Figure 4 shows the calibration characteristic of a logarithmic amplifier. The graph shows that for signals from 100 μV to 10 mV, the measurement error is less than 10%, and for signals from 10 mV to 100 V, the measurement error is less than 1%.

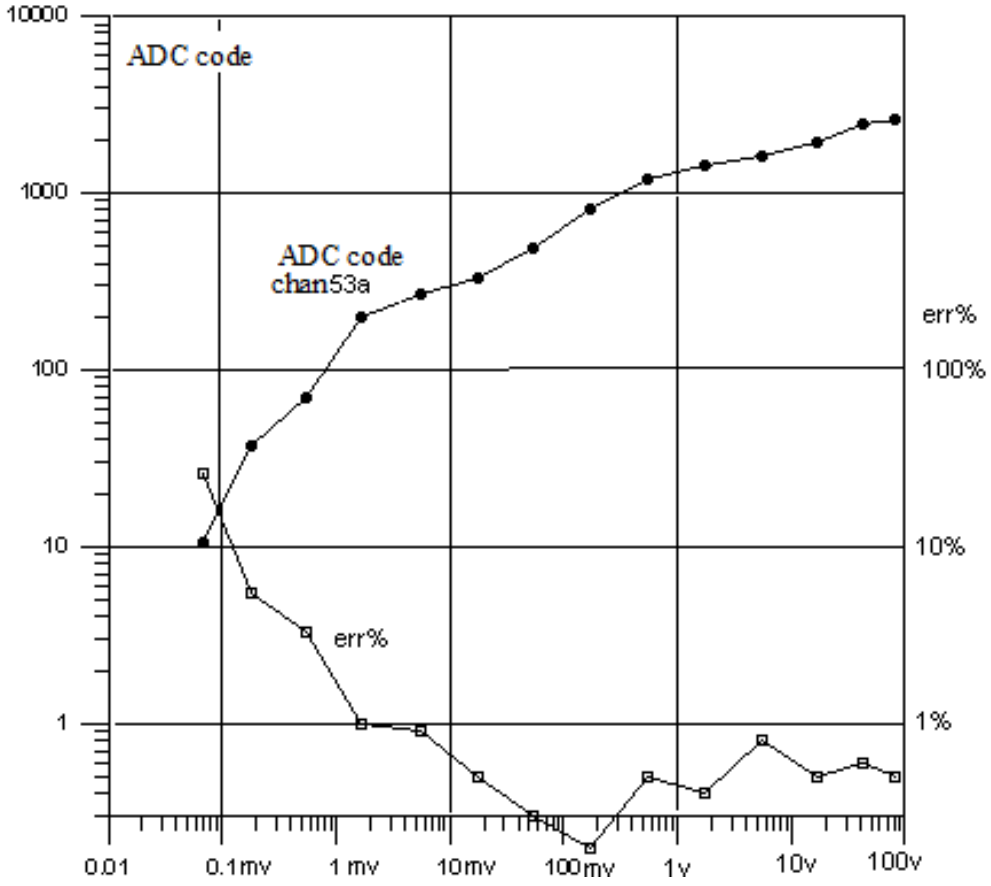

Figure 4 – Transfer function of the amlifier of ionization chamber.

5 Scintillation detectors used in the IC

To detect electron EAS component, the HADRON-55 setup uses scintillation detectors fabricated on the basis of solid plastic scintillators which contain luminescent substances emitting light when charged particles pass through them. The light pulses are recorded by a photomultiplier tube (PMT-110 in our case). Figure 5 shows the structure of the scintillation detector.

A light-tight casing of the scintillator is made of an aluminum sheet of 1 mm thick and is covered inside with white reflective paint. In the lower part of the casing, there is horizontally mounted plastic block of 50×50 cm^2 in size and 5 cm thick. The upper part of the body has the shape of a pyramid on top of which a photomultiplier is mounted together with a voltage divider for dynodes and a PMT signal amplifier. At present, 24 scintillation have been installed and are already under operation.

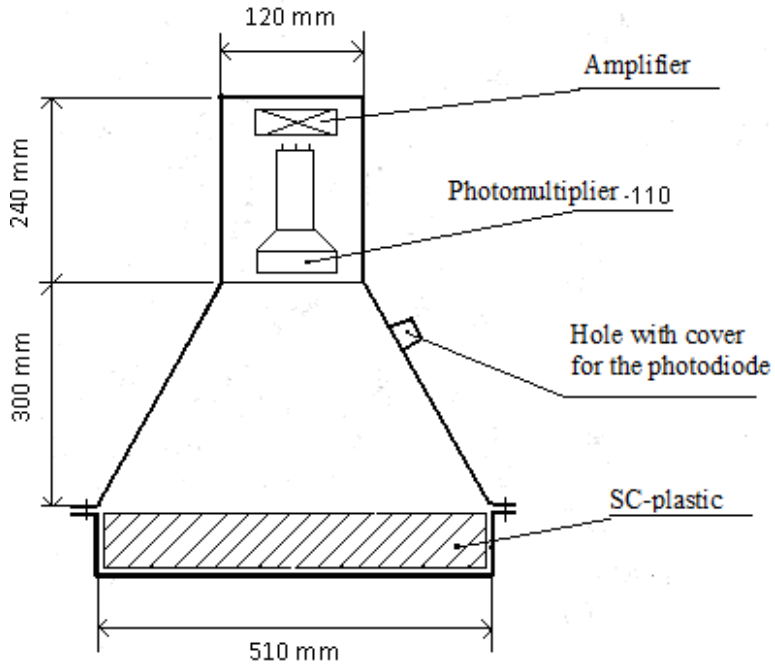

Figure 5 – The design of the scintillation detector

6 Neutron detectors of the IC

The method of energy measuring based on the detection of evaporated neutrons from the nuclei splitting produced by cascade particles was proposed about 30 years ago [5] and is used in analyzing the data of the world network of neutron monitors [6]. However, neutron calorimeters have not yet been widely used. Our project by using a two-tiered IC combines two different methods of particle energy measuring, i.e., the ionization calorimeter method and that of the neutron one. The informativeness of such a combined calorimeter is substantially higher as compared with ionization and neutron calorimeters individually [7]. Indeed, in addition to determining the energy of two independent methods, IC is able to separate gamma rays, electrons and hadrons in the mixed flux of particles due to the fact that the relative neutron yield in electromagnetic cascades as compared with nuclear ones is not more than 5−10% [8,9]. When neutron moderation to thermal energies is used for neutron detection, the design of the IC is practically the same as of common calorimeters. In this case, the signals from the neutrons will be delayed with respect to the ionization signal to tens or hundreds of microseconds because of thermalization and diffusion processes in the material of the moderator and, thus, the detection of ionization and neutron signals can be carried out by the same detectors, such as gas proportional neutron counters, with some time shifting .

The IC has two rows of neutron detectors. The first one is between the third and fourth registration rows, and the second one is just after the 9th row (see Figure 2). This arrangement of neutron detectors allows to determine independently the primary particle energy [10], number of neutrons and their lateral distribution function in the calorimeter.

7 The trigger and the readout systems

The HADRON-55 setup trigger system assumes selection of events by several EAS parameters: total ionization, density of charged component, position of the EAS axis (hitting parameters), etc. The event registration is done by recording detector signals in a computer memory according to a special control (trigger) signal which is generated in a special electronic unit of the setup. It is supposed that the triggers system of the setup will have four different modes. However, nowadays we use only the 1st mode of trigger system operation based on the circuit processing the sum of ionization in two detection levels (rows) of the G-block. The readout system includes a computer and a software package of management, control and processing. The program manages the readout process through the

computer's LPT parallel port, then through the CAMAC data controller which transfers data to the computer memory from the ADC modules installed in the CAMAC crate. With the accumulation of events in the computer memory, the database is formed.

8 Search for structures in the distribution of particles from the central area of EAS

For illustration, was used event № 9, which occurred on January 1, 2019 at 2 hours 24 minutes 49 seconds. It was registered in six rows of the ionization calorimeter and in 18 scintillation detectors, see Figure 1 and 2.

In the first and second rows of the gamma block, the ionization chambers are located in mutually perpendicular directions. This allows you to determine the direction and energy of the showers passing through this layer, which forms the first level of the ionization calorimeter. The third and fourth, fifth and sixth rows of the ionization calorimeter, forming the second and third levels, are considered in a similar way. In fig. 6 shows three levels of ionization calorimeter. The X and Y axis shows the location of the ionization chambers. On the Z axis, the amount of ionization during the passage of charged particles. For this event, the zenith angle is 7^0, azimuth angle is 205^0. The energy of the primary particle is $2{,}4 \cdot 10^{15}$ eV.

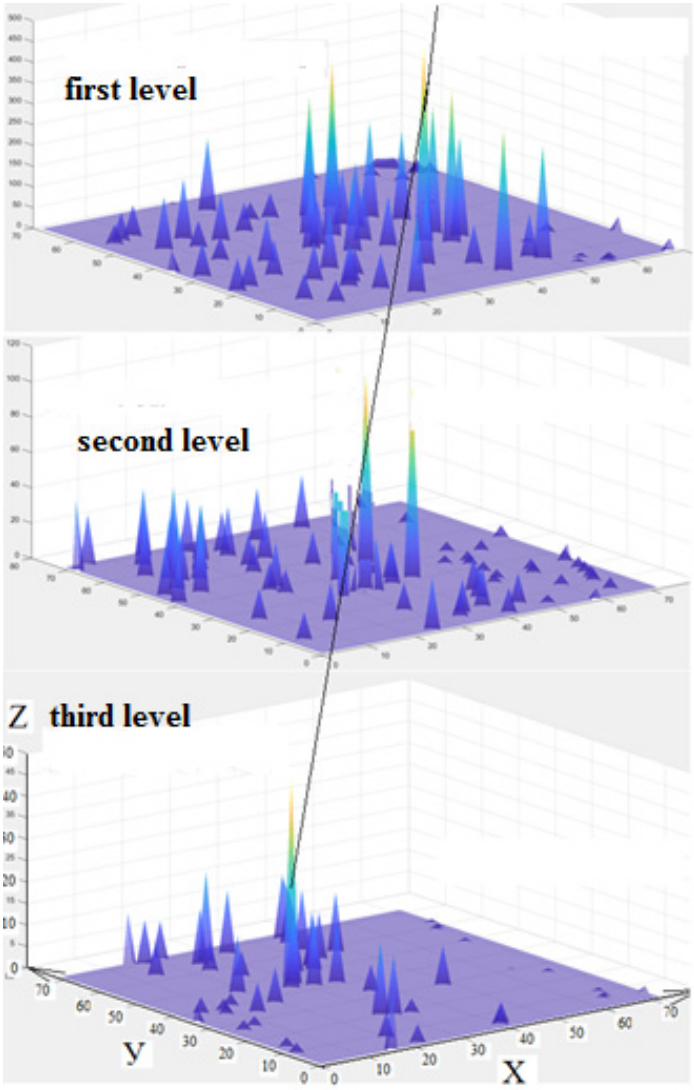

Figure 6 – Illustration of the position of the axes of EAS event №9 in the plane of the "carpet" of the ionization calorimeter

9 Results

In order to verify the correct operation of the entire electronics of the calorimeter, the adequacy of programs and methods for calculating the energy of primary particles, we calibrated the setup by determining the flux of particles of cosmic rays with an energy of $E_0 \geq 3 \cdot 10^{12}$ eV. It is known that the flux of cosmic particles at a given height is a fairly stable and well studied quantity. Therefore, a comparison of the experimentally measured flux values on a new installation with the results obtained on already well-tested plants that have worked stably for a long period allows us to estimate the accuracy of measurements on our plant. It was logical to compare our data with the results of the work of the ionization calorimeter of the Tien-Shan plant of LPI of Russia, located on the same site with our calorimeter. According to their data of [11], the total particle flux at an altitude of 3340m is I(≥1ТэВ)=0,8 parts/m^2·ster·h. The particle flux obtained in our experiment is equal to I(≥3ТэВ)=0,15±0,01 part m·ster·h. To compare flows, it is necessary to bring them to the same threshold energy. If we bring our value to the energy of 1 TeV, then we get (≥3 TeV)=(0.82±0.04) parts/m^2·ster·h, which well coincides with the data of [11]. Thus, all the systems of the created installation "Adron-55" work correctly and in a steady mode.

Currently, the facility operates: eight rows of ionization chambers or four levels; twenty-five scintillation detectors inside the building; four scintillators outside the building located at a distance of 40 meters from the center of the calorimeter. In 2019, about six thousand events with energies greater than $2 \cdot 10^{15}$ eV were recorded. The interactions when the share of primary energy is transferred only to the neutral component is 6%.

References

1. A.S. Borisov, A.P. Chubenko, O.D. Dalkarov, V.P. Pavluchenko, V.S. Puchkov, V.A. Ryabov, S.B. Shaulov, A.L. Shchepetov. HADRON-55 complex setup for study of hadron interactions within the central part of EAS cores// ICRC, PoS. – 2015. – P. 570.

2. L. A. Anchordoqui, D. Ch. Dai, H. Goldberg. Searching for the layered structure of space at the LHC// ANL-HEP-PR-10-53, NUHEP-TH/10-23. – 2011- arXiv:1012.1870v2 [hep-ph].

3. D.S. Adamov, N.G. Vildanov, A.D. Erlykin, S.B. Shaulov et al. // Spatial-energy characteristics of the electron-photon and hadron components of EAS// Preprint. Moscow. FIAN. – 1989. – Vol. 187. – P. 12.

4. M.K. Babaev, A.S. Baigubekov et al., Analysis of nuclear-electromagnetic cascades produced by cosmic ray hadrons in the energy range ≥ 1013 eV// Izv. MON RK. – 2001. – Vol. 6. – P. 53.

5. V.I. Yakovlev. The study of the energy spectrum of particles at the mountain level// Avtoref.diss. Cand. Ph.-m.s. M. – 1969. – P. 25.

6. L.I. Dorman. Experimental and theoretical foundations of astrophysics of cosmic rays// M.: Nauka, 1975. – 256 p.

7. V.V. Amosov, G.I. Merzon, T. Saito, et al. Calculation of the processes of generation, transport and detection of neutrons in some experimental facilities using the Monte Carlo method // Letters to the Journal of Technical Physics. - 1998. – Vol. 24. – P.20. (In Russian)

8. Ryazhskaya O.G. Neutrino from gravitational collapse of stars // Dis. Dr. Phys.-Mat. sciences. M.: INR USSR Academy of Sciences, 1986.

9. Enikeev R.I., Zatsepin R.T., Korolkova E.V. et al. Hadrons generated by cosmic ray muons underground // Nuclear Physics. – 1987. – Vol. 46, No. 5. – P. 1492. (In Russian)

10. Antopov V.P., Vildanova L.I. et. al. Very high energy cosmic ray interactions // Izvestiya RAN. Ser. Phys. - 2002. – Vol .66. – P. 1576.

11. J.A. Simpson, W. Fongen, S.B. Treiman. Cosmic Radiation Intensity-Time Variations and Their Origin. I. Neutron Intensity Variation Method and Meteorological Factors// Phys. Rev. B. – 1953. – Vol. 90, No. 5 – P. 934.

12. The CMS collaboration, observation of long-range near-side angular correlations in proton-proton collisions at the LHC [hep-ex/1009.4122].

13. The ALICE collaboration, Multiplicity dependence of two-particle azimuthal correlations in pp collisions at the LHC// JHEP. – 2013. – Vol. 09. – P. 49.

14. V.S. Murzin, L.I. Sarychev, Cosmic rays and their interactions. Moscow. Atomizdat. – 1968. – P.55.

15. A.S. Borisov, V.M. Maximenko, V.S. Puchkov et al., Some interesting phenomena observed in cosmic-ray experiments by means of X-ray emulsion technique at super accelerator energies// Phys.Part.Nucl. – 2005. – Vol. 36. – P. 1228.

16. L. T. Baradzei et al. [Pamir Collaboration]// Bull. Russ. Acad. Sci. Phys. – 1986. – Vol.50, No. 11. – P. 46.

17. V.S Aseykin, N.M. Nikolskaya, V.P. Pavlyuchenko, Universal algorithm for estimating the basic parameters of EAS// Preprint. Moscow. FIAN. – 1987. – Vol. 31. – P. 10.

18. A.S. Borisov, V. G. Denisova, V. I. Galkin et al.// Proc.30th ICRC, Merida. – 2007. – Vol. 4. – P.593.

19. V.V. Arabkin, B. Afanasyev, M.M. Nikolskaya, P V.P. avlyuchenko, V.V. Piskal et al., Primary databank of the complex installation “Adron” TSHVNS LIAN// Preprint. Moscow. PhIAN. – 1986. – Vol. 255. – P. 11.

20. B.A. Iskakov, V.V. Oskomov, O.A. Kalikulov. Registration of muon and electron-photon component of cosmic radiation by the godoscopic modules of the neutron supermonitor 6NM-64// Research in Technical Sciences. – 2015. – Vol. 3 (17). – P. 17.

21. V.A. Ryabov, R.U. Beisembayev, v S.P., Bezshapo A.S. Borisov, A.P. Chubenko, O.D. Dalkarov, A.V. Gurevich, G.G. Mitko, R.A. Nam, V.P. Pavlyuchenko, et al., Modern status of the Tien-Shan cosmic ray station// EPJ Web of Conferences. ISVHECRI 2016 – 19th International Symposium on Very High Energy Cosmic Ray Interactions. – 2017. – P. 12001

Andrey Stepanovich Drobyshev, scientist who developed cryophysics in Kazakstan, obituary (11.09.1950 – 20.12.2018)

Andrey Stepanovich Drobyshev, physicist, doctor of physical and mathematical sciences, professor at al-Farabi Kazakh National University and chief researcher of the Institute of Experimental and Theoretical Physics (IETP) and Natoinal Nanotechnological Laboratory of Open Type (NNLOT). He was a remarkable man and a great developer of the scientific direction of "Cryophysics" in the Republic of Kazakhstan. He has passed away on 20th December, 2018 at the age of 68.

Andrey S.Drobyshev was born on September 11, 1950 in the village of Lukyanovka, Omsk Region. In 1959, his family moved to Kazakhstan and in 1967 he graduated from high school and entered the Department of Physics at S.M. Kirov Kazakh State University. In 1973 he graduated from the university with the qualification of "physicist, teacher of physics in German" and was distributed to the Department of Physical Hydrodynamics (later, the Department of Thermal Physics), which is still in operation.

Since 1975, he has been actively involved in research work, being the executor, and subsequently, the head of large contractual issues, commissioned by enterprises of the Ministry of General Engineering of the USSR. The main directions of the work that he carried out were space modeling in ground-based test facilities and thermal vacuum testing of materials and components of products intended for work in space conditions. The results of these studies became the basis of his PhD thesis: "Growth rate, density and thermal conductivity of cryocondensate gases", which was defended in 1984, in the specialty "Thermal Physics and Molecular Physics".

In March 1987, Drobyshev A.S. established a "Laboratory of Cryophysics and Cryotechnologies". He was the head of this Laboratory until the last days of his life. In addition to the continuation of applied research, an important focus of the his Laboratory is the performance of fundamental researches related to the study of gas-solid phase transitions at low

temperatures and the properties of cryovacuum gas condensates.

In 1991, Drobyshev A.S. became a member of the initiative group headed by Academician Kozhamkulov T.A., which was engaged in the development of regulatory documents on the creation of research institutes at the university. As a result, in 1992, based on the Faculty of Physics at al-Farabi Kazakh National University (KazNU) the Research Institute of Experimental and Theoretical Physics (IETP), was established. A.S. Drobyshev became the deputy director of this institute, and later a director between 1993 and 1996.

In 1997 he defended his Doctoral thesis on the topic of "Growth kinetics, structure and properties of real cryocrystals", in the specialty "Solid State Physics".

Professor Drobyshev continued research works in the field of low-temperature physics, as a head of scientific projects in a number of fundamental research programs of the National Academy of Sciences of Kazakhstan. At the same time, Laboratory of Cryophysics and Cryotechnologies carried out researches and production activities, introducing low-temperature technologies at enterprises in Kazakhstan. He also was engaged in activity related with establishment of close scientific, industrial and pedagogical relationships with leading universities in the former Soviet space and far abroad. Among them Institute of Solid State Physics (Russia), Physical-Technical Institute of Low Temperatures (Ukraine), M.V. Lomonosov Moscow State University, Texas Christian University (USA), Autonomous University of Madrid (Spain), University of Manchester (England), Munich Polytechnic Institute (Germany).

Some of the professional activities of the professor Drobyshev A.S were related to the preparation of new scientific and pedagogical stuff in physical specialties. In 2000, he became a head of a creative team for the development of the State Standard in the specialty "Technique and Physics of Low Temperatures". In the same year, the first enrollment in this specialty is carried out at the Department of Physics at al-Farabi KazNU. He has prepared and read the basic special courses on these specializations: "Cryophysics", "Technique and Physics of Low Temperatures", "Experimental Physics", "Cryophysics of the Condensed State", "Physics of Cryocrystals", etc. He has supervised graduation and dissertations of bachelors and masters of the faculty. Under his leadership, have been defended PhD dissertations.

For several years, Drobyshev A.S. was a member of the academic council of the al-Farabi KazNU and the Faculty of Physics and Technology, a member of the dissertation council for defending doctoral dissertations, a member of the scientific and technical council of the IETP at Al-Farabi KazNU, an expert of the Ministry of Education and Science of the Republic of Kazakhstan. Since 2011, he was a member of the Council of the Institute of Oil and Gas of Kazakhstan. According to the materials of scientific research, more than 80 articles have been published in major international scientific journals, which reflect the main scientific results obtained by the group of professor Drobyshev.

Al-Farabi Kazakh National University,
Faculty of Physics and Technology

Institute of Experimental and
Theoretical Physics

National Nanotechnological Laboratory
of Open Type